Examination of transient carrier behaviors in organic field-effect devices via displacement current measurement

A DISSERTATION
SUBMITTED TO THE FACULTY OF THE GRADUATE SCHOOL
OF THE UNIVERSITY OF MINNESOTA
BY

Yan Liang

IN PARTIAL FULFILLMENT OF THE REQUIREMENTS
FOR THE DEGREE OF
DOCTOR OF PHILOSOPHY

C. Daniel Frisbie, Advisor

January 2011

Acknowledgements

I would first like to thank my advisor Dan Frisbie. Among the many things I have learned from him, two things are the most valuable to me and help me to become a better scientist and a better person. The first is to focus and work hard on what really matters, the second is to think beyond the surface and ask myself what I have really learned. I am also very grateful for the freedom and trust he gives me during the years of this Ph.D. project. I would like to thank the former and present Frisbie group members for their help and knowledge. I would especially like to thank Derek Stevens, Moon Sung Kang, and Salil Bapat, who have spent a lot of time maintaining the proper operation of our lab equipments.

I would like to thank my collaborators Hsiu-Chuang Chang and Prof. Paul Ruden, who have developed all the analytical and numerical models in this thesis, and kindly provided me with their beautiful calculation results. Without their help, I would never finish this thesis. I would especially like to thank Hsiu-Chuang, who always showed great patience during my frequent visits to his office with all kinds of crazy questions. I would also like to thank Jian Qin, who helped me develop the very first mathematical model to explain the displacement current I measured.

I would like to thank my friends, Siguang Sui, Jian Qin, Wei Wang, Xiaobo Gong, Dongbo Zhang, Lejun Qi, Nan Zhang, who make the life here more enjoyable.

Finally I would like to thank my family for the support they give me. I am so grateful to my parents, who always encourage me and believe in me. I am forever indebted to my wife, who sacrifices so much that I can finish this thesis.

Abstract

Organic field-effect transistors (OFETs) are one of the key components of the ubiquitous flexible electronics in the near future. Since the first report in the mid-1980s, OFETs have been intensively studied for more than 20 years. However, most of these studies are based on steady state or quasi steady state DC measurements, which are not sensitive to transient processes including the formation and depletion of the conducting channel. These transient processes are essential parts of the device operation, and determine the response frequency of OFETs. For these reasons, the transient carrier behaviors during these processes warrant examination.

This thesis develops displacement current measurement (DCM) as a technique to probe transient carrier behaviors. Instead of using OFETs for measuring displacement current, long-channel capacitors (LCCs) are used. A LCC can be viewed as a simplified OFET with only one channel contact to limit the carrier injection/extraction to one direction only. The channel of a LCC is elongated to millimeter range to increase the transient time and the displacement current associated with charging/discharging the channel. Displacement current has been measured from LCCs under cyclic gate voltage sweeps. The number of the injected, extracted, and trapped carriers can be calculated by integrating the displacement current with respect to time. A current peak has always been observed in the charging sweep, and it is attributed to the transient process of conducting channel formation. Analytical and numerical device models have been developed to understand the transient carrier behaviors. It is found that carrier mobility can be calculated from the slope of the displacement current peak. In addition, the evolution of the carrier distribution in the long channel during the conducting channel formation and depletion are presented in detail. Further more, the effects of carrier traps on the transient carrier behaviors are discussed.

DCM has also been used to study the contact effects at metal-pentacene interfaces. It is found that the carrier trapping in the long channel of the LCCs with Au contacts is indirectly caused by the deep trap states at the pentacene-dielectric interface in

the contact region generated by Au penetration. Low trapped carrier density is found in the LCCs with Cu contacts due to the shallow penetration of Cu atoms. In addition, ambipolar injection and transport are observed in a LCC with Al contact and a PMMA buffer layer between pentacene and SiO_2. Thus DCM can be used to characterize the quality of metal-organic contacts.

The conducting channel depletion dynamics under constant gate voltages has also been examined. It is found that the discharging displacement current can either follow an exponential decay or a power law decay, depending on the discharging gate voltage. A simple RC model has been given to explain these different decay behaviors. For the power law decay, the decay exponent measured from the experimental data is around 1.2 to 1.3, while the exponent predicted by the RC model is 2. The smaller exponent observed in experiment might be attributed to the effect of carrier traps.

Table of Contents

List of Tables

List of Figures

1 Introduction

1.1 Thesis overview

Displacement current measurement (DCM) is an unconventional and relatively new technique in the field of organic electronics. DCM was first introduced in 1992 by Egusa *et al.* to study the charge carrier injection in organic light-emitting diodes (OLEDs).[1, 2] Since then, a small number of research groups in the world have further developed this technique and applied it to study the carrier behaviors in organic field-effect transistors (OFETs),[3-12] OLEDs,[13-15] and organic solar cells.[16]

Using DCM to study OFETs was first reported by the Niwano group in 2003.[3, 5] In recent years, a few research groups also adopted this technique in their OFETs study.[6, 8-12] However, the basic carrier behaviors in an OFET during the displacement current measurement were still not well understood at the beginning of this thesis. Rich information hidden in the I-V characteristics of DCM can be extracted.

The main purpose of this thesis is to further develop DCM as a *transient* measurement technique, and to use it to examine the transient carrier behaviors occurring during conducting channel formation and depletion in OFETs.

The thesis is organized as the following manner:

Chapter 2 gives an overview of OFETs and the DC and transient measurements for characterizing OFETs. The importance of the transient measurements is emphasized and the recent development of the transient measurement techniques is reviewed.

Chapter 3 describes the experimental procedures for fabricating pentacene long-channel capacitors (LCCs) and the electrical setup for measuring displacement current.

The subsequent chapters are presented in research article form:

Chapter 4 summarizes two previous published papers: Yan Liang, C. Daniel Frisbie, Hsiu-Chuang Chang, and P. Paul Ruden, "Conducting channel formation and annihilation in organic field-effect structures." *J. Appl. Phys.* **2009**, 105, 024514; Hsiu-Chuang Chang, P. Paul Ruden, Yan Liang, and C. Daniel Frisbie, "Transient effects

controlling the charge carrier population of organic field effect transistor channels." *J. Appl. Phys.* **2010**, 107, 104502. This chapter focuses on the basic I-V characteristics of LCCs under displacement current measurement. A geometry model and a full numerical model are described, providing a detailed physical picture of the transient carrier behaviors during the conducting channel formation. The effects of carrier traps on the displacement current are discussed briefly with the aid of the numerical model.

Chapter 5 has been prepared for submission as Yan Liang, Hsiu-Chuang Chang, Salil Bapat, P. Paul Ruden, and C. Daniel Frisbie, "Examination of contact effects in organic field-effect devices via displacement current measurement." This chapter expands the application of DCM to examine contact effects at metal-organic interfaces in pentacene LCCs with Au, Cu, and Al contacts. It is found that the deep traps generated by metal penetration in the contact region can cause carrier trapping in the channel. In addition, ambipolar injection and transport are observed in a LCC with an Al contact and a PMMA buffer layer between pentacene and SiO_2.

Chapter 6 has been prepared for submission as Yan Liang, Hsiu-Chuang Chang, P. Paul Ruden, and C. Daniel Frisbie, "Examination of conducting channel depletion dynamics of organic field-effect devices via displacement current measurement." Two different extraction situations are considered: the transient carrier extraction under linear gate voltage sweeps, and that under constant gate voltages. For the transient carrier extraction under linear voltage sweeps, the evolution of the carrier distribution in the channel is given. For the transient carrier extraction at constant gate voltages, it is found that the discharging displacement current can either follow an exponential decay or a power law decay, depending on the discharging gate voltage. A simple RC model is proposed to explain these decay behaviors.

Chapter 7 presents the preliminary results and proposed future experiments for extending the work presented in this thesis. Specifically, systematic comparison of the activation energies associated with the transient and steady state transport is proposed. A new gate voltage profile is proposed, enabling the variable temperature study of the transient carrier extraction at constant gate voltages with the aid of numerical simulations. A device for quickly characterizing the electrical properties of spin-coated

polymer films, and a device for accurately determining the carrier density induced by ionic liquid are also proposed.

Appendix I describes the feature dimensions of the shadow masks for fabricating LCCs used in this thesis. Appendix II includes the Keithley 2612 test scripts for displacement current measurement. Appendix III describes the common mistakes one should avoid when measuring displacement current. Appendix IV describes a proposed experiment to study detrapping kinetics.

My contribution is experimental work. Device models are presented in the thesis to explain the experimental results. These models represent the work of my collaborators Hsiu-Chuang Chang and Prof. P. Paul Ruden.

2 DC and transient measurements of organic field-effect transistors

2.1 Introduction to organic field-effect transistors

The key difference between organic field-effect transistors (OFETs) and their inorganic counterparts is the use of organic semiconducting materials in OFETs.[17-20] The organic semiconductors can be divided into two classes: small organic molecules[21, 22] and conjugated polymers.[23, 24] Among all the small molecules, pentacene is probably the most widely used p-type semiconducting material in OFETs.[25-28] The structure and electrical connections of a pentacene OFET is shown in Figure 2-1. It consists of source and drain electrodes (Au), an organic semiconductor layer (pentacene), a gate dielectric layer (SiO_2), and a gate electrode (p+ Si). An OFET acts as a switch, with its "ON" and "OFF" states controlled by the gate voltage (V_G). Suppose that a constant drain-to-source voltage (V_D) is applied on the pentacene OFET in Figure 2-1, and that the pentacene film is undoped. When V_G is zero, the carrier density in the channel is very low, and only a very small current (I_D) runs through the channel. The transistor is in the "OFF" state. When V_G is negative, positive carriers (holes) are accumulated in the channel, and a current several orders of magnitude higher than the OFF-state current runs through the channel. The transistor is in the "ON" state.

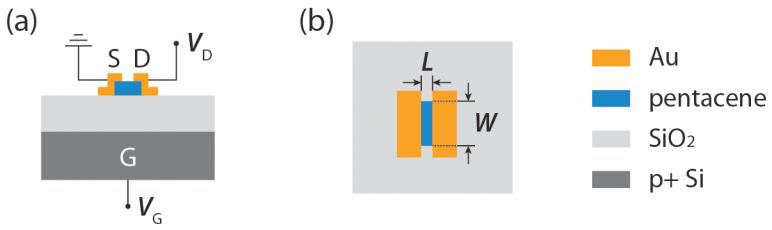

Figure 2-1 (a) Schematic cross section and electrical connections of a pentacene OFET. S, D, and G stand for source, drain, and gate electrodes, respectively. (b) Schematic top view of the same device. L and W are the channel length and width, respectively.

One of the earliest OFETs was reported by Tsumura *et al.* in the 1986 with a carrier mobility ~10^{-5} $cm^2V^{-1}s^{-1}$ (ref. 29). After more than 20 years of intense research and device optimization, OFETs with a carrier mobility in the range of 0.1–1 $cm^2V^{-1}s^{-1}$ are routinely fabricated.[17-20] This mobility range is comparable to that of the inorganic transistors based on amorphous silicon. With good electrical performance and other unique properties, such as low cost, light weight, solution processability, and compatibility with flexible plastic substrates, OFETs are not only the potential candidate to substitute amorphous silicon transistors, but also the key components to the future flexible electronics.[30] Some of the current flexible circuits based on OFETs are shown in Figure 2-2.

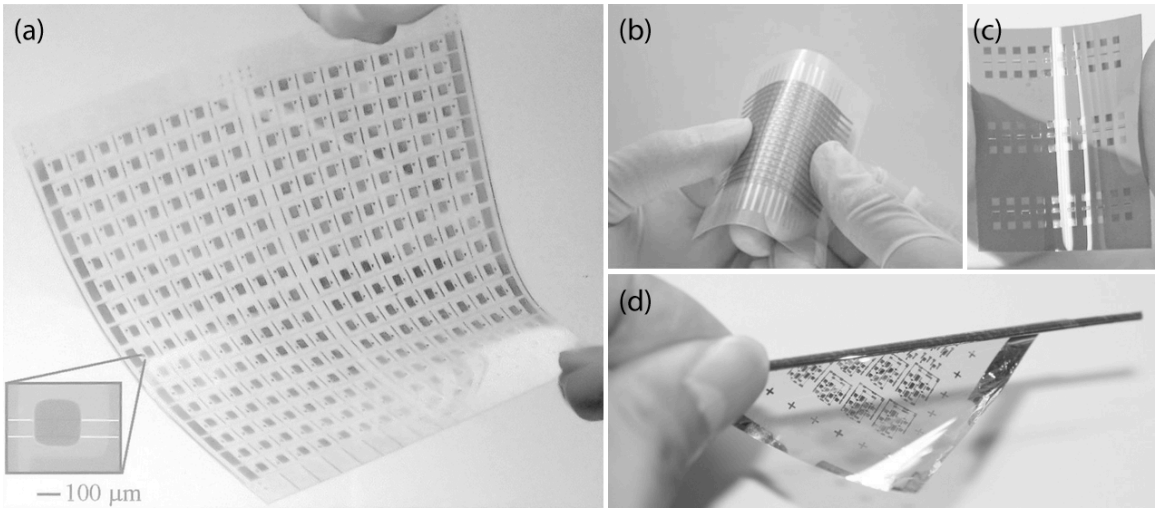

Figure 2-2 Flexible electronic devices and circuits based on OFETs. (a) Flexible active matrix backplane circuits for E-ink display developed by Rogers *et al.* in 2000 (image from ref. 31). (b) Electronic artificial skin developed by Someya *et al.* in 2004 (image from ref. 32). (c) Flexible OFETs based on ion-gel gate dielectric with an operating voltage less than 3 V developed in our group in 2008 (image from ref. 33). These devices were fabricated with aerosol jet printing. (d) Ultraflexible organic circuits developed by Someya *et al.* in 2010 (image from ref. 34).

2.2 DC measurements of OFETs

During the DC measurements on OFETs, the source-to-drain current (I_D) is either measured by sweeping the drain voltage at a series of constant gate voltages to get the output characteristics (Figure 2-3a), or by sweeping the gate voltage at a constant drain voltage to get the transfer characteristics (Figure 2-3b).

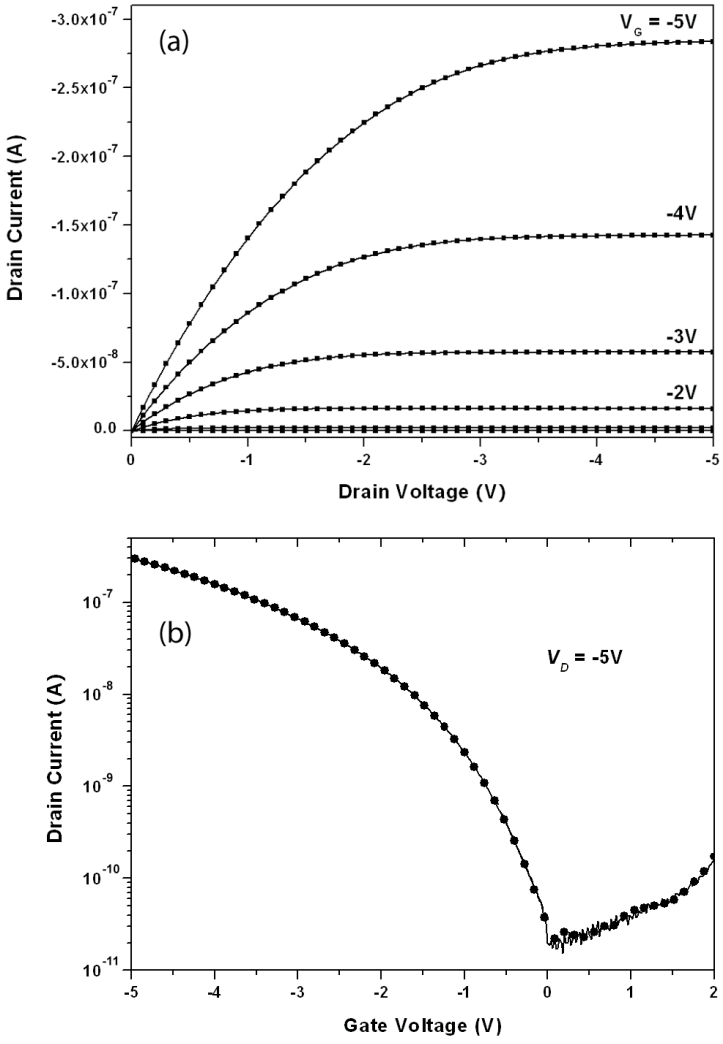

Figure 2-3 (a) Output characteristics of a pentacene OFET. (b) Transfer characteristics of the same device.

When $-(V_G - V_T) >> -V_D$, the transistor is working in the linear regime. I_D is expressed as

$$I_D = \frac{W}{L} C' \mu \left[(V_G - V_T) - \frac{V_D}{2} \right] V_D \qquad (2\text{-}1)$$

where V_T is the threshold voltage, C' is the capacitance per unit area of the gate dielectric, and μ is the carrier mobility.

When $-(V_G - V_T) < -V_D$, the transistor is working in the saturation regime. I_D satisfies

$$I_D = \frac{W}{2L} C' \mu (V_G - V_T)^2 \qquad (2\text{-}2)$$

The carrier mobility is usually calculated from the transfer characteristics by using either Equation 2-1 or Equation 2-2. Moreover, other device parameters such as ON/OFF ratio, threshold voltage, and subthreshold swing can also be determined from the transfer characteristics.

2.3 Transient measurements of OFETs

The DC measurements of OFETs are steady state or quasi-steady state measurements. They are not sensitive to the transient processes occurring during the conducting channel formation and depletion. These transient processes, however, are essential parts of the device operation, and they determine the response frequency of the devices. In addition, the transient carrier behaviors may be different from those in the steady state, because the trapping and detrapping may not be in equilibrium during the transient processes.

Transient measurements focus on the transient processes mentioned above. Only a few techniques have been used to study the transient processes in OFETs. One of the

techniques is called time-resolved microscopic optical second-harmonic generation (TRM-SHG).[35-38] It is an optical technique employed by the Iwamoto group to study transient carrier transport before the conducting channel is formed. During the measurement, the drain and gate electrodes are grounded, and a positive voltage pulse at the source electrode generates a sheet of carriers moving from the source to the drain (Figure 2-4). The second harmonic generation (SHG) signal detected by this technique is sensitive to lateral electric field. Because a large lateral electric field exists at the front of the carrier sheet in the channel, TRM-SHG can directly visualize the movement of the front of the carrier sheet (Figures 2-5a and 2-5b).

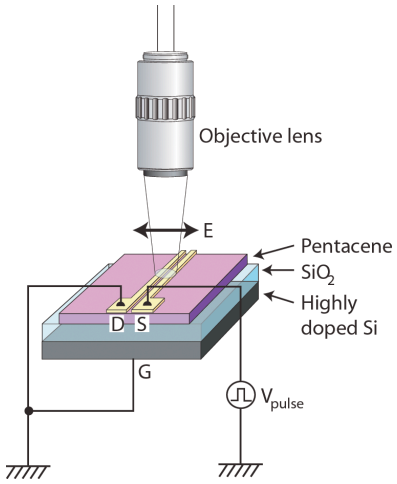

Figure 2-4 Experimental setup for time-resolved microscopic optical second-harmonic generation (TRM-SHG) used by the Iwamoto group. A voltage pulse at the source electrode generates a sheet of carriers moving from the source to the drain. Image from ref. 35.

In their earliest TRM-SHG study,[35] only drift was considered and carrier sheet front was thought to move at constant speed v. The transient carrier mobility was then calculated from $\mu = vL/V_D$, where L is the channel length, and V_D is the drain-to-source voltage. Later, the simple linear relationship between the position of the carrier sheet front and time was replaced by a power law relationship when diffusion was also considered.[36] TRM-SHG was also used to study transient carrier injection.[37] It was found

that inefficient carrier injection led to a high lateral electric field at the contact edge. The effect of traps on the transient carrier transport was also discussed in a recent publication.[38]

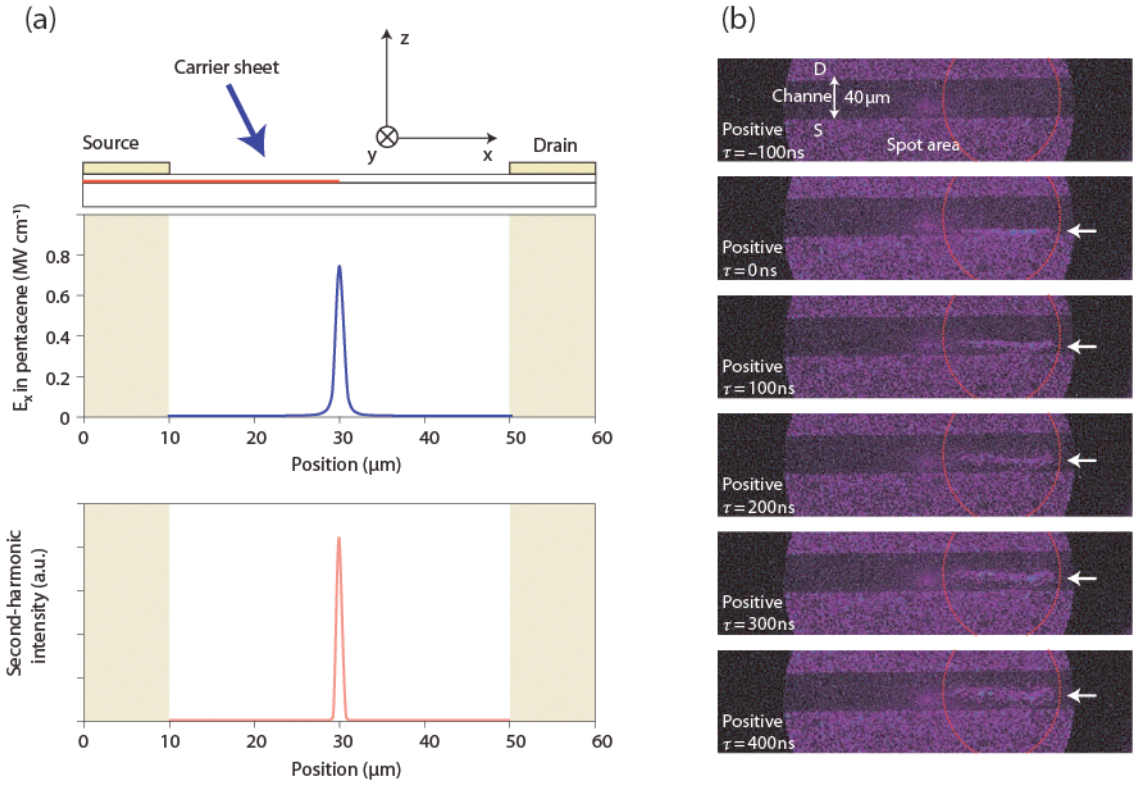

Figure 2-5 (a) The second-harmonic intensity measured by TRM-SHG is sensitive to the lateral electric field in the channel (E_x) whose maximum is at the front of the carrier sheet. (b) Visualization of the carrier sheet front moving in the channel by TRM-SHG. Images from ref. 35.

A modified time-of-flight (MTOF) method was first introduced by the Dodabalapur group to study the transient carrier transport.[39] It has also been adopted and further developed by others.[40, 41] The experimental setup of MTOF is shown in Figure 2-6. Similar as in TRM-SHG, a voltage pulse at the source electrode generates transient carrier movement in the channel. When the carriers injected from the source electrode reach the drain electrode, a transient current is generated and recorded at the drain electrode. The transient time during which the *fastest* carriers travel from the source to

the drain can then be determined and the transient mobility of these fastest carriers is calculated. It is found that the transient mobility is typically larger than the field-effect mobility obtained from the DC measurements.[39, 42] In addition, the activation energy associated with transient transport is higher than the activation energy associated with the steady state transport.[43] The differences in mobility and activation energy were attributed to the different carrier concentrations during the transient and steady state transport.[43]

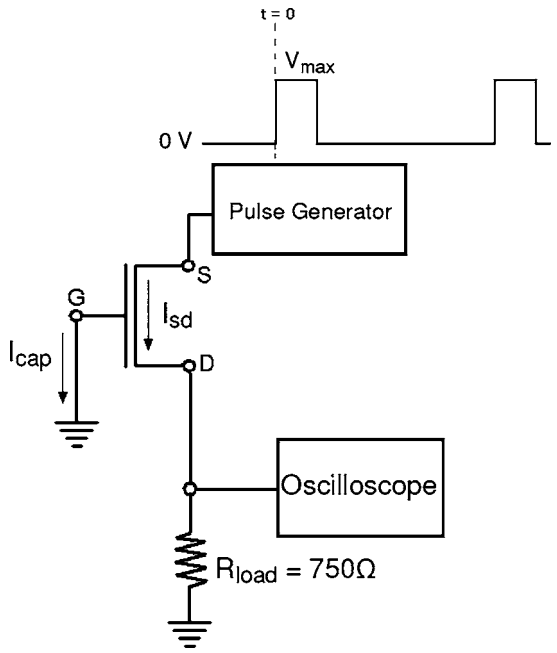

Figure 2-6 Experimental setup for the modified time-of-flight (MTOF) measurement used by the Dodabalapur group. A voltage pulse at the source electrode generates a sheet of carriers moving from the source to the drain. When the carriers reach the drain electrode, a signal is detected in the oscilloscope. Image from ref. 39.

Another technique that can potentially probe the transient carrier behaviors in OFETs is displacement current measurement (DCM). DCM, however, has not yet been fully developed as a transient technique. DCM first was used by Egusa *et al.* to study the carrier injection in organic light-emitting diodes (OLEDs).[1, 2] It was later introduced as a technique to characterize carrier injection in OFETs by the Niwano group.[3, 5] During the

measurement on OFETs, the source and drain electrodes are both grounded and cyclic voltage sweeps are applied on the gate electrode, as shown in Figure 2-7. The displacement current associated with charging and discharging the device is measured at the gate electrode. A current peak occurring during carrier injection was always observed in Niwano's papers.[3-5, 7] However, the origin and physical meaning of this peak were not well explained. As we will see in Chapter 4, this peak is associated with transient carrier injection and transport. The Majima group further developed the DCM technique.[6, 9] However, they typically made the area of transistor channel much smaller than the overlapping area between the channel contacts and organic semiconductor layer. By doing this, they focused only on carrier injection and extraction but *ignored* the transient carrier transport in the channel.

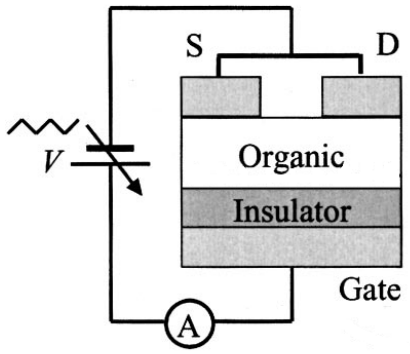

Figure 2-7 Experimental setup for displacement current measurement (DCM) used by the Niwano group. Image adopted from ref. 4.

One major purpose of this thesis is to further develop the DCM technique, and use it to understand the transient carrier behaviors in OFETs. Comparing to TRM-SHG and MTOF, DCM has several advantages. Firstly, the experimental setup of DCM is very simple, and electrical signal is easy to detect when the device structure is optimized (more details in Chapter 4). Secondly, not only can transient carrier injection and transport can be detected, but the transient carrier extraction can also be examined with DCM. The transient extraction process is part of the OFET device operation, which

occurs when the transistor is turned off. Thirdly, by integrating the displacement current with respect to time, the number of injected, extracted, and trapped carriers can be calculated, providing additional information about transient carrier behaviors. In the following chapters, we will provide detailed analysis on DCM and its applications.

3 Device fabrication and electrical characterization

3.1 Device fabrication

The devices we used for displacement current measurement are called long-channel capacitors (LCCs). The schematic structure of a LCC is shown in Figure 3-1. A LCC can be seen as an OFET with one channel contact removed and the conducting channel elongated to millimeter range. The channel width and channel length of the LCC are defined in Figure 3-1b. OFETs were typically made together with LCCs, and were only used for DC measurements. The schematic structure of an OFET is shown in Figure 3-1 as well.

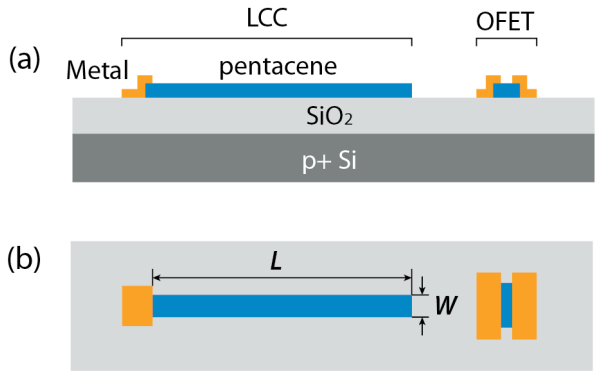

Figure 3-1 Schematics of a pentacene LCC and a pentacene OFET fabricated on a p+ Si wafer with 300 nm SiO_2. (a) Cross section view. (b) Top view.

As shown in Figure 3-1, a heavily doped p-type Si wafer with 300 nm SiO_2 (Silicon Valley Microelectronics) was used as the substrate. The backside of the wafer was scratched to expose the silicon and then painted with silver paint (Ted Pella, Inc.) to make the heavily doped Si serve as the gate electrode.

Twice sublimed pentacene was deposited on the SiO_2 by thermal evaporation. The shape of the pentacene film was defined by the pentacene shadow mask (PM). During the deposition, the substrate temperature was 30 °C and the deposition rate was 0.1–0.2 $Å s^{-1}$.

The metal contact was then deposited by thermal evaporation through the contact shadow mask (CM). The substrate was water-cooled during the deposition. The thickness of the metal contact was 40 nm. Three metals were used, including Au, Cu, and Al. Au and Cu were evaporated from alumina coated evaporation boats (R.D. Mathis Company), and the deposition rate was 0.5–1 $Å s^{-1}$. Al was evaporated from a tungsten basket (R.D. Mathis Company), and the deposition rate was 2–3 $Å s^{-1}$.

The shadow masks were designed to allow as many as 34 LCCs and 30 OFETs to be fabricated together on the same chip in a single run. Figure 3-2 shows the schematics of some shadow masks and finished device chips. The size of all the masks is 25 mm × 25 mm. PM1, PM2, CM1, and CM2 were fabricated from 3 inch 125 μm thick silicon wafers (Virginia Semiconductor). The fabrication procedures including photolithography and deep trench etching were done in the Nanofabrication Center at the University of Minnesota. PM3 and CM3 were fabricated from 0.006 inch thick stainless steel sheet by laser cutting. They are directly ordered from Photo Etch Technology. PM2 was used to make LCCs with different channel length. CM2 was used to make OFETs with different channel length. PM3 and CM3 were used together to make LCCs with large W/L ratio to increase the displacement current. The width of the overlapping area between metal and pentacene in LCCs are typical 0.1–0.2 mm. The detailed feature dimensions of the shadow masks are presented in Appendix I.

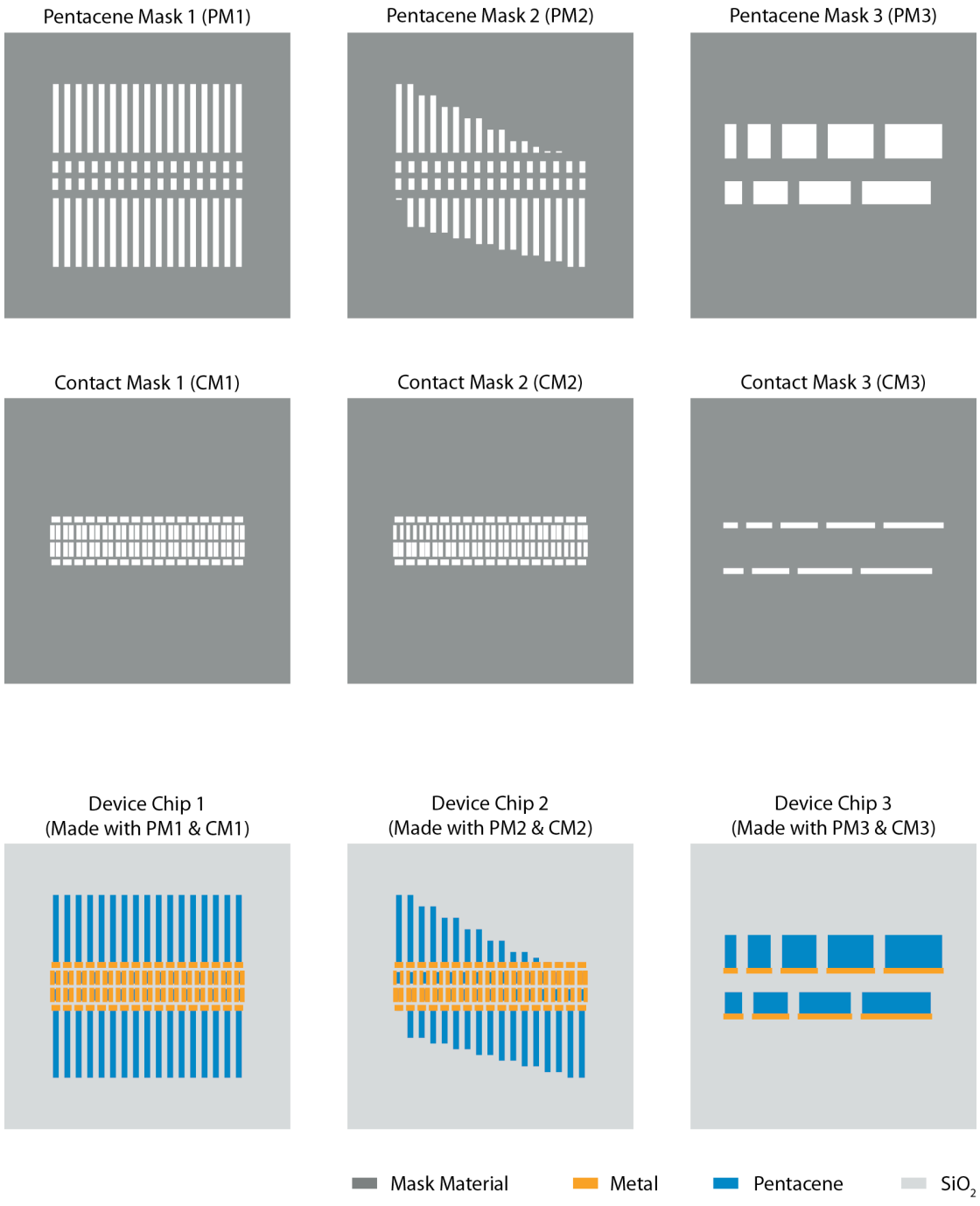

Figure 3-2 Schematics of pentacene and contact shadow masks and device chips fabricated with these shadow masks. The size of each shadow mask is 25 mm × 25 mm. PM1, PM2, CM1, and CM2 are made of 125 µm thick silicon wafer. PM3 and CM3 are made of 0.006 inch thick stainless steel.

3.2 Electrical characterization

All electrical measurements were performed in the dark in a vacuum probe station with temperature control (Lake Shore). For measuring displacement current from LCCs, a Keithley 2612 dual-channel SourceMeter was used. Custom test scripts were used to control the machine (Appendix II). During a typical measurement, the Channel B of the Keithley 2612 applied a voltage profile on the gate electrode, and the Channel A measured the displacement current running through the grounded channel contact, as shown in Figure 3-3a.

Two types of gate voltage profiles were used, as shown in Figure 3-3. The first voltage profile (Figure 3-3b) included two or three cyclic sweeps, each cyclic sweep consisted of a forward sweep (V_1 to V_2), and a reverse sweep (V_2 to V_1). A constant voltage was typically applied for 5 s before the first cyclic sweep to eliminate the large displacement current generated by the sudden voltage change. The sweep was comprised of small voltage steps, as shown in the inset of Figure 3-3b. The typical height of the step was 0.1 V, and duration of the step was determined by the integration time to measure the current. For Keithley 2612, the integration time is controlled by the NPLC (Number of Power Line Cycles) parameter. We typically chose NPLC = 1, and the resulting sweep rate was 5.7 Vs^{-1}.

The second voltage profile included two voltage steps (Figure 3-3c). During the first voltage step (V_3), the conducting channel was filled with charge carriers. The charging time t_1 was 15 to 30 s to ensure that the carrier distribution in the channel was stabilized and uniform. No displacement current was measured in this step. During the second step (V_4), carriers were extracted from the pentacene channel, and the displacement current associated with the carrier extraction was measured as a function of time. When the discharging time (t_2) is long enough, the channel could be either completely or partially discharged based on the discharging voltage (V_4).

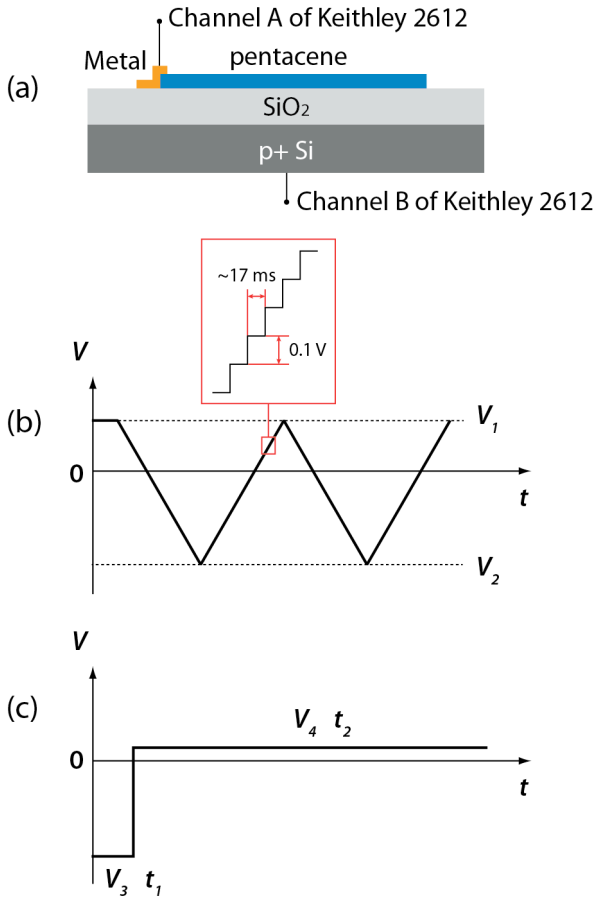

Figure 3-3 (a) Experimental setup for measuring displacement current from a pentacene LCC. (b) Gate voltage profile containing two consecutive cyclic voltage sweeps. (c) Gate voltage profile containing charging and discharging steps.

For DC measurements of OFET, a Keithley 6517A was used to source the gate voltage, a Keithley 237 was used to source the drain voltage and measure the drain current, and a Keithley 236 was used to measure the source current, as shown in Figure 3-4. Custom Labview codes were used to control the above Keithley instruments simultaneously.

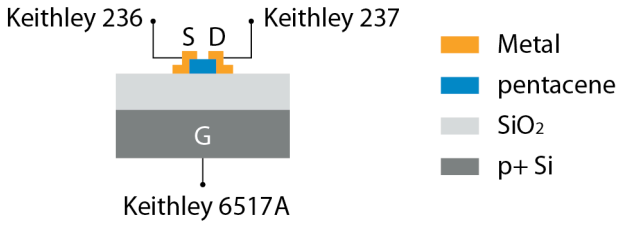

Figure 3-4 Experimental setup for characterizing a pentacene OFET.

4 Basics of displacement current measurement and conducting channel formation in organic field-effect devices

4.1 Introduction

Organic field-effect transistors (OFETs) have been intensively studied for more than 20 years because of their low cost, light weight, solution processability, and compatibility with flexible plastic substrates.[17-20, 24] Recently, displacement current measurement (DCM) has been used by the Niwano group to study the charge carrier injection in OFETs.[3, 5] The Majima group[6, 9] and others[8, 10, 11] have also adopted DCM in their OFET research. A current peak was typically observed during the charging sweep of displacement current measurement.[3-5, 7] However, the physical meaning of this current peak was not well understood.

In this chapter, we show that the current peak is associated with the transient process of conducting channel formation. Instead of using OFETs for displacement current measurement, we use long-channel capacitors (LCCs). A LCC can be seen as a simplified OFET with only one channel contact to limit the carrier injection/extraction to one direction only. The channel of a LCC is elongated to millimeter range to increase the transient time and the displacement current associated with charging/discharging the channel. Displacement current has been measured from LCCs under cyclic gate voltage sweeps. Analytical and numerical device models are given to analyze the experimental results. With these models, we are able to calculate the carrier mobility from the slope of the displacement current peak and plot the evolution of the carrier distribution in the long channel during the conducting channel formation. The transient carrier behavior during the conducting channel depletion will be discussed in Chapter 5.

4.2 Long-channel capacitors

Figure 4-1 shows the common electrical connections on a pentacene OFET for displacement current measurement. The source and drain electrodes are shorted and grounded, and a cyclic voltage sweep is applied on the gate electrode. Instead of measuring the displacement current at the gate electrode as first introduced by the Niwano group,[3, 5] we measure the displacement current at the grounded source and drain electrodes. We think this is a more direct way of measuring the displacement current associated with charging and discharging the *conducting channel*. In addition, measuring displacement current from the source and drain contacts excludes the background current associated with the internal capacitance of the Keithley instrument when sourcing voltage sweeps (see Appendix III for more details). The advantage of using an OFET for displacement current measurement is that the DC characteristics can be measured from the same device as well.[3-7, 9] However, there are a few drawbacks.

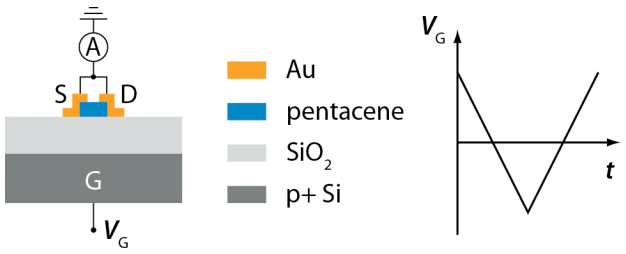

Figure 4-1 Schematic electrical connections on a pentacene OFET for displacement current measurement.

First, because the source and drain electrode are shorted together, carriers are injected into the channel from the source and the drain in opposite directions. The same is also true for the extraction process. For the sake of simplicity, the injection and extraction processes should be limited to one direction only. Also, one-direction-only injection avoids the "collision" of the two carrier sheets moving in the opposite direction during the injection process.

Second, the channel length of the OFETs is typically in the range of several tens to several hundreds of microns. This means the transient time is very short. Additional instrumentation may be required to measure current at higher time resolution. In addition, because the area of the conducting channel is usually much smaller than the total area of the source and drain electrodes, the displacement current of interest, which is the current associated with charging and discharging the channel, is much smaller than the background displacement current associated with the source and drain electrodes.[6, 9] To increase the accuracy of the measurement, it is necessary to increase the displacement current of interest and decrease the background current.

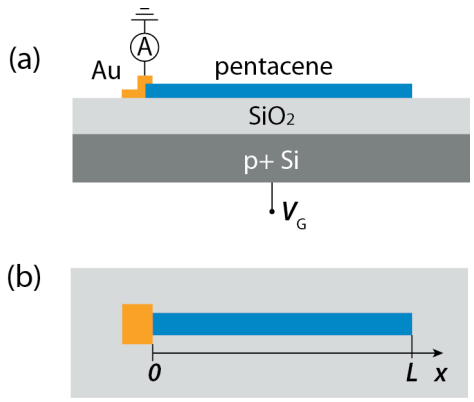

Figure 4-2 (a) Schematic cross section of a pentacene long channel capacitor (LCC) and its electrical connections for displacement current measurement. (b) Schematic top view of the device. The one-dimensional coordinate system is also shown.

Based on the above discussion, one of the channel contacts is removed to limit the injection and extraction to one direction only. In addition, the channel length is elongated to millimeter range to increase both the transient time and the displacement current associated with charging and discharging the channel. The new device structure and its electrical connections are shown in Figure 4-2. Only one Keithley 2612 unit is needed for measuring the displacement current. We call this new device a long-channel capacitor (LCC). In some cases, the channel width is increased to several millimeters to further increase the displacement current.

A LCC can be seen as a simplified OFET. The factors that affect the transient processes in an OFET, such as carrier mobility and carrier traps at the semiconductor-dielectric interface, are still present in a LCC. However, the transient processes in a LCC occur over a much longer time scale because of the long channel, making them easier to detect. Studying the transient carrier behaviors in the long channel is an interesting topic by itself. We also believe that the information we learn about the transient processes in LCCs can be applied to OFETs.

4.3 Experiment

A heavily doped p-type Si wafer with a 300 nm thick thermal oxide layer was used as the substrate. The heavily doped Si also served as the gate electrode. On the top of the SiO_2, a 30 nm pentacene film was thermally evaporated through a shadow mask to define the rectangular-shaped strip. The deposition rate was 0.1 Å/s and the substrate temperature was 30 °C during the deposition. The width of the pentacene strip (W) was 0.5 mm and the length varied from 1 mm to 6 mm. After pentacene deposition, a 40 nm gold layer was evaporated through another shadow mask to define the channel contact with a size of 0.5 mm by 0.75 mm. The width of the overlapping area between the gold contact and the pentacene film was 0.1–0.2 mm. The pentacene channel length (L) is defined as the distance from the edge of the gold electrode on pentacene to the other end of the pentacene strip, as shown in Figure 4-2b.

Electrical characterization was carried out by measuring the displacement current running through the grounded channel contact while linearly sweeping the gate voltage. A Keithley 2612 dual-channel SourceMeter was used, with one channel sourcing the gate voltage, and the other channel measuring the displacement current. Consecutive cyclic sweeps were usually used. In each cyclic sweep, the forward sweep was from +40 to –40 V, and the reverse sweep was from –40 to +40 V. The sweep rate was 5.7 V/s. All measurements were performed in the dark in a vacuum probe station.

4.4 Basic I-V characteristics of LCCs

In this chapter, we only discuss the measurement scheme with gate voltage sweeps (Figure 3-3b). In Chapter 6, we will discuss another measurement scheme with gate voltage steps (Figure 3-3c), which is for examining transient carrier extraction.

Figure 4-3 shows the typical I-V characteristics of a pentacene LCC during one cyclic gate voltage sweep. The channel length and width are 5.88 mm and 0.5 mm, respectively. At the beginning of the forward sweep, a region of constant displacement current is observed (Region I). This current is due to the metal contact and is determined by the following equation:

$$I = \frac{dQ}{dt} = \frac{d(C_0 V_B)}{dt} = C_0 \frac{dV_B}{dt} = C_0 r_V \qquad (4\text{-}1)$$

where Q is the amount of charge accumulated under the gold contact, C_0 is the effective capacitance associated with the gold contact, and $r_V = dV_G / dt$ is the sweep rate. Since the overlapping area between the gold and pentacene is small, and the thickness of pentacene is much smaller than that of SiO_2, C_0 approximately equals $\varepsilon_0 \varepsilon'_{SiO_2} A_{Au} / d_{SiO_2}$, where ε_0 is the vacuum permittivity, ε'_{SiO_2} is the relative permittivity of SiO_2, A_{Au} is the area of the gold electrode, and d_{SiO_2} is the thickness of SiO_2. The displacement current associated with the gold contact can be measured after carefully detaching the pentacene from the contact (at $x = 0$ in Figure 4-2) with a sharp probe under a microscope, as shown by the dashed line in Figure 4-3.

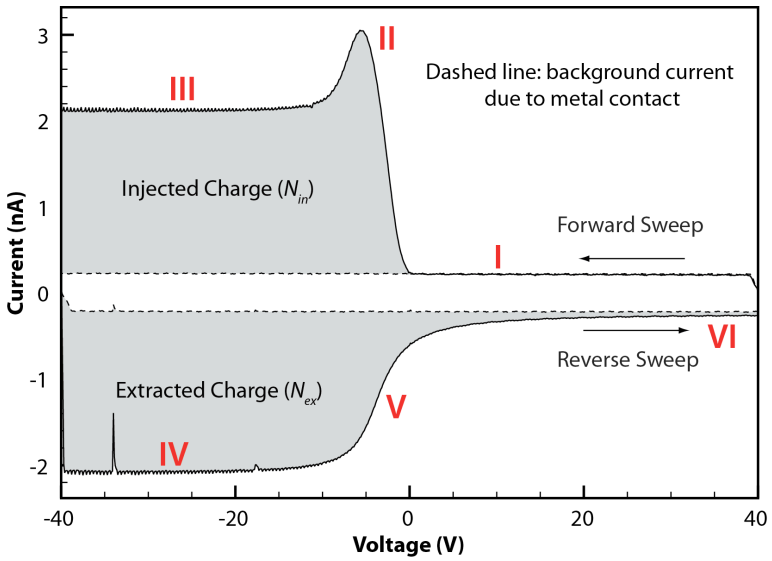

Figure 4-3 Basic I-V characteristics of a pentacene LCC. Six different regions (I to VI) can be seen in the displacement current curve. Dashed line: background displacement current associated with the metal contact. The number of carriers injected in the forward sweep and the number of carriers extracted in the reverse sweep can be calculated by integrating the displacement current with respect to time.

Following the constant-current region, a peak is observed on the displacement current curve (Region II), which is due to the transient carrier transport in the channel (see Section 4.4.1 for more details). Eventually, carriers are distributed uniformly in the channel and the pentacene film becomes conductive. The displacement current then enters the second constant region (Region III). The constant current is determined by

$$I = C_1 r_V \qquad (4\text{-}2)$$

where C_1 is the new effective capacitance determined by the area of gold and pentacene (A_{pen}) combined, *i.e.* $C_1 = \varepsilon_0 \varepsilon'_{SiO_2} (A_{Au} + A_{pen}) / d_{SiO_2}$.

At the beginning of the reverse sweep, the sign of the displacement current changes but the absolute value of the current remains the same (Region IV). At about −15 V, a transient region appears (Region V) and the current gradually decreases in magnitude from the high constant value to the low constant value. In this region, the

carrier distribution in the channel is no longer uniform (see Section 5.3.1 for more details). Near the end of the reverse sweep (Region VI), the displacement current is slightly larger in magnitude than the displacement current associated with the gold contact (dashed line). This is due to the slow emission of trapped holes (see Section 4.4.2.3).

Figure 4-4 shows the displacement current measured from devices with different channel lengths. It is apparent that the displacement current from -40 to -20 V scales nicely with the channel length, as suggested by Equation 4-2. In addition, the widths of the transient regions in both the forward and reverse sweeps increase with the channel length. This is because it takes longer for the carriers to get in and out of the channel as the channel gets longer.

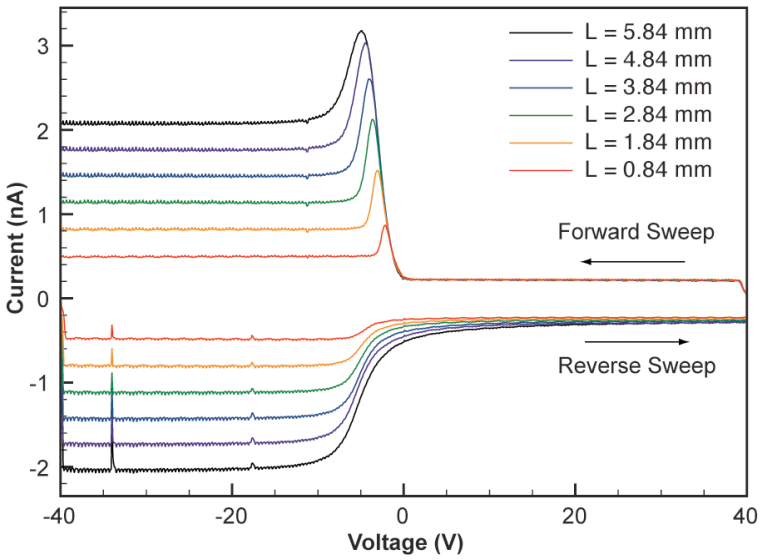

Figure 4-4 Displacement current measured from pentacene LCCs with different channel lengths.

4.5 Determination of trapped carrier density

The displacement current can be used to calculate the number of carriers injected into the channel during the forward sweep, and the number of carriers extracted from the channel during the reverse sweep, as shown in Figure 4-3. The difference between the

two is the number of carriers trapped in the channel after one cyclic sweep. The number of carriers injected into the pentacene channel during the forward sweep is

$$N_{in} = \left| \frac{1}{er_V} \int_{V_1}^{V_2} (I^f - I^{Au,f}) dV \right| \qquad (4\text{-}3)$$

where e is the elementary charge, V_1 and V_2 are the starting and ending voltage for the forward sweep, I^f is the displacement current during the forward sweep, and $I^{Au,f}$ is the displacement current due to the gold contact during the forward sweep, indicated by the dashed line in Figure 4-3.

The number of carriers extracted from pentacene channel during the reverse sweep is

$$N_{ex} = \left| \frac{1}{er_V} \int_{V_2}^{V_1} (I^r - I^{Au,r}) dV \right| \qquad (4\text{-}4)$$

where I^r is the displacement current during the reverse sweep, and $I^{Au,r} = -I^{Au,f}$ is the displacement current due to the gold contact during the reverse sweep. Therefore, the average trapped carrier density at the end of one cyclic sweep is

$$\overline{p}_{trap} = N_{trap} / A_{pen} = (N_{in} - N_{ex}) / A_{pen} \qquad (4\text{-}5)$$

Figure 4-5 shows the displacement current obtained during three consecutive cyclic sweeps. Table 4-1 lists the average injected, extracted, and trapped carrier densities for each sweep. About 6% of carriers injected into pentacene were trapped in the first sweep. The average trapped carrier density in the first sweep was more than 5 times as high as that in the second sweep. The shift between the peaks in the first and second sweeps was caused by the carriers trapped in the first sweep. The shift between the peaks in the second and the third sweeps was smaller, because fewer carriers were trapped in the second sweep than in the first sweep (Table 4-1).

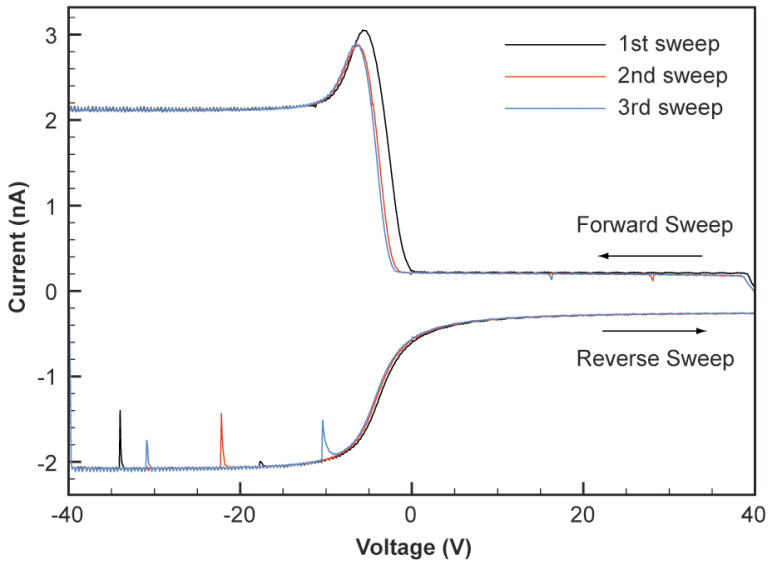

Figure 4-5 Displacement current measured from a pentacene LCC during three consecutive cyclic voltage sweeps.

Table 4-1 Average injected, extracted, trapped carrier densities, and percentage of trapped carriers over total injected carriers in each consecutive cyclic sweep shown in Figure 4-5.

	Injected ($\times 10^{12}$ cm^{-2})	Extracted ($\times 10^{12}$ cm^{-2})	Trapped (cm^{-2})	Trapped (%)
First sweep	2.80	2.64	1.61×10^{11}	5.76%
Second sweep	2.65	2.62	3.02×10^{10}	1.14%
Third sweep	2.62	2.60	2.63×10^{10}	1.00%

4.6 Device models (developed by Hsiu-Chuang Chang and Prof. P. Paul Ruden)

4.6.1 Geometry model

Only drift current is considered in the geometry model. Also for now, the background current associated with the contact is not considered. In the forward sweep, the front of the carrier sheet is assumed to be moving at a *constant* speed, μE, during the transient carrier transport, where μ is the carrier mobility, and E is the in-plane electric field. In addition, the carrier distribution profile in the channel follows a straight line, as shown in Figure 4-6a. Because the carrier density at the contact, $p(0,t)$, changes linearly with time, the slope of the profile line in Figure 4-6a should be constant. Based on the gradual channel approximation,[44] the electric field within the carrier sheet is

$$E(x,t) = -\frac{e}{C'}\frac{\partial p(x,t)}{\partial x} \qquad (4\text{-}6a)$$

where C' is the capacitance per unit area of SiO_2. Because $\partial p(x,t)/\partial x$ is constant, we have

$$E = \frac{e}{C'}\frac{p(0,t)}{\mu E t} \qquad (4\text{-}6b)$$

Insert $p(0,t) = C'V/e = C'r_V t/e$ into Equation 4-6b, we have $E = r_V/\mu E$. Solving this simple equation, we have

$$E = \sqrt{r_V/\mu} \qquad (4\text{-}7)$$

The displacement current at $x = 0$ is

$$I(0,t) = eW\mu p(0,t)E \tag{4-8}$$

Insert Equation 4-7 into Equation 4-8, we get

$$I(0,t) = WC' r_V^{3/2} \mu^{1/2} t \tag{4-9}$$

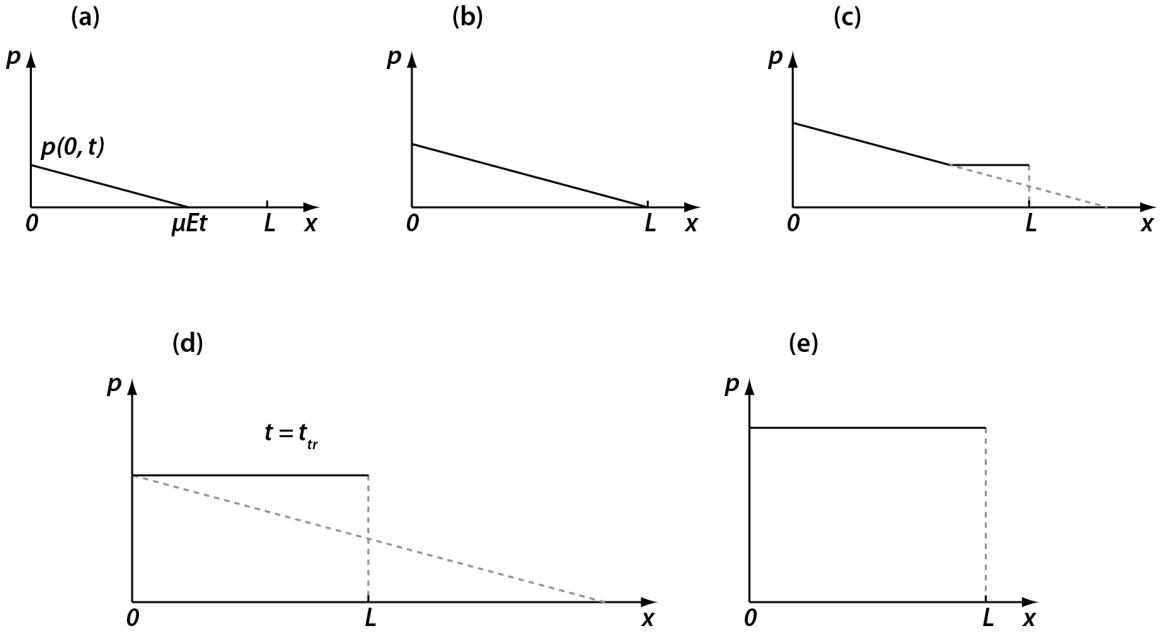

Figure 4-6 Evolution of charge carrier distribution in the channel during the forward sweep based on the geometry model.

After the front of the carrier sheet reaches the other end of the channel at $x = L$, carriers bounce back, so that a region of uniform carrier distribution is seen in Figure 4-6c. Later, the width of this region increases, and eventually the carrier density in the whole channel becomes uniform, as shown in Figure 4-6d. We call the time at which the situation in Figure 4-6d occurs the transient time t_{tr} ($t_{tr} = 2L/\mu E = 2L/\sqrt{\mu r_V}$). When $t < t_{tr}$, the electric field at $x = 0$ remains unchanged, so that the displacement current still follows the Equation 4-9. When $t > t_{tr}$, the carrier density everywhere in the channel increases uniformly with time (Figure 4-6e), so that the displacement current becomes:

$$I(0,t) = \frac{dQ}{dt} = eWL\frac{dp(0,t)}{dt} = WLC'r_V \qquad (4\text{-}10)$$

During the reverse sweep, carriers are extracted from the channel. At any time, the carrier distribution is assumed to be uniform in the channel, as shown in Figure 4-7. So that the displacement current still follows Equation 4-10, with an opposite sign.

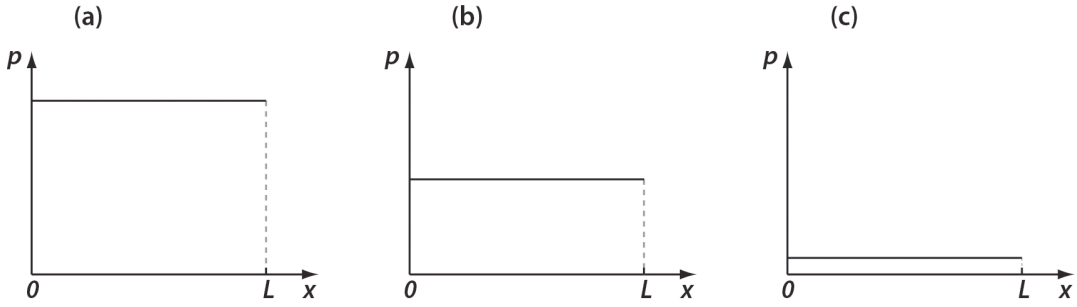

Figure 4-7 Evolution of charge carrier distribution in the channel during the reverse sweep based on the geometry model.

The calculated I-V characteristics based on the geometry model are shown in Figure 4-8, with the background current associated with the contact added to the forward and reverse sweeps. (The channel length and width are 6 mm and 0.5 mm, respectively.) Based on the geometry model, the existence of the displacement current peak in the forward sweep is due to the transient transport of carriers in the channel. In addition, the slope of the displacement current peak can be related to the carrier mobility.

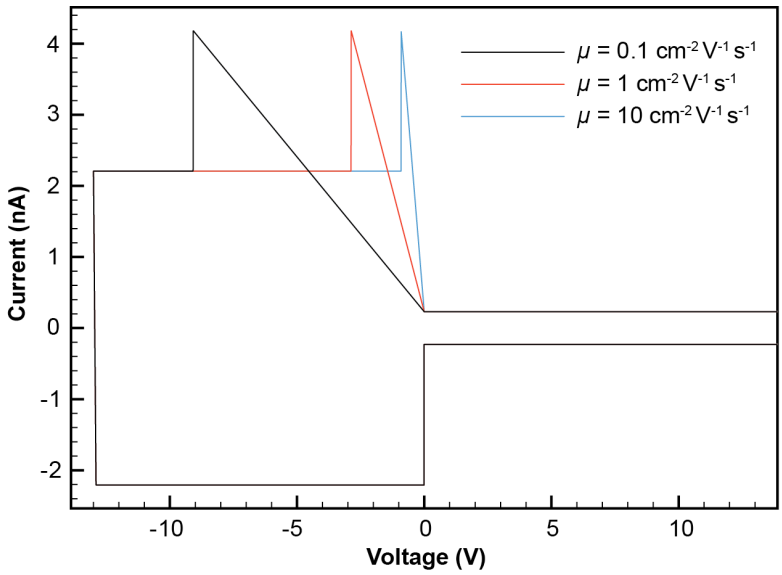

Figure 4-8 Calculated I-V characteristics based on the geometry model. (Data courtesy of Hsiu-Chuang Chang.)

From Equation 4-9, the slope of the displacement current peak G is

$$G = dI/dV = WC' r_V^{1/2} \mu^{1/2} \qquad (4\text{-}11)$$

Rearrange Equation 4-11, we get

$$\mu = \frac{G^2}{r_V W^2 C'^2} \qquad (4\text{-}12)$$

Equation 4-12 provides a simple way to calculate the mobility from displacement current curves. (Its validity will be tested by the numerical model in Section 4.4.2.) For example, the slope of displacement current peak in Figure 4-3 is about 0.81 nAV^{-1}, corresponding to a carrier mobility of 0.3 $cm^2V^{-1}s^{-1}$ calculated with Equation 4-12. The field-effect mobility obtained from the DC measurements of a pentacene OFET made in the same run on the same substrate was 0.2 $cm^2V^{-1}s^{-1}$. The two values are in reasonable agreement.

Figure 4-9a shows the displacement current curves taken at different voltage sweep rates. According to Equation 4-11, G^2 should be proportional to r_V. The linear relationship between G^2 and r_V can be clearly seen in Figure 4-9b, which provides solid support for the geometry model.

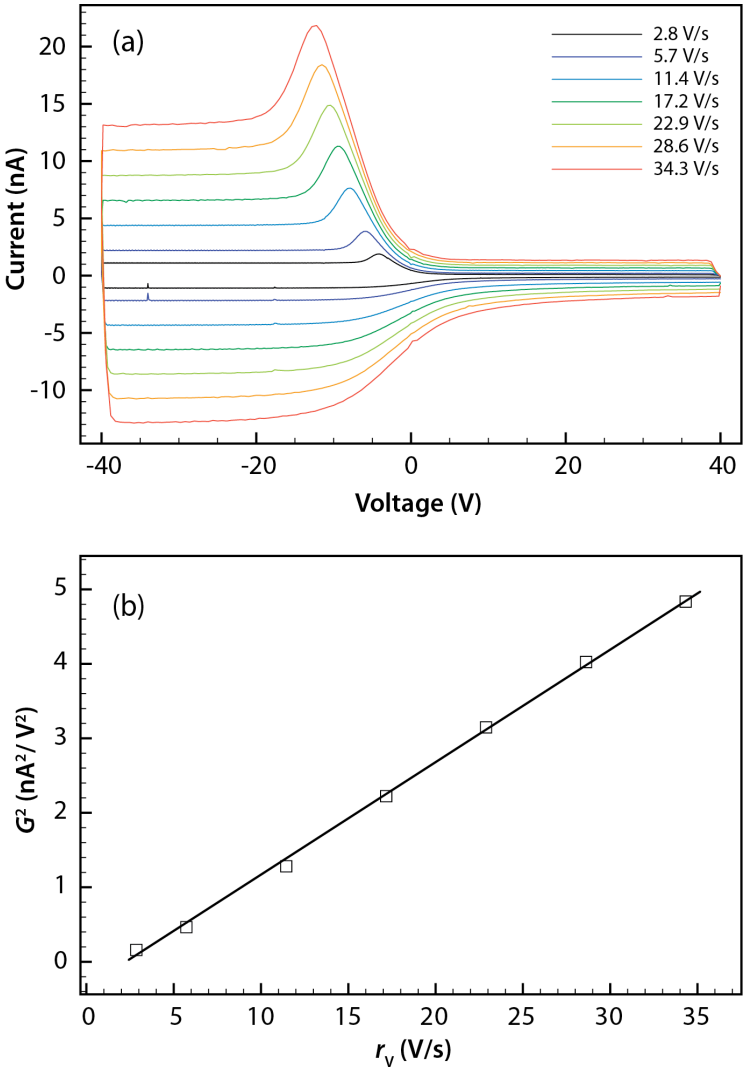

Figure 4-9 (a) Displacement current taken at different sweep rates. The device under measurement was a pentacene LCC with a Cu contact. (b) Plot of G^2 *vs.* r_V.

Nevertheless, there are many limitations in the geometry model. For example, after the front of the carrier sheet reaches $x = L$, the kink in Figure 4-6c is unrealistic. Instead, the carrier distribution in the channel should be close to the red line shown in Figure 4-10a. In addition, the electric field at $x = 0$ should gradually change to zero, giving rise to the smooth peak as seen in the experimental data (Figure 4-3). More information regarding the carrier distribution during the conducting channel formation will be discussed in Section 4.2.2.2. During the reverse sweep, the carriers away from the contact travel longer to get out of the channel than those near the contact. At some point, the carrier distribution in the channel should not be uniform anymore, as shown by the red line in Figure 4-10b. As we will see in Chapter 6, the non-uniform distribution leads to the S-shaped transition region in the reverse sweep in the experimental data (Figure 4-3).

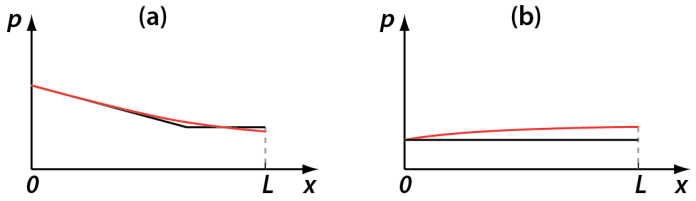

Figure 4-10 Limitations of the geometry model. Black lines are based on the geometry model. Red lines are more realistic approximations. (a) Carrier distribution at a certain time during the forward sweep. (b) Carrier distribution at a certain time during the reverse sweep.

4.6.2 Numerical model

4.6.2.1 Description of the model

As shown in Figure 4-2, the x-axis is parallel to the pentacene strip with its origin at the edge of the gold contact. Because the device has lateral dimensions that are large compared to the oxide thickness, the gradual channel approximation is used in the model.[44] (For the devices discussed in this chapter no fixed charge gave rise to a non-zero threshold voltage for the first sweep. Subsequent sweeps, however, were affected by

trapped holes as seen in Figure 4-5.) The local charge in the channel is related to the local voltage drop across the SiO_2,

$$V(x) = -(V_G - V_{channel}(x)) \tag{4-13}$$

$$e[p(x) + p_T(x)] = C'V(x),\ V(x) \geq 0 \tag{4-14}$$

where $p(x)$ is the sheet density of mobile holes, $p_T(x)$ is the sheet density of trapped holes, C' is the SiO_2 capacitance per unit area, e is the elementary charge, and $V(x)$ is the voltage difference between the channel and gate electrode. The lateral electric field in the channel is

$$E(x) = -\frac{dV_{channel}(x)}{dx} \tag{4-15}$$

The current density due to drift and diffusion is,

$$J_p = e\mu_p pE - eD\frac{\partial p}{\partial x} \tag{4-16}$$

where μ_p is the hole mobility, D is the hole diffusivity related to the mobility by the Einstein relationship. As holes are injected from the electrode into the pentacene, the sheet density of mobile holes varies with time according to the continuity equation,

$$\frac{\partial p}{\partial t} = -\frac{1}{e}\frac{\partial}{\partial x}J_p + \left.\frac{\partial p}{\partial t}\right|_{traps} \tag{4-17}$$

After combining Equations (4-13)–(4-17), the sheet density of mobile holes at position x and time t satisfies:

$$\frac{\partial p}{\partial t} = \frac{e\mu_p}{C'}\left[\frac{\partial}{\partial x}\left(p\frac{\partial p}{\partial x}\right) + \frac{\partial}{\partial x}\left(p\frac{\partial p_T}{\partial x}\right)\right] + D\frac{\partial^2 p}{\partial x^2} + \left.\frac{\partial p}{\partial t}\right|_{traps} \qquad (4\text{-}18)$$

The sheet density of trapped holes is controlled by the total (sheet) density of trap states N_T, the capture coefficient $\tilde{c}$, and the emission coefficient $\tilde{e}$,

$$\frac{\partial p_T}{\partial t} = \tilde{c}p(N_T - p_T) - \tilde{e}p_T = -\left.\frac{\partial p}{\partial t}\right|_{traps} \qquad (4\text{-}19)$$

To solve the device problem of the coupled differential Equations 4-18 and 4-19, the equations are discretized and integrated subject to the initial and boundary conditions imposed.

At $t = 0$, no holes exist in the pentacene channel,

$$p(x,t=0) = p_T(x,t=0) = 0 \qquad (4\text{-}20)$$

Since the current vanishes at the end of the device, the boundary condition at $x = L$ is

$$\left.\frac{\partial p}{\partial x}\right|_L = \left.\frac{\partial p_T}{\partial x}\right|_L = 0 \qquad (4\text{-}21)$$

When bias is applied and holes are injected into the channel, the following condition at the contact holds:

$$e[p(x=0,t) + p_T(x=0,t)] = C'V(x=0,t) \qquad (4\text{-}22)$$

where $V(x=0,t) = -V_G(t) = -(V_G(t=0) - r_V t)$.

The current density going into the contact at $x = 0$ may be calculated either by monitoring the rate of increase of the integrated free and trapped holes in the pentacene or by directly evaluating J_p from Equation 4-16 at $x = 0$.

$$\begin{aligned} J_p &= e\frac{\partial}{\partial t}\int_0^L [p(x,t) + p_T(x,t)]dx \\ &= \frac{e^2}{C'}\mu_p p(0,t)\left[\frac{\partial p(0,t)}{\partial x} + \frac{\partial p_T(0,t)}{\partial x}\right] + eD\frac{\partial p(0,t)}{\partial x} \end{aligned} \tag{4-23}$$

For all the simulation results below, the channel capacitance is $C' = 11.5$ nFcm^{-2}, channel length is $L = 5.88$ mm, and $r_V = 5.732$ Vs^{-1}. We first consider the situation in which no traps exist in the channel. From Equations 4-14 and 4-23 it is readily seen that the ratio of current due to drift to current due to diffusion is approximately:

$$\frac{J_p^{drift}}{J_p^{diffusion}} = \frac{e|V_B|}{k_B T} \tag{4-24}$$

where k_B is the Boltzmann constant, and T is the temperature. Evidently, diffusion plays a role only at the very beginning of the channel formation, *i.e.* when $|V_B(t)|$ is of order $k_B T$. Subsequently, the drift current dominates.

Figure 4-11 shows the simulated displacement current curves using different hole mobilities of 0.1, 1, and 10 cm^{2}V^{-1}s^{-1}. As shown in the figure, carrier mobility can greatly affect the transient processes in both forward and reverse sweeps. In the forward sweep, larger hole mobility leads to smaller and narrower peaks; in the reverse sweep, larger hole mobility results in faster extraction of carriers from the channel. It is notable that a good linear region exists in the forward sweep between the onset and the maximum of the displacement current peak. We have calculated mobilities with Equation 4-12 from the simulated displacement current curves and compared them to the actual mobilities used in the simulation. It is found that when the mobility is in the range of from 0.001 to 2 cm^{2}V$^-$

$^{1}s^{-1}$, the mobility calculated with Equation 4-12 is in very good agreement with the actual mobility used in simulation.

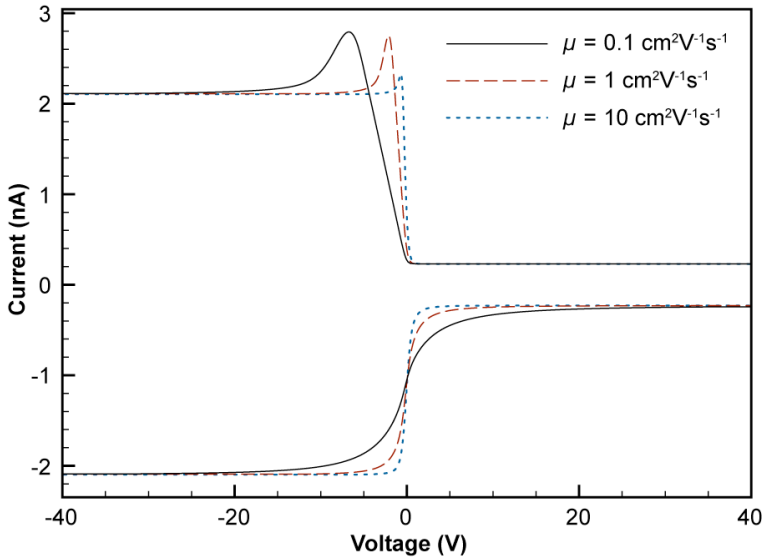

Figure 4-11 Simulated displacement current curves with different hole mobilities. (Data courtesy of Hsiu-Chuang Chang.)

4.6.2.2 Evolution of the carrier distribution in the channel during conducting channel formation

Figure 4-12a shows the current peak region in the simulated displacement current curve (μ = 0.1 $cm^2V^{-1}s^{-1}$) plotted against both voltage and time (t = 0 at V_G = 0). As we have discussed in the geometry model, the current peak corresponds to the transient process of conducting channel formation. Figure 4-12b shows the corresponding carrier distribution profiles in the channel from t = 0.2 s to t = 3.0 s calculated by the numerical model, with an interval of 0.2 s. The 0% position corresponds to the contact end, and the 100% position corresponds to the other end of the channel. Several characteristics can be seen from the Figure 4-12.

From 0.2 s to 0.8 s, the carrier distribution profiles in the channel are straight lines with a constant slope. This characteristic is the same as that in the geometry model (Figures 4-6a and 4-6b).

From 0.8 s to 1.0 s, no obvious change occurs in the slope of the profile line at the contact end, but the profile lines become flatter near the other end of the channel. Unlike the geometry model (Figure 4-6c), no kink on the profile line is observed.

From 1.0 to 3.0 s, the flatter region in the profile line expands toward the contact end, and the slope of the profile line at the contact end decreases, in contrast to the constant slope proposed in the geometry model. The carrier distribution in the channel becomes more and more uniform during this period. At 3.0 s, the carrier density at the contact end is higher than that at the other end by only 3.7%.

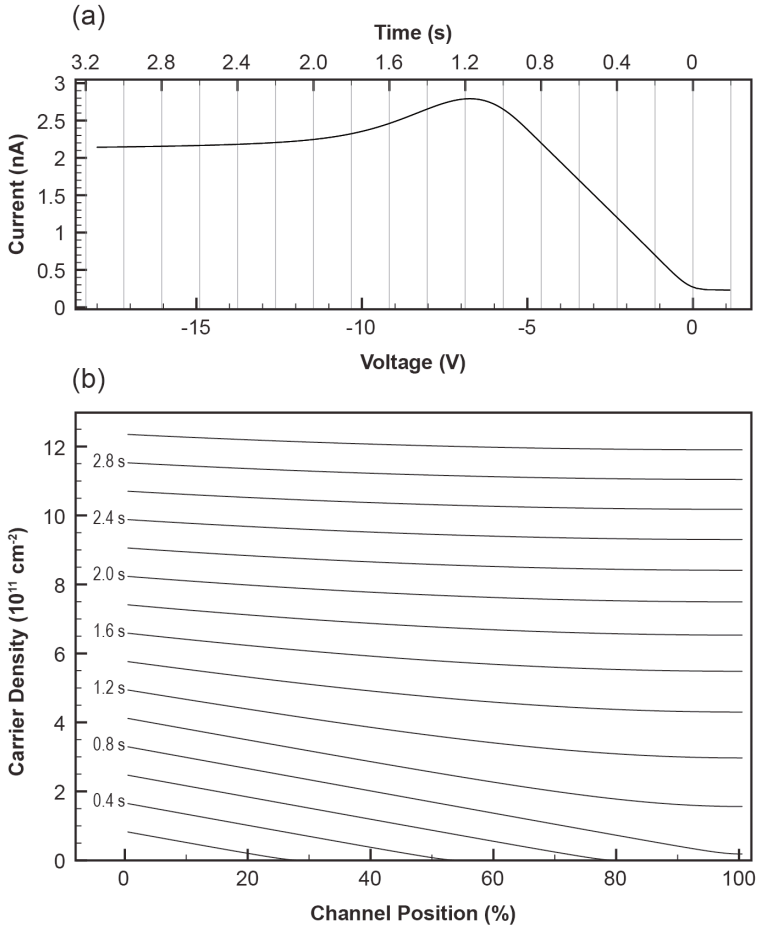

Figure 4-12 (a) Simulated displacement current curve plotted against gate voltage and time (t = 0 at V_G = 0). (b) The corresponding calculated carrier distribution profiles in the channel from 0.2 to 3.0 s with an interval of 0.2 s. (Data courtesy of Hsiu-Chuang Chang.)

Comparing Figure 4-12 to Figure 4-6 based on the geometry model, we can see that the geometry model successfully describe the carrier distribution at the beginning of the conducting channel formation. However, it fails to predict the slow decease of the slope of the profile line at the contact end, and hence the smooth displacement current peak.

4.6.2.3 Effects of carrier traps on displacement current

When carrier traps are included in the numerical model, three parameters need to be considered: total available trap states (N_T), capture coefficient ($\tilde{c}$), and emission coefficient ($\tilde{e}$).The product of N_T and $\tilde{c}$ determines how fast free carriers are being trapped, so that $\tilde{c}N_T$ can be treated as a single parameter as long as $p_T << N_T$. We define the capture time $\tau_{cap} = 1/(\tilde{c}N_T)$, and emission time $\tau_{emi} = 1/\tilde{e}$. When discussing the effects of the traps, it is often useful to compare τ_{cap} and τ_{emi} with the transient time (t_{tr}) for the conducting channel formation. t_{tr} can be estimated with the geometry model, that is $t_{tr} = 2L/\sqrt{\mu r_V}$.

We should keep in mind that it is rather difficult to fit the experimental data with the numerical model for two reasons. (1) There are too many parameters in the numerical model to get meaningful fitting. (2) The current numerical model only considers single-energy-level carrier traps. In reality, however, carrier traps should exist at multiple energy levels. Nevertheless, two examples are given below to illustrate the effects of τ_{cap} and τ_{emi} on the displacement current behaviors. In the both examples, we use μ = 1 $cm^2V^{-1}s^{-1}$, giving rise to t_{tr} = 0.5 s.

Example 1. In this example τ_{cap} = 10 s, and τ_{emi} = 0.01 s, 2 s, and 1000 s. Because τ_{cap} is much larger than t_{tr}, only a few carriers are trapped during the conducting channel formation. As a result, the shape of the displacement current peak in the forward sweep is not affected, as shown in Figure 4-13. In the reverse sweep, the shape of the displacement current curve is dependent on τ_{emi}. For τ_{emi} = 0.01 s, most of the carriers can be quickly emitted once they are trapped. As a result, the displacement current curve shows little difference from that of the no-trap case (they overlap each other in Figure 4-13). For τ_{emi}

= 1000 s, the trapped carriers cannot be emitted during the time scale of the simulation. As a result, the S-shaped displacement current curve in the reverse sweep is shifted negatively by about 4 V. For τ_{emi} = 2 s, some, but not all trapped carriers can be emitted during the simulation. As a result, the S-shaped displacement current curve is still shifted negatively compared to that of the no-trap case, but the shift is smaller than that for τ_{emi} = 1000 s. In addition, the carriers being emitted from the traps contribute to the displacement current higher than the background at the end of the reverse sweep.

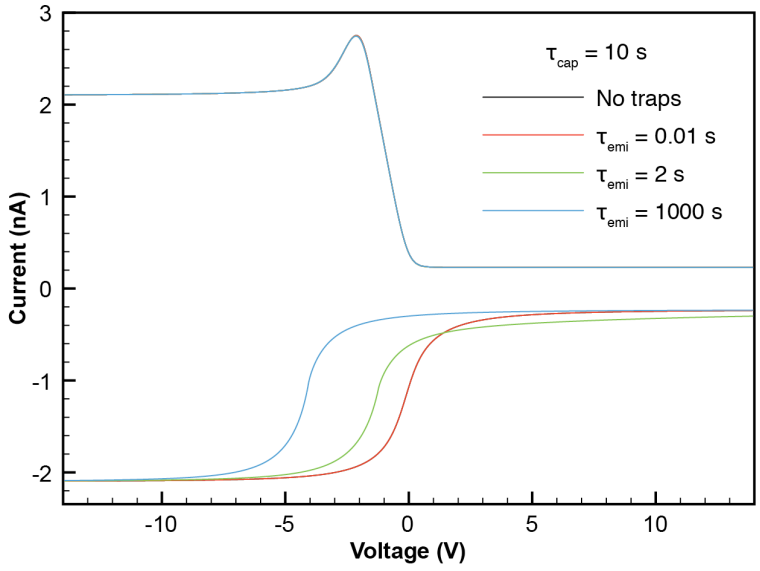

Figure 4-13 Simulated displacement current curves with τ_{cap} = 10 s, and τ_{emi} = 0.01 s, 2 s, and 1000 s. In this example, $\tau_{cap} + \tau_{emi} >> t_{tr}$. Simulated displacement current curve with no traps is also shown. It overlaps with the curve with τ_{cap} = 10 s, and τ_{emi} = 0.01 s. (Data courtesy of Hsiu-Chuang Chang.)

Example 2. In this example τ_{cap} = 0.01 s, and τ_{emi} = 0.02 s, 0.04 s, and 0.08 s. Because both τ_{cap} and τ_{emi} are much smaller than t_{tr}, trapping and detrapping processes occur during conducting channel formation. As a result, the slope of the displacement current peak in the forward sweep is smaller than that of the no-trap case, as shown in Figure 4-14. In other words, the effective mobility is reduced because of the presence of

carrier traps. In addition, we expect the fast trapping and detrapping processes are in equilibrium during the transient transport, so the effective mobility can also be calculated with

$$\mu = \mu_0 \tau_{cap} / (\tau_{cap} + \tau_{emi}) \qquad (4\text{-}25)$$

where $\mu_0 = 1$ cm^{2}V^{-1}s^{-1}. In Table 4-2, we list the carrier mobilities calculated from the slopes of the displacement current peaks with Equation 4-12, and the carrier mobilities calculated with Equation 4-25. We find that the mobility values calculated from the two methods are almost identical, indicating the trapping and detrapping are indeed in equilibrium. In the reverse sweep, the displacement current is also dependent on τ_{emi}. As τ_{emi} increase, the width of the transient region increases.

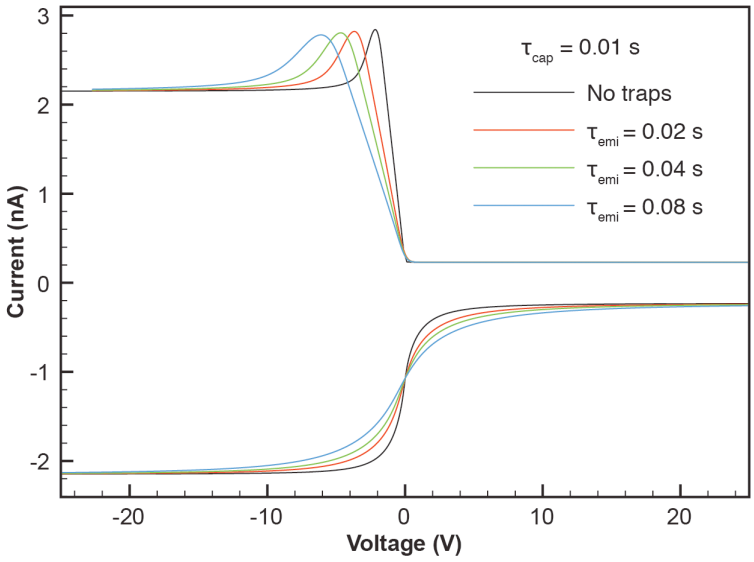

Figure 4-14 Simulated displacement current curves with $\tau_{cap} = 0.02$ s, and $\tau_{emi} = 0.01$ s, 0.04 s, and 0.08 s. In this example, $\tau_{cap} + \tau_{emi} << t_{tr}$. Simulated displacement current curve with no traps is also shown. (Data courtesy of Hsiu-Chuang Chang.)

Table 4-2 Comparison of the mobility values calculated from Equations 4-12 and 4-25

τ_{emi} (s)	μ ($cm^2V^{-1}s^{-1}$) (Calculated with Equation 4-12)	μ ($cm^2V^{-1}s^{-1}$) (Calculated with Equation 4-25)
0.02	0.35	0.33
0.04	0.21	0.20
0.08	0.12	0.11

We believe Example 2 is more relevant to the experiment. That is, the mobility calculated from the experimental data by using Equation 4-12 including the effect of carrier traps. The "native" mobility of the material free of traps should be higher than the measured mobility.

4.7 Conclusion

We have presented here a device called a long-channel capacitor (LCC) for examining displacement current to study the transient carrier behaviors during conducting channel formation and depletion. A LCC only has one channel contact to limit the carrier injection/extraction to one direction, and the channel length is in millimeter range to increase the transient time and the displacement current associated with charging and discharging the channel. The displacement current also provides information about the densities of carriers injected into, extracted from, and trapped inside the pentacene film during the device operation.

We have described a simplified geometry model to explain the displacement current peak observed in the I-V characteristics. A more sophisticated numerical model has also been given to describe the evolution of the carrier distribution in the channel during the conducting channel formation. Based on the geometry model, the transient carrier mobility (μ) can be estimated from the slope of the displacement current peak (G). We have also described a numerical model and confirmed that the simple relationship between μ and G obtained from the numerical model (Equation 4-12) is usable if mobility is in the range from 0.001 to 2 $cm^{-2}s^{-1}V^{-1}$. Finally, the effects of traps on the displacement current behaviors were discussed with the numerical model.

5 Examination of contact effects in organic field-effect devices via displacement current measurement

5.1 Introduction

Displacement current measurement (DCM)[3, 5, 6, 9, 45, 46] is one of the a few techniques[35, 36, 39-41, 43] that can be used to study the transient processes in organic field-effect transistors (OFETs). These transient processes, including the formation and depletion of the conducting channel in OFETs, are essential parts of the device operation and determine the response frequency of OFETs. However, they are often overlooked during steady state or quasi steady state DC measurements.[17-20, 24]

In this chapter, we intend to expand the application of DCM and use it to study carrier injection and extraction at the metal-organic interface in OFETs. Previous studies have shown that the simplistic energy band diagrams between metals and organic semiconductors are often complicated by the variation of metal Fermi energy,[47] interfacial dipoles,[47-49] metal penetration,[47, 50, 51] and microstructures of the organic semiconductor films.[52-54] When traditional DC measurements are used to study the carrier injection and extraction in OFETs, a challenge arises since these two processes occur simultaneously during the measurements. On the contrary, the injection and extraction processes are naturally separated during displacement current measurement. Moreover, the number of injected, extracted, and trapped carriers can be calculated by integrating the displacement current with respect to time, providing additional information for understanding the carrier injection and extraction processes.

Instead of using OFETs for measuring displacement current, we use long-channel capacitors (LCCs).[45, 46] A LCC can be seen as a simplified OFET with only one channel contact to limit the carrier injection/extraction to one direction only. The channel of a LCC is elongated to millimeter range to increase the transient time and the displacement current associated with charging and discharging the channel.

In our experiments, three metals, Au, Cu, and Al, were used as the channel contacts in pentacene LCCs. Au is the most widely used contact material for pentacene OFETs. However, Au penetration often occurs in top-contact devices and may result in detrimental effects on device performance.[47, 51] With DCM, it is possible to explore the effects of Au penetration on the carrier injection and extraction during the conducting channel formation and depletion. Recent reports have shown that pentacene OFETs with Cu contacts exhibit better performance than those with Au contacts.[55-57] By comparing the displacement current of Cu and Au devices, we hope to understand why Cu contacts are better than Au contacts. Al is not an efficient hole-injection material for pentacene due to its low work function. However, ambipolar injection has recently been observed in pentacene transistors with Al contacts.[7, 58] We want to confirm the ambipolar injection in pentacene LCCs with Al contacts. Since electron trapping is generally more severe than hole trapping at the semiconductor-dielectric interface,[59] we want to explore the possible effect of trapped electrons on hole injection.

5.2 Experiment

The schematic structure of a long-channel capacitor (LCC) used in this study is shown in Figures 5-1a and 5-1b. The substrate was a heavily doped p-type Si wafer with 300 nm SiO_2. The heavily doped Si also served as the gate electrode. Shadow masks were used to pattern both the pentacene and metal films. During the pentacene deposition, the deposition rate was 0.1–0.2 $Å s^{-1}$, and the substrate temperature was 30 °C. The thickness of the pentacene film was either 30 or 100 nm. The typical size of the pentacene strip in a LCC was 0.5 mm × 6.0 mm. The 40 nm thick metal contact was deposited on the pentacene by thermal evaporation while the substrate was water-cooled. The deposition rate was 0.5–1.0 $Å s^{-1}$ for Au and Cu, and 2.0–3.0 $Å s^{-1}$ for Al. The width of the overlapping area between metal and pentacene is typically 0.1–0.2 mm. In a single run, 34 LCCs were made on the same chip, as showed in Figure 5-1c. To study the dependence of displacement current on pentacene thickness for a certain metal, two types of pentacene strips with different thicknesses (30 and 100 nm) were deposited separately, and the metal contacts of all the devices were deposited in a single deposition. The device

chip is schematically shown in Figure 5-1c, with different pentacene colors representing different pentacene thicknesses.

All electrical measurements were performed in the dark in a vacuum probe station. A Keithley 2612 dual-channel SourceMeter was used to characterize the LCCs, with one channel applying voltage sweeps on the gate electrode, and the other channel measuring the displacement current running through the grounded channel contact. The voltage sweep rate was 5.7 Vs^{-1}. Two *consecutive* cyclic voltage sweeps were performed on each device during the measurement. Each cyclic sweep comprised a *forward* sweep (usually from +40 V to –40 V) and a *reverse* sweep (usually from –40 V to + 40 V).

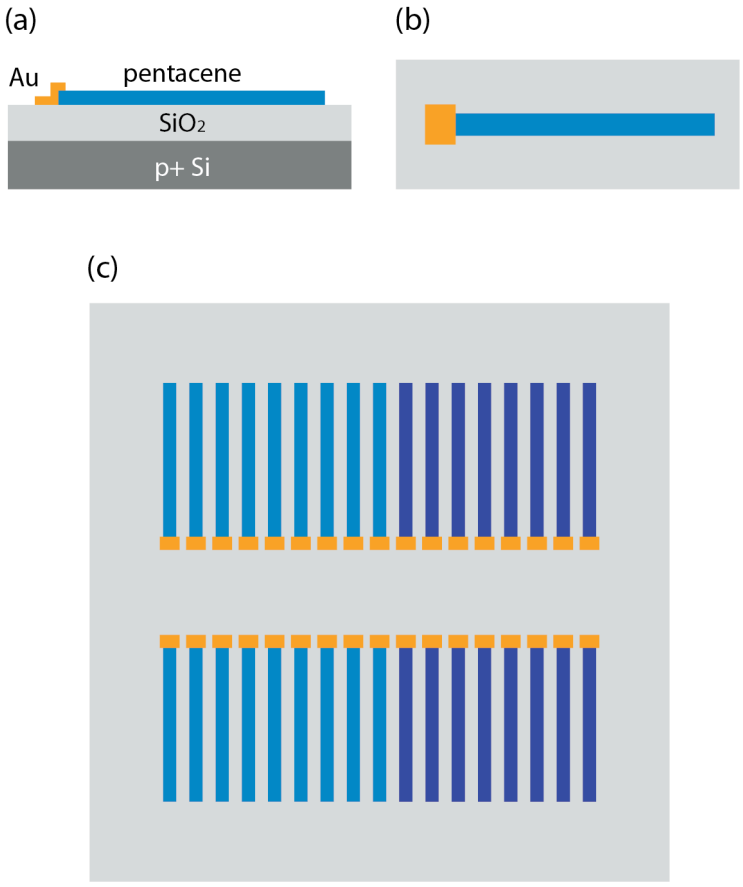

Figure 5-1 (a) Schematic cross section of a pentacene long-channel capacitor (LCC). (b) Schematic top view of the device. (c) A device chip containing 34 LCCs used in this study. Different pentacene colors represent different pentacene thicknesses.

5.3 Carrier injection, extraction, and trapping in devices with Au and Cu contacts

Figures 5-2a and 5-2b show the displacement current taken from the devices with Au and Cu contacts, respectively. Red curves represent the displacement current taken from the devices with 30 nm pentacene, and black curves from the devices with 100 nm pentacene. For the sake of simplicity, we call the Au devices with 30 nm and 100 nm pentacene Au/30Pen and Au/100Pen, respectively. Similarly, the Cu devices with 30 nm and 100 nm pentacene are called Cu/30Pen and Cu/100Pen, respectively.

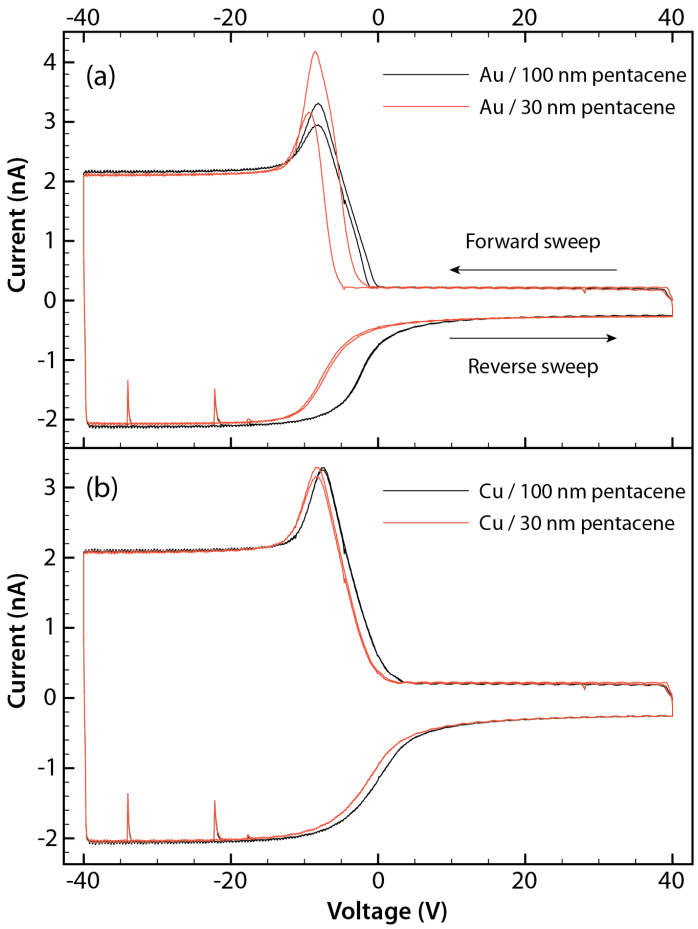

Figure 5-2 Displacement current measured from LCCs with (a) Au and (b) Cu contacts. For each metal, two different pentacene thicknesses were used, which were 30 nm (black lines) and 100 nm (red lines). Each measurement consisted of two consecutive cyclic voltage sweeps.

During the displacement current measurement, the hole injection occurred in the forward sweep (+40 to –40 V), whereas the hole extraction occurred in the reverse sweep (–40 to +40 V). By integrating the displacement current with respect to time, the total number of the carriers injected into the pentacene strip during the forward sweep, and the total number of the carriers extracted from the pentacene strip during the reverse sweep can be calculated,[45] as shown in Figure 5-3a. The difference between the two is the total number of the carriers trapped inside the pentacene after one cyclic sweep. Dividing the number of the trapped carriers with the area of the pentacene channel gives the average trapped carrier density. Figure 5-3b shows the average trapped carrier densities after the first cyclic sweep for all the devices in Figure 5-2.

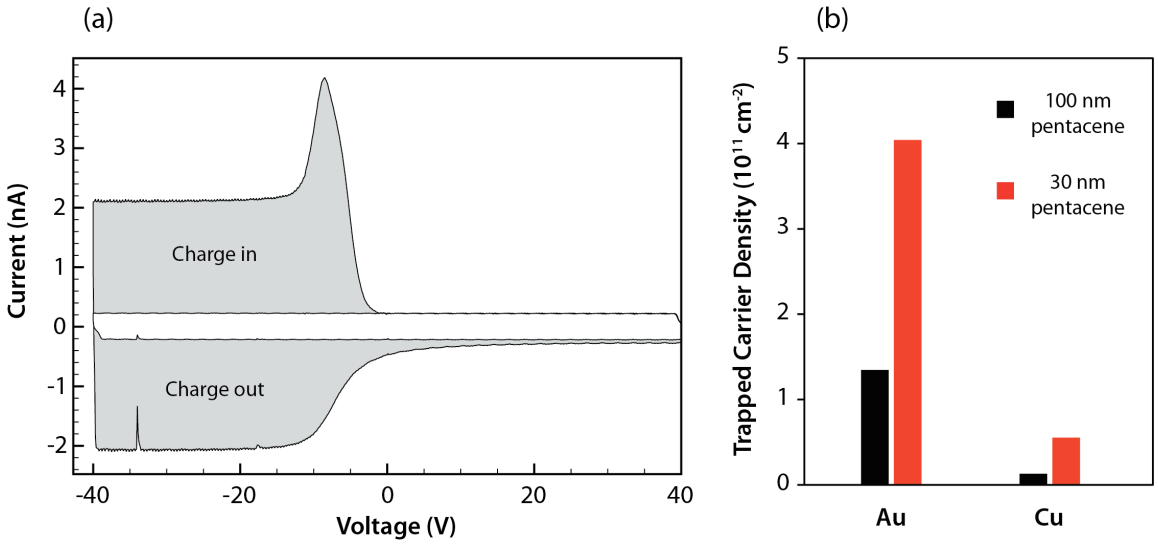

Figure 5-3 (a) The total number of injected and extracted carriers can be calculated by integrating the displacement current with respect to time.[11] (b) Average trapped carrier densities after the first cyclic sweep for the devices in Figure 5-2.

As shown in Figure 5-2a, the displacement current of the devices with Au contacts was dependent on pentacene thickness. During the first cyclic sweep, the hole injection started later for Au/30Pen than for Au/100Pen, as indicated by the more negative onset of the displacement current peak for Au/30Pen. The injection rate, which

was identical to the value of the displacement current, was lower for Au/30Pen from 0 to –5 V, but was higher afterwards until the displacement current reached the flat region. At the end of the forward sweep, the densities of the carriers injected into the pentacene strips was similar for the both devices. In the reverse sweep, the S-shaped displacement current curve was negatively shifted for Au/30Pen compared to the displacement current curve for Au/100Pen. As a result, fewer carriers were extracted from Au/30Pen, and more carriers were trapped at the end of the first cyclic sweep. As shown in Figure 5-3b, the trapped carrier density at the end of the first cyclic sweep was 4.0×10^{11} cm^{-2} for Au/30Pen, which was about 3 times as high as that for Au/100Pen (1.3×10^{11} cm^{-2}). The trapped carriers in the channel delayed the carrier injection in the second cyclic sweep, and hence shifted the onset of the displacement current peak negatively. Since more carriers were trapped in Au/30Pen, its onset shift was larger.

On the contrary, the displacement current of the devices with Cu contacts exhibited less dependence on pentacene thickness, as shown in Figure 5-2b. Similar as for the Au devices, the trapped carrier density for the Cu/30Pen was higher than that for Cu/100Pen. However, the trapped carrier density for either Cu device was much lower than that for the corresponding Au device with the same pentacene thickness, as shown in Figure 5-3b. As a result, there was a very small shift between the onsets of the displacement current peaks for Cu/30Pen, and no obvious shift was observed for Cu/100Pen.

5.3.1 Mechanism of carrier trapping

It is commonly believed that charge carrier trapping is caused by the trap states at the semiconductor-dielectric interface in the channel region. In our experiments, the density of these trap states should be roughly the same for all the devices because the same substrates, pentacene source, and pentacene deposition conditions were used. However, for the Au and Cu devices with the same pentacene thickness, a large difference in the trapped carrier density was observed, as shown in Figure 5-3b. In addition, for a certain metal, the trapped carrier density was dependent on the pentacene film thickness. These facts indicate that the trap states at the semiconductor-dielectric

interface in the channel region are not the only factor that causes carrier trapping in the channel. The effects of the contact should also be considered.

5.3.1.1 Carrier trapping in devices with Au contacts

To prove that carriers were trapped in the long channel, LCCs with Au contacts and different channel lengths were made. Figure 5-4 shows the total number of trapped carriers after the first cyclic sweep *vs.* channel length for one series of devices with 30 nm pentacene and the other series with 100 nm pentacene. As can be seen from the figure, the total number of trapped carriers increased with the channel length for the both series. In addition, the imaginary trend line of each series intercepts the *y*-axis at close to zero. These two facts indicate that the majority of the trapped carriers were in the long channel. The linear trend line for the series with 30 nm pentacene suggests that the distribution of trapped carriers was uniform in the long channel. The non-linear trend line for the series with 100 nm pentacene suggests that the distribution of trapped carriers in the long channel was not uniform, with more carriers trapped towards the end of the channel away from the contact. The reason for the different distributions is not clear. Finally, for each channel length, more carriers were trapped in the device with 30 nm pentacene than in the device with 100 nm pentacene, agreeing with the results in Figure 5-3b.

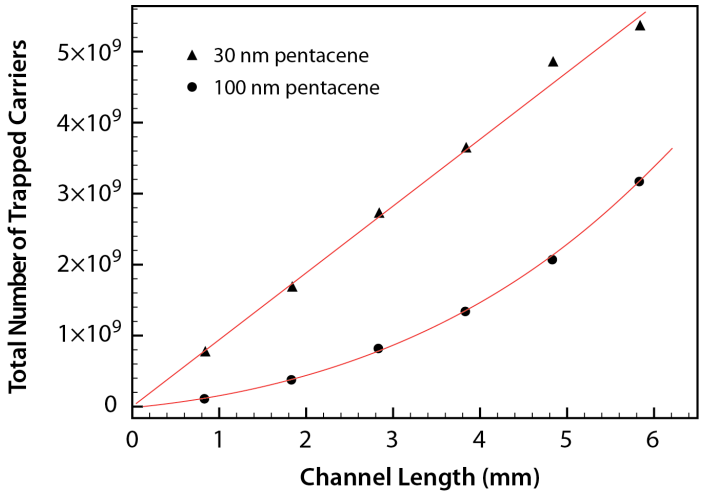

Figure 5-4 Total number of trapped carriers after the first cyclic sweep *vs.* channel length for Au devices with 30 nm (black triangles) and 100 nm pentacene (black circles). Red lines are imaginary trend lines.

Previous studies have demonstrated that Au atoms can penetrate organic semiconductor films when deposited from the vapor phase.[47, 50, 51] In addition, the penetrating Au atoms can generate deep trap states in pentacene.[55, 60, 61] In our experiments, it is highly possible that some Au atoms penetrate the pentacene film and reach the pentacene-dielectric interface, generating deep trap states at this interface. Since carriers are accumulated at the pentacene-dielectric interface during the device operation, we proposed that carrier trapping in the long channel is related to the deep trap states at the pentacene-dielectric interface generated by the penetrating the Au atoms. Depending on the pentacene film thickness, more deep traps are generated in Au/30Pen than in Au/100Pen, as shown by the white dots in Figures 5-5a and 5-5b.

In the forward sweep, the deep trap states at the pentacene-dielectric interface near the contact delay the carrier injection process because few free carriers can move into the channel region until these trap states were filled. This is more obvious for Au/30Pen because of the higher density of deep traps: the onset of its displacement current peak in the first cyclic sweep is more negative than that for Au/100Pen, as shown

in Figure 5-2a. However, the presence of these deep traps does not affect the density of the carriers injected into pentacene at the end of the forward sweep.

In the reverse sweep, carriers trapped in these deep trap states are emitted at a very slow rate, so that the density of the trapped carriers near the contact is not likely to change during the reverse sweep. When the carrier density in the long channel becomes lower than the density of the deeply trapped carriers near the contact, an energy barrier is formed, blocking the further extraction of carriers in the channel. As a result, *carriers are left in the channel not because of the trap states in the channel region, but because of the blockage effect of the deeply trapped carriers near the contact.* The density of the carriers trapped in the long channel should be close to the density of the deep traps near contact. As a result, Au/30Pen shows more trapping the channel region because of its higher density of the deep trap states near the contact (Figure 5-5).

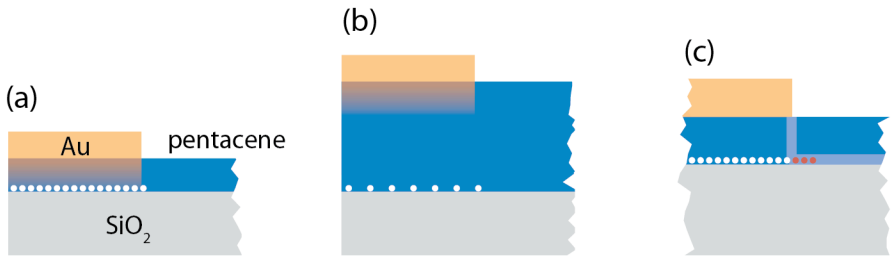

Figure 5-5 (a) and (b) Schematic diagrams illustrating the penetration of Au atoms into 30 nm and 100 nm pentacene, respectively. The white dots represent the deep trap states at the pentacene-dielectric interface generated by the penetrating Au atoms. (c) Most of the deep traps caused by Au penetration exist directly under the contact, as represented by the white dots. Some deep traps may extend into the channel due to the lateral diffusion of the penetrating Au atoms, as represented by the red dots. The carrier injection/extraction path is shown by the light blue line.

Most of the deep trap states exist directly under the contact, as shown by the white dots in Figure 5-5c. But some trap states may extend into the channel due to the lateral diffusion of the penetrating Au atoms,[62, 63] as shown by the red dots in Figure 5-5c. Because the carrier injection and extraction between the Au contact and the pentacene

channel are likely to occur at the contact edge as shown by the light blue path in Figure 5-5c, we propose that carrier trapping in the long channel is more sensitive to the deep trap states extended into the channel near the contact edge.

The proposed mechanism can be tested by changing the density of the traps near the contact edge but maintaining the density of traps under the contact. This can be achieved by angled Au deposition. Because of the finite thickness of the shadow mask (125 μm in our experiment), blurry and sharp edges are formed on deposited rectangular patterns if the deposition flux is not perpendicular to the substrate, as schematically shown in Figure 5-6a. The sharp and blurry edges can be easily distinguished under the microscope, as shown in Figures 5-6b and 5-6c. The formation of the blurry edges is due to the "shadow" area of the mask where the Au film is not continuous. The Au atoms in the shadow area introduce more deep traps near the blurry edge.

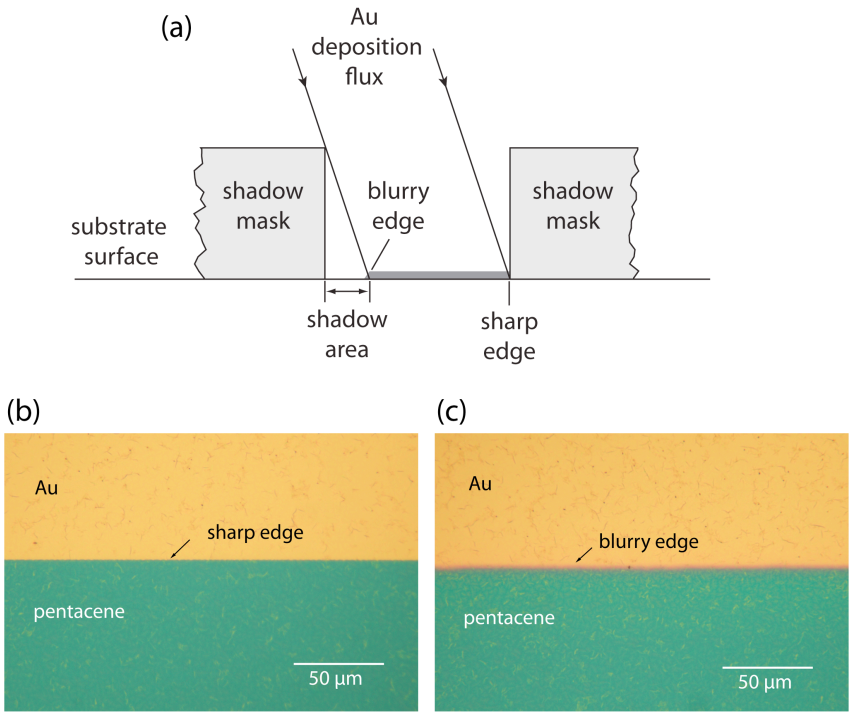

Figure 5-6 (a) Formation of sharp and blurry edges during angled Au deposition. (b) and (c) Microscope images of sharp and blurry Au contact edges on pentacene, respectively.

Because of the layout of our devices on the chip (Figure 5-1c), if the 17 LCCs in one row have blurry edges, the 17 LCCs in the other row must have sharp edges. So LCCs with blurry and sharp edges can be fabricated in a single run, ensuring the trap density under the contact is the same for all the devices. Figure 5-7 shows the displacement current measured from LCCs with blurry and sharp Au contact edges. In this case, the pentacene thickness was 30 nm. The trapped carrier density after the first cyclic sweep was about 3.5×10^{11} cm^{-2} for the device with the blurry edge, and 2.2×10^{11} cm^{-2} for the device with the shape edge. The differences in displacement current behaviors and trapped carrier densities indicate that carrier injection/extraction and carrier trapping in the long channel are more sensitive to the deep traps near the contact edge. (The above trapped carrier densities are not comparable to those in Figure 5-3b due to the large run-to-run variation for the LCC devices with the Au contacts.)

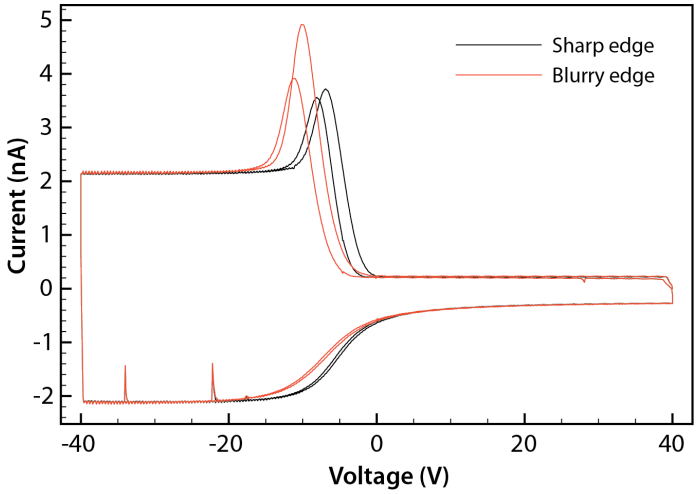

Figure 5-7 Displacement current measured from Au devices with sharp and blurry contact edges. The pentacene thickness was 30 nm.

In addition, a numerical model[45, 46] is used to prove that deep trap states near the contact edge can cause carrier trapping in the long channel. In our model, trap states are only present in a very narrow region near the contact (half Gaussian function with FWHM = 60 μm) and *no* traps exist elsewhere in the long channel (channel length = 6

mm). The total number of the trap states near the contact edge is 4.43×10^{8}. These trap states have relatively large emission time constant. Once they are filled, few trapped carriers can be emitted during the time scale of the simulation. In other words, these states behave as deep traps.

The red line in Figure 5-8 shows the simulation result for the device with the deep traps near the contact edge, whereas the black line for an ideal device with no traps. Just as the experimental data shown in Figure 5-2a, a higher displacement current peak is observed in the forward sweep for the device with deep traps near the contact edge. In the reverse sweep, fewer carriers are extracted from this device, as indicated by the smaller integrated area of the red curve. The total number of trapped carriers calculated by integrating the black displacement curve is 2.90×10^{10}, which is much larger than the total number of trap states near the contact edge (4.43×10^{8}). This result confirms that carriers are trapped in the long channel due to the presence of deep traps near the contact edge.

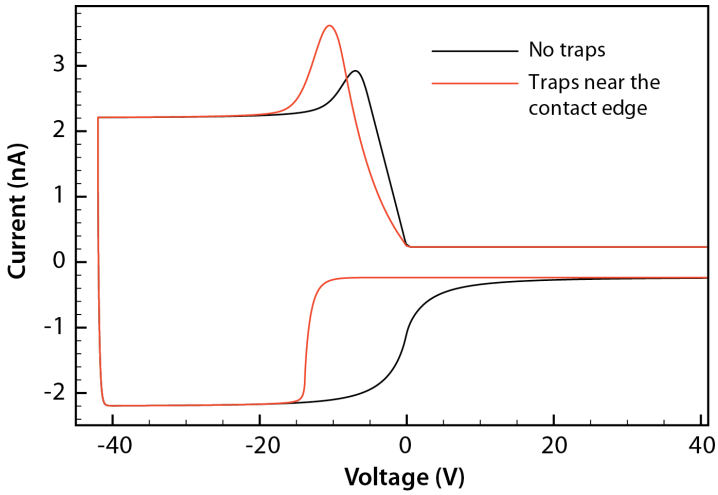

Figure 5-8 Numerical simulation results. Red curve is the simulation result for a device with traps only near the contact edge, and black curve is for an ideal device with no traps. (Data courtesy of Hsiu-Chuang Chang.)

5.3.1.2 Carrier trapping in devices with Cu contacts

Based on the above discussion for the Au devices, the low trapped carrier density for the Cu devices is likely due to the low density of the deep trap states at the pentacene-dielectric interface near the contact. One possible explanation is that the penetration of Cu atoms into pentacene is rather shallow, as shown in Figure 5-9, so that far fewer Cu atoms can reach the pentacene-dielectric interface and generate deep trap states. For Cu/30Pen, a small number of Cu atoms reach the pentacene-dielectric interface and generate deep traps there, resulting in carrier trapping in the channel region. However, the trapped carrier density (5.5×10^{10} cm^{-2}) for this device is still about 7 times as low as that for Au/30Pen (Figure 5-3b). For Cu/100Pen, even less deep traps are generated by Cu penetration, leading to the lowest trapped carrier density (1.3×10^{10} cm^{-2}) among all the devices. Because the density of the deep traps is very low in either Cu device, the carrier injection and extraction are less affected by these deep traps than in the corresponding Au device. As a result, the Cu devices show very similar displacement current behaviors, as shown in Figure 5-2b. The proposed shallow Cu penetration and low density of deep traps at the pentacene-dielectric interface near the contact for the Cu contacts agree with the recent studies on the pentacene OFETs with Cu source and drain contacts.[55-57] Di *et al.* reported that a sharp interface was found between Cu and pentacene.[56]

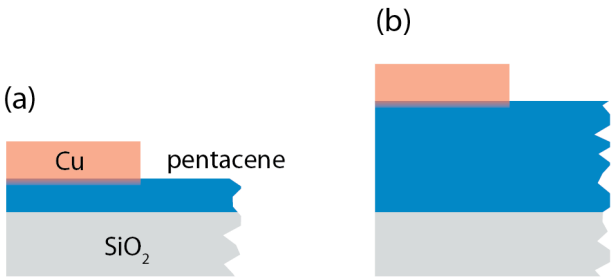

Figure 5-9 (a) and (b) Schematic diagrams illustrating the shallow penetration of Cu atoms into 30 nm and 100 nm pentacene, respectively.

5.3.2 Pentacene field-effect transistors with Au and Cu contacts

We also made pentacene OFETs with Au and Cu contacts to compare their electrical performance. The channel length of the transistors was 125 μm, and channel with was 1000 μm. The pentacene thickness was 30 nm.

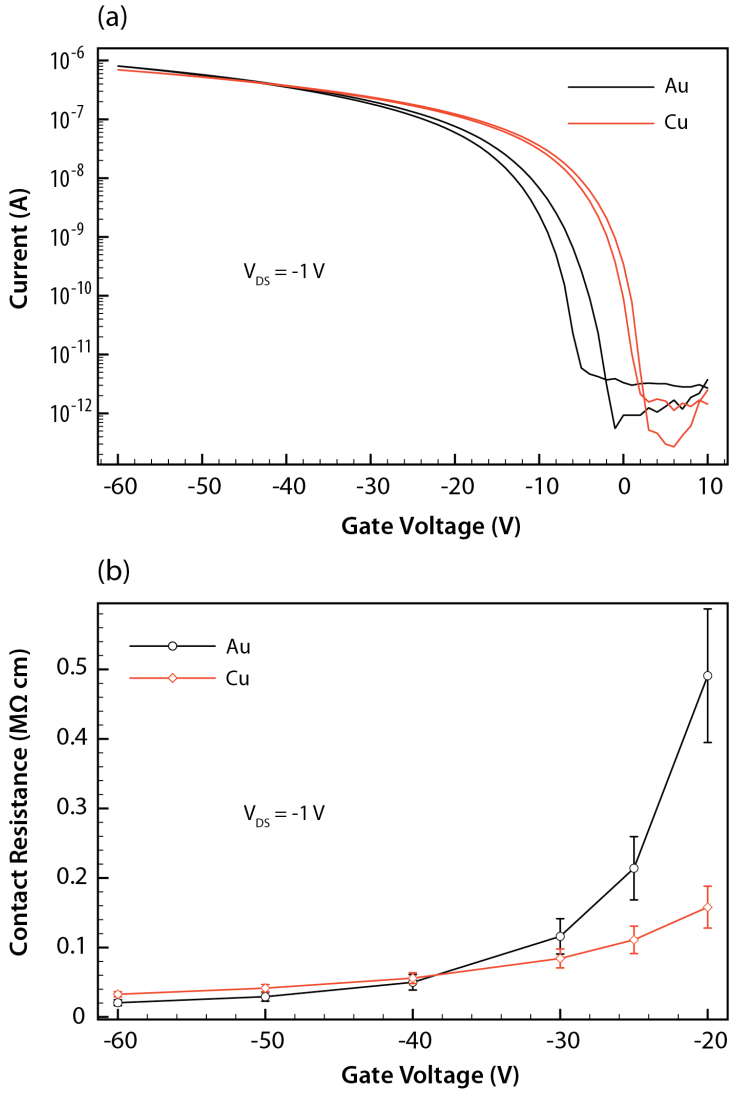

Figure 5-10 (a) Transfer characteristics of pentacene OFETs with Au and Cu contacts. (b) Contact resistance determined by transmission line method for the Au and Cu contacts. For both (a) and (b), the pentacene thickness was 30 nm, $V_{DS} = -1$ V during the measurement.

Although the injection barrier between metal and pentacene (HOMO = –5.1 eV) is higher for Cu (E_F = –4.5 eV) than for Au (E_F = –5.0 eV), the two devices exhibited very comparable electrical characteristics, as shown in Figure 5-10a. The carrier mobility at high gate voltage was 0.25 $cm^2V^{-1}s^{-1}$ and 0.18 $cm^2V^{-1}s^{-1}$ for the Au and Cu devices, respectively. The hysteresis in the transfer characteristics was less for the Cu device than for the Au device, which is consistent with the lower trapped carrier density observed for Cu LCCs shown in Figure 5-3b. We also measured the contact resistance of the Cu and Au devices by using transmission line method,[53] as shown in Figure 5-10b. At large gate bias, the contact resistance of the Au was slightly lower than that of Cu. At low gate bias, however, the contact resistance of Au was much higher than that of Cu, which is likely due to the high density of the deep trap states generated by Au peneration.[55] Collectively, these results suggest that Cu is comparable to, if not better than, Au as a contact material for pentacene OFETs, as has been reported by other groups.[55-57]

5.4 Ambipolar injection and transport in devices with Al contacts

Al is generally considered an inferior contact material for hole injection in pentacene OFETs because of the large energy barrier (~1 eV) between the Al Fermi level (–4.1 eV) and pentacene HOMO level (–5.1 eV). The electron injection barrier between the Al Fermi level and pentacene LUMO level (–3.2 eV) is ~0.9 eV, which is comparable to the hole injection barrier. As a result, electron injection from Al to pentacene should be possible and it has been reported recently.[7, 58]

Figure 5-11 shows the displacement current of a LCC with an Al contact and 30 nm pentacene fabricated on a SiO_2 substrate. The channel length was about 6 mm. The high displacement current peak from –5 to –40 V in the forward sweep suggests that the hole injection was very inefficient, possibly due to the large hole injection barrier between Al and pentacene. No displacement current associated with electron injection was observed even at very high positive gate voltages close to the breakdown voltage of SiO_2. This is possibly due to the high density of electron traps at the pentacene-SiO_2 interface.[59]

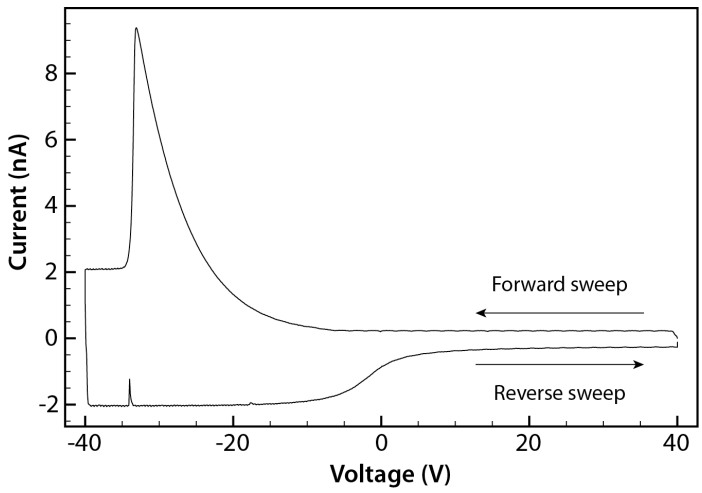

Figure 5-11 Displacement current measured from a LCC with an Al contact and 30 nm pentacene on a SiO_2 substrate.

To eliminate the electron traps, a 100 nm PMMA buffer layer was spin coated on SiO_2 (ref. 58). Figure 5-12 shows the displacement current taken from this device. A different gate voltage profile with zero starting voltage was used, as shown in the inset of Figure 5-12. Besides the hole injection peaks at the negative voltages, current peaks associated with electron injection and transport were observed at high positive voltages. It is interesting to note that electron trapping still occurred in the channel. The trapped electrons positively shifted the hole and electron injection peaks in the second sweep, and increased the height of the hole injection peak in the second sweep. The positive shift and height increase of the hole injection peak in the second sweep indicate more holes were injected to neutralize the trapped electrons. The positive shift of the electron injection peak in the second sweep indicates there were still some trapped electrons in the channel after the charge neutralization by holes.

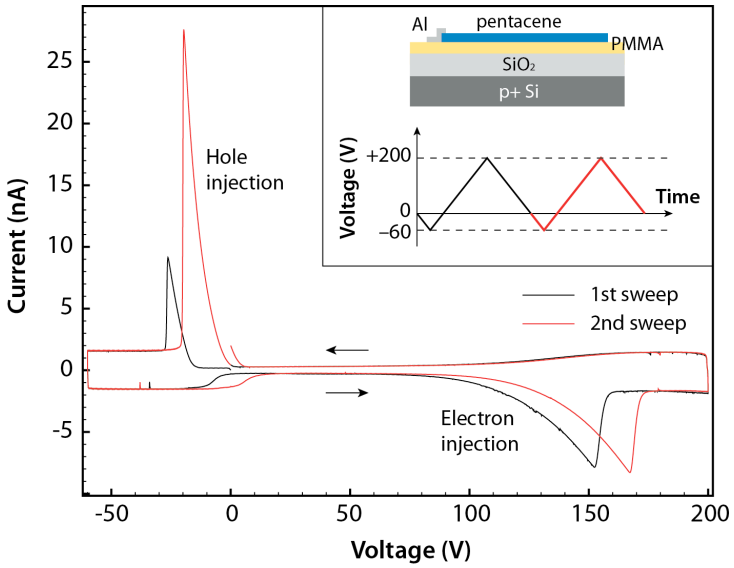

Figure 5-12 Displacement current measured from an Al LCC with a 100 nm PMMA buffer layer between pentacene (30 nm) and SiO_2. Inset: the device structure and voltage sweep profile. Black lines represent the first cyclic sweep, red lines represent the second cyclic sweep.

5.5 Conclusion

Displacement current measurement (DCM) was used to study the carrier injection and extraction in the pentacene long-channel capacitors (LCCs) with Au, Cu, and Al contacts. We found that the carrier trapping in the long channel of the Au devices was indirectly caused by the deep trap states at the pentacene-dielectric interface near the contact generated by Au penetration. More specifically, carrier trapping in the channel was more sensitive to the deep traps near the contact edge. Low trapped carrier density was found in the devices with Cu contacts presumably due to the shallow penetration of Cu atoms. Pentacene field-effect transistors with Cu contacts showed better device performance than those with Au contacts in terms of hysteresis and contact resistance at low gate voltages. In addition, ambipolar injection and transport were observed in a LCC with Al contact and a PMMA buffer layer between pentacene and SiO_2. Overall, we have shown that DCM is a useful tool for studying the carrier injection and extraction in organic field-effect transistors.

6 Examination of conducting channel depletion dynamics in organic field-effect devices via displacement current measurement

6.1 Introduction

Transient processes, including the formation and depletion of the conducting channel, are essential parts of the device operation of organic field-effect transistors (OFETs). However, these transient processes are not well understood because they are usually not detectable during steady state or quasi steady state DC measurements.[18-20, 24] It is also important to know that the transient carrier behaviors may be different from the steady state behaviors because carrier traps may not be in equilibrium during the transient processes.

Several techniques have recently been used to study the transient carrier transport during the conducting channel formation of OFETs. For example, time-resolved microscopic optical second-harmonic generation (TRM-SHG) has been used by the Iwamoto group to visualize the carrier motion during the conducting channel formation.[35-37] It is found that the position of the front of the carrier sheet follows a power law relationship with time.[36] In addition, a modified time-of-flight method was used by the Dodabalapur group and others to study the transient carrier transport.[39-41, 43] It is found that the transient mobility is typically larger than the DC field-effect mobility.[39, 43] In addition, the activation energy associated with the transient transport is higher than the activation energy associated with the steady state transport.[39, 43] Despite these achievements, very little progress has been made in understanding the transient carrier behaviors during conducting channel depletion.

Displacement current measurement (DCM)[3, 5, 6, 9] is a useful technique for characterizing both the transient carrier transport during conducting channel formation and the transient carrier extraction during conducting channel depletion.[45, 46] Here we

report the use of DCM to examine the transient carrier extraction. Instead of using common OFETs for measuring displacement current, we use long channel capacitors (LCCs)[45, 46] to limit the extraction process to one direction only, and to increase the displacement current associated with the transient carrier extraction. The transient carrier extraction during linear gate voltage sweeps and at contact gate voltages are discussed in detail.

6.2 Experiment

The schematic structure of a long-channel capacitor used in this study is shown in Figure 6-1. The substrate was a heavily doped p-type Si wafer with 300 nm SiO_2. The heavily doped Si also served as the gate electrode. Shadow masks were used to pattern both the pentacene and metal films. During the pentacene deposition, the deposition rate was 0.1–0.2 $Ås^{-1}$, and the substrate temperature was 30 °C. The thickness of the pentacene film was 30 nm. The 40 nm thick Cu contact was deposited on the pentacene by thermal evaporation at a rate of 0.5–1.0 $Ås^{-1}$. The substrate was water-cooled during the metal deposition. Cu was selected because far less deep trap states were generated in the contact region during Cu deposition, as will be discussed in Chapter 6. The channel length (L) was 3 mm, and the channel width (W) was either 3 mm or 4 mm, which was much wider than that of our pervious devices (0.5 mm). The reason for choosing a larger channel width in this study is to increase the displacement current, as well as the accuracy of the measurement. The width of the overlapping area between Cu and pentacene is typically about 0.2 mm.

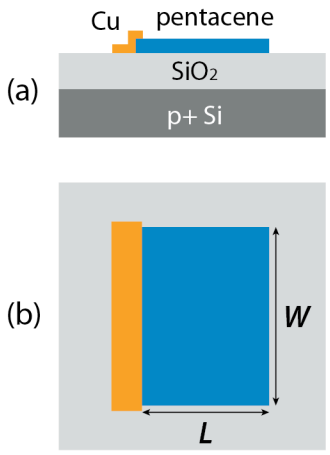

Figure 6-1 (a) Schematic cross section of a long-channel capacitor (LCC). (b) Schematic top view of the device. *L* was 3 mm, and *W* was either 3 mm or 4 mm to increase the displacement current.

All electrical measurements were performed in the dark in a vacuum probe station. A Keithley 2612 dual-channel SourceMeter was used to characterize the LCCs, with one channel applying gate voltage profiles, and the other channel measuring the displacement current running through the grounded channel contact.

Two different gate voltage profiles were used in this study. The first profile, as shown in Figure 6-2a, was a cyclic linear voltage sweep. The sweep rate was 5.7 Vs^{-1}. During the forward sweep from V_1 to V_2, charge carriers were injected into the pentacene channel; during the reverse sweep from V_2 to V_1, carriers were extracted from the pentacene channel. The second profile, as shown in Figure 6-2b, included two voltage steps. During the first step (V_3, t_1), carriers were injected into the pentacene channel. The charging time (t_1) was 15 s to ensure that carriers were distributed uniformly in the channel. During the second step (V_4, t_2), carriers were extracted from the pentacene channel, and the displacement current associated with the carrier extraction was measured as a function of time. The time interval between the data points was about 17 ms. As t_2 approaches infinity, the final steady state of the channel could be either completely or partially discharged depending on the discharging voltage (V_4).

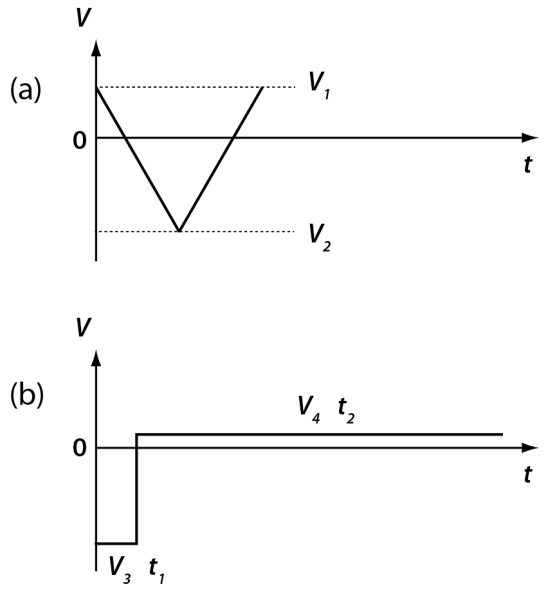

Figure 6-2 (a) Gate voltage profile containing forward (V_1 to V_2) and reverse (V_2 to V_1) voltage sweeps. (b) Gate voltage profile containing charging (V_3, t_1) and discharging (V_4, t_2) voltage steps.

6.3 Carrier extraction during linear gate voltage sweeps

6.3.1 Evolution of carrier distribution in the channel during conducting channel depletion

Figure 6-3a shows the displacement current taken under a cyclic voltage sweep. The channel length and width were 3 mm and 4 mm, respectively. The transient carrier behaviors and the shape of the displacement current curve in the forward sweep have been discussed in the previous chapters. Here we only discuss the transient carrier extraction in the reverse sweep.

As show in Figure 6-3a, the general shape of the displacement current in the reverse sweep is an S-curve. It comprises 3 different regions: the first and second flat regions at the beginning and end of the reverse sweep, respective, and a transition region between the two flat regions. The current in the second flat region is slightly higher than

the background current associated with the metal contact (dashed line in Figure 6-3a) due to the existence of carrier traps at the pentacene-dielectric interface (see Section 4.4.2.3).

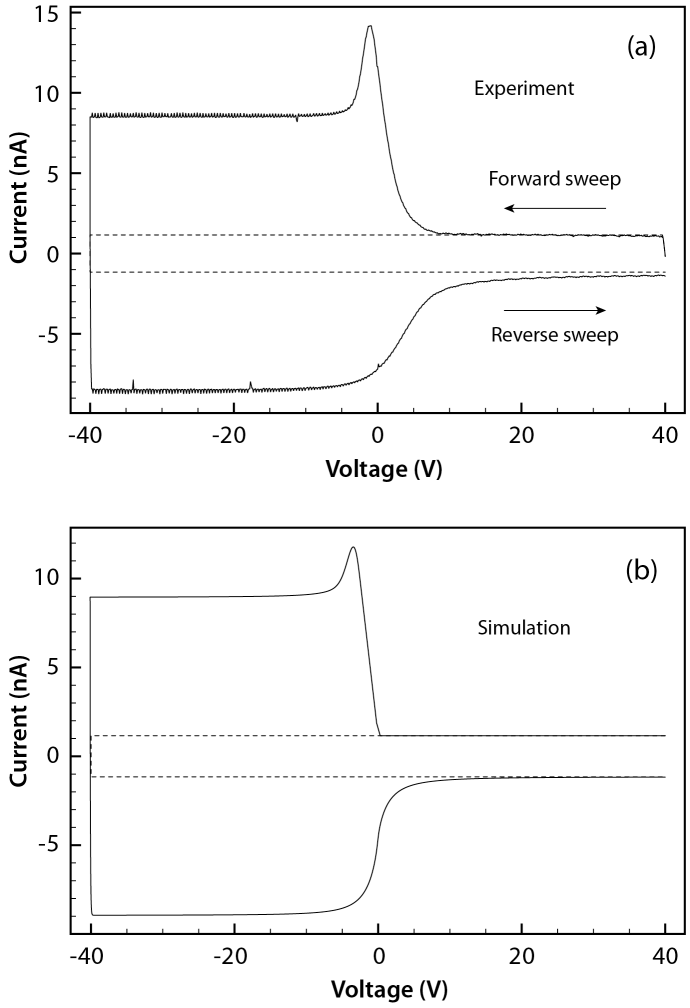

Figure 6-3 (a) Displacement current curve measured from a pentacene LCC under a cyclic gate voltage sweep. (b) Simulated displacement current curve (data courtesy of Hsiu-Chuang Chang). In the simulation, μ = 0.1 $cm^2V^{-1}s^{-1}$, hole injection starts at 0 V, and no traps are considered. Dashed lines in both figures: background current associated with the metal contact.

To understand the carrier distribution in the channel in the reverse sweep, the previous numerical model is used. The carrier mobility (μ) used in the simulation is 0.1 $cm^2V^{-1}s^{-1}$. At V_G = 0 V, holes are injected from the contact to pentacene. (In the

experiment, the injection started at a positive voltage, presumably because the pentacene was slightly p-doped by impurities.) No carrier traps are considered in the numerical model. As shown in Figure 6-3b, the general shape of the simulated curve in the reverse sweep is very similar to that of the experimental curve in Figure 6-3a.

The carrier distribution in the first flat region is easy to understand. The constant displacement current indicates the pentacene film is very conductive. The carrier distribution in the channel is uniform, and the carrier density changes linearly with time. In the transition region, however, the carrier distribution in the channel is no longer uniform. In Figure 6-4a, the transition region of the simulated displacement current curve is plotted against gate voltage and time, with $t = 0$ at $V_G = 0$. Several points are selected in the transition region, and the carrier distributions at these points are shown in Figures 6-4b and 6-4c. The 0% position corresponds to the contact end of the channel, and the 100% position corresponds to the other end of the channel.

Figure 6-4b shows the carrier distributions from –2 s to 2 s with a time interval of 1 s. At $t = -2$ s, the carrier distribution in the channel is close to uniform. Two types of carrier extraction behaviors are clearly seen in the figure.

For $t < 0$, the carrier density in the channel is high, and carriers are extracted at high speeds. From –2s to 0 s, the carrier density at the contact end is controlled by the gate voltage and hence it changes linearly with time. However, the change rate of the carrier density at the other end of the channel cannot follow that at the contact end. As a result, the difference between the carrier densities at the both ends increases with time.

For $t \geq 0$, the carrier density at the contact end is zero. As a result, *the gate voltage sweep has no more effect on the carrier extraction*. In other words, the carriers are getting out of the channel by drift and diffusion without the help of the gate voltage. As a result, the carriers are extracted from the channel at much smaller speeds compared to the case for $t < 0$.

Figure 6-4c shows the carrier distribution from –1 s to +1 s with a time interval of 0.2 s, providing more details about the different extraction behaviors for $t < 0$ and $t \geq 0$.

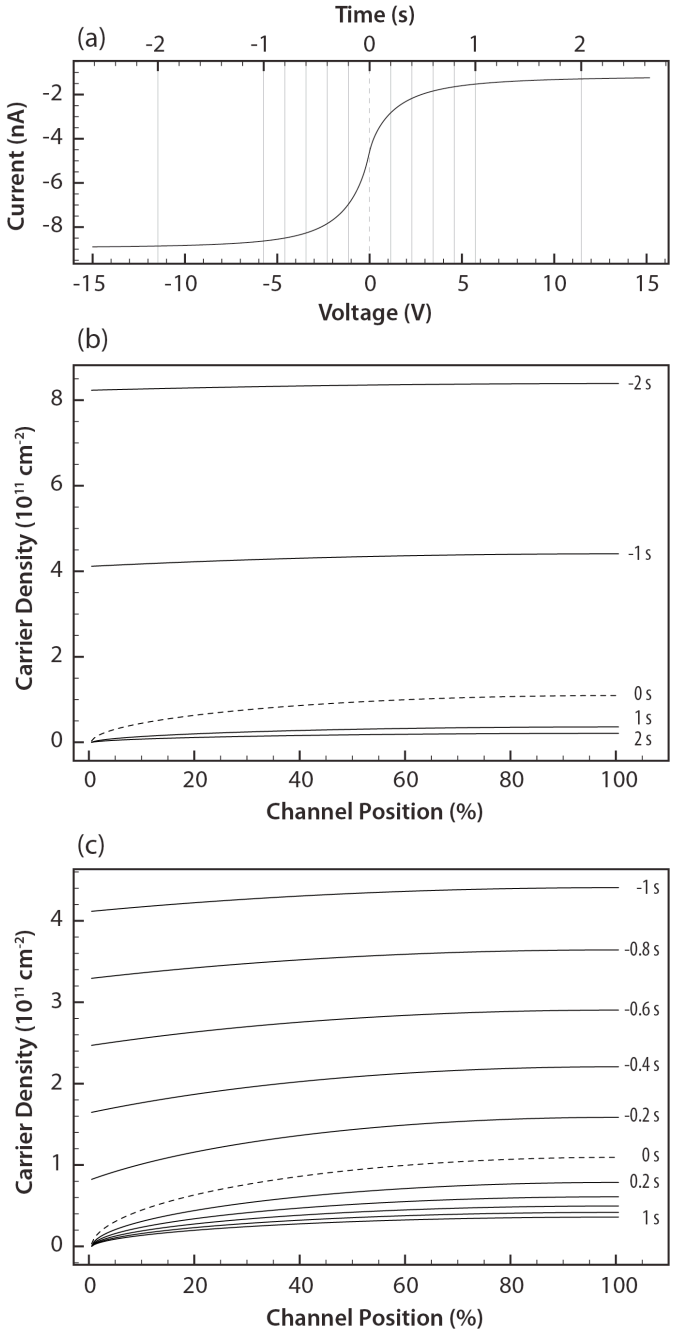

Figure 6-4 (a) The transition region in simulated displacement current curve plotted against voltage (bottom *x*-axis) and time (top *x*-axis). (b) Carrier distributions in the channel from –2 s to 2 s with a time interval of 1 s. (c) Carrier distributions in the channel from –1 s to 1 s with a time interval of 0.2 s. The carrier distribution at $t = 0$ is highlighted by dashed lines in (b) and (c). (Data courtesy of Hsiu-Chuang Chang.)

6.3.2 Carrier extraction at different temperatures

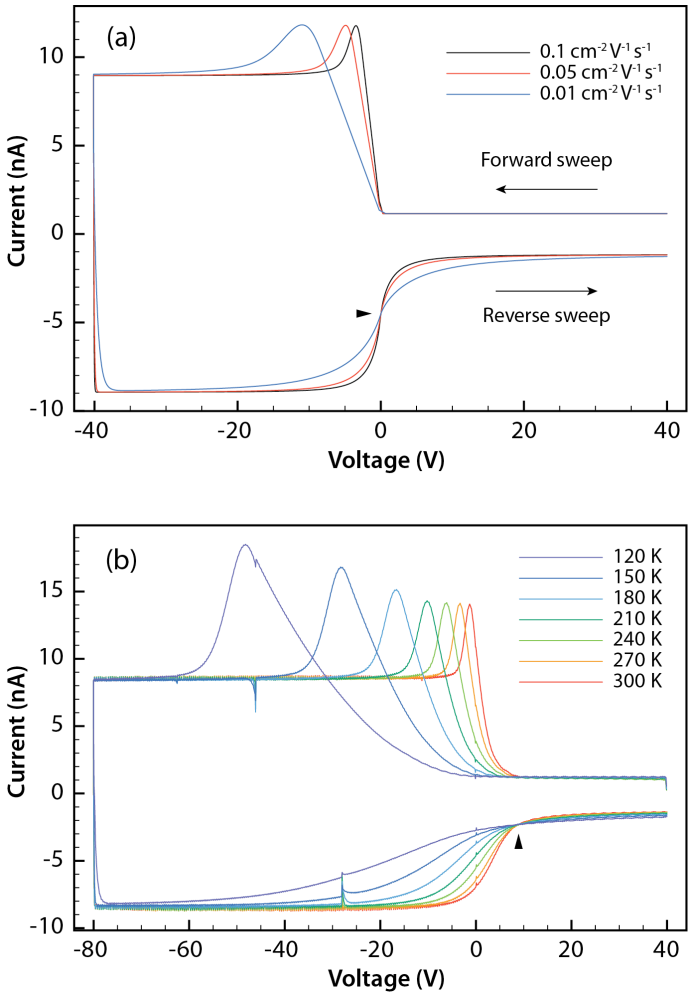

Figure 6-5 (a) Simulated displacement current curves with different motilities (data courtesy of Hsiu-Chuang Chang). (b) Displacement current curves measured from a pentacene LCC at different temperatures. The single crossing point of the displacement current curves is highlighted by a black triangle in each figure.

When the carrier mobility is decreased in the simulation, the width of the transition region increases, as shown in Figure 6-5a. In addition, all the displacement current curves with the different mobilities cross at a single point at $V_G = 0$ when the

carrier density at the contact end is zero. This point is also the center of the transition regions of all the displacement current curves.

As shown in Figure 6-5b, similar increase of the transition region width was also observed in the experiment as the temperature decreased due to the decrease of carrier mobility. However, the center of the transition region was negatively shifted as the temperature decreased. We believe this shift is due to the carrier traps.

Because of the above changes in the transition region, fewer carriers were able to get out of the channel during the reverse sweep as the temperature decreases. Hence more carriers were trapped in the pentacene channel at the end of the sweep, as shown in Figure 6-6c. We believe the "trapped" carriers in Figure 6-6c include both the carriers that were actually in the trap states and those that could not get out of the channel at end of the reverse sweep because of the low extraction rate.

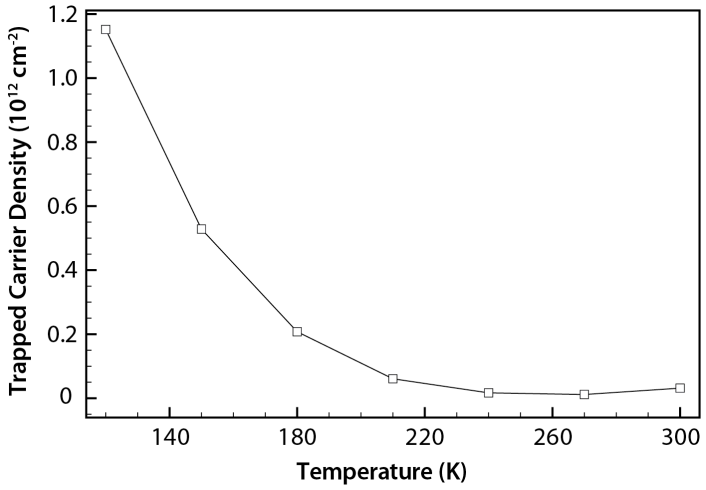

Figure 6-6 Plot of trapped carrier density at the end of the reverse sweep *vs.* temperature.

In is interesting to note that the experimental displacement current curves in the reverse sweep still cross at a single point as highlighted by the arrow in Figure 6-5b. However, this point is not at the center of the transition region at any given temperature. The crossing point is very close to the onset voltage of hole injection at 300 K, which

means that at this point the carrier density at the contact end is likely to be zero, just as the case for the simulation results.

6.4 Carrier extraction at constant gate voltages

Another way to study the transient carrier extraction is to use the step voltage profile as shown in Figure 6-2b. The initial carrier density in the channel is dependent on the charging voltage V_3. The final steady state carrier density in the channel (as t_2 approaches infinity) is dependent on V_4. If the final carrier density is not zero, we call it the *partially discharged* case. If the final carrier density is zero, we call it the *completely discharged* case. The completely discharged case is more relevant to the real device operation of OFETs: the states of the LCC during the first and second voltage steps correspond to the ON and OFF states an OFET, respectively.

The charging time t_1 was typically 15 s to ensure that carrier distribution in the channel was stabilized and uniform. We found that no change occurred in the extraction process when t_1 was longer than 15 s. We also found that the extraction process was not sensitive to the charging voltage V_3. At room temperature, for example, when V_3 was changed from –20 V to –80 V, it only changed the magnitude of the displacement current at the very beginning of the extraction process and had little effect on the overall behavior of the extraction process. The discharging voltage V_4, however, had a major effect on the extraction process.

6.4.1 Effect of discharging voltage on transient carrier extraction

Figures 6(a) and 6(b) show the displacement current measured at different discharging voltages V_4 in semi-log and log-log plots, respectively. The channel length and width of the device are both 3 mm. The charging gate voltage V_3 was –40 V for all the measurements. The inset of Figure 6-7a shows the displacement current measured from the same device under a cyclic linear voltage sweep. The onset voltage of carrier injection in the forward sweep was about 5 V. The color-coded vertical lines in the inset of Figure 6-7a show the positions of V_4 on the displacement current curve.

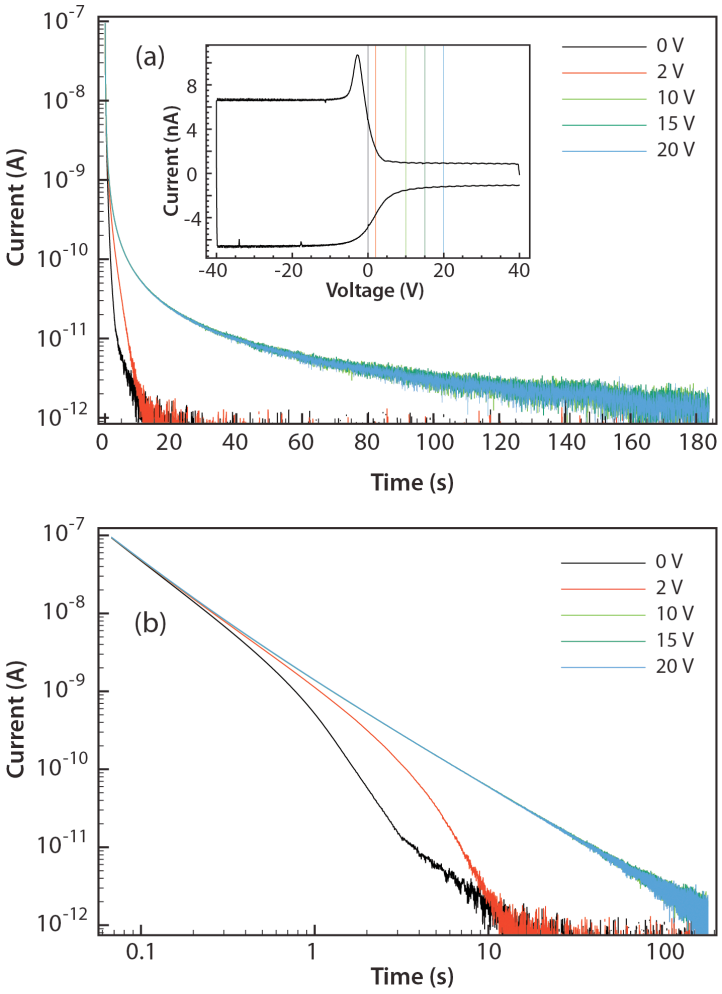

Figure 6-7 (a) Semi-log plot of displacement current *vs.* time at different the discharging voltage V_4. The displacement current curves for V_4 = 10, 15, and 20 V overlap each other. Inset: displacement current measured from the same device under a cyclic voltage sweep. The color-coded lines visualize the positions of V_4 on the displacement current curve. (b) Log-log plot of the displacement current *vs.* time as in (a).

For the completely discharged case (*e.g.* V_4 = 10, 15, or 20 V), the displacement current behavior was *independent* of V_4 and it followed a power law decay (Figure 6-7b). The exponent of the power law decay was about 1.3. For the partially discharged case (*e.g.* V_4 = 0, or 2 V), the displacement current was dependent on V_4 and it exhibited an

exponential decay (Figure 6-7a). The exponential decay was much faster than the power law decay.

To understand the dependence of the transient carrier extraction on the discharging voltage, a simple resistance-capacitance (RC) model is proposed here, with its circuit diagram shown in Figure 6-8. This model is developed by Hsiu-Chuang Chang and Prof. P. Paul Ruden.

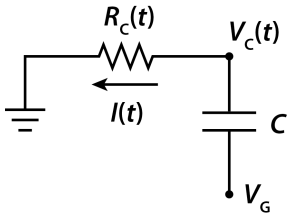

Figure 6-8 Circuit diagram of the proposed RC model developed Mr. Chang and Prof. Ruden.

During the extraction process, it is assumed that the channel capacitance C is a constant and the carrier distribution in the channel is uniform. In addition, the channel resistance $R_C(t)$ is assumed to be inversely proportional to the carrier density $p(t)$ in the channel by the following equation:

$$R(t) = \frac{L}{We\mu p(t)} = \frac{L^2}{\mu C\left(V_C(t) - V_G\right)} \qquad (6\text{-}1)$$

where L and W is the channel length and width, respectively, e is the elementary charge, μ is the carrier mobility, and $V_C(t)$ is the channel voltage.

Assume the charging occurs during $t \leq 0$, *i.e.* $V_G\ (t \leq 0) = V_3$, and $V_C\ (t \leq 0) = 0$. For $t > 0$, V_G switches from V_3 to V_4, *i.e.* $V_G\ (t > 0) = V_4$.

The time-dependent discharging current $I(t)$ is

$$I(t) = \frac{V_C(t)}{R_C(t)} = -C\frac{dV_C(t)}{dt} \qquad (6\text{-}2)$$

Inset Equation 6-1 into Equation 6-2, and substitute V_G with V_4 we get

$$\frac{dV_C(t)}{dt} = \frac{\mu}{L^2}\left(V_4 V_C - V_C{}^2\right) \qquad (6\text{-}3)$$

The final carrier density in the channel is dependent on V_4. For the sake of simplicity, we assume that the onset voltage for hole injection is 0 V. Also, no electron injection is considered. If $V_4 < 0$, the final carrier density in the channel is $C|V_4|/(LW)$, corresponding to the partially discharged case. If $V_4 \geq 0$, final carrier density in the channel is 0, corresponding to the completely discharged case. By solving Equation 6-3, we can get the equations for the discharging current.

For the partially discharged case (*i.e.* $V_4 < 0$), $I(t)$ is dependent on V_4 and it follows a exponential decay:

$$I(t) = \frac{\mu C V_4}{L^2} \frac{(1/V_4 - 1/V_3)}{[(1/V_4 - 1/V_3)\exp(\mu V_4 t/L^2) + 1/V_4]^2} \exp(\frac{\mu V_4}{L^2} t) \qquad (6\text{-}4)$$

For the completely discharged case (*i.e.* $V_4 \geq 0$), $I(t)$ is independent of V_4 and it follows a power law decay:

$$I(t) = \frac{CL^2}{\mu} \frac{1}{[t - (L^2/\mu V_3)]^2} \qquad (6\text{-}5)$$

Figure 6-9 summarizes the results of the RC model. The exponential behavior for the partially discharged case and the power law behavior for the completely discharged case are clearly seen in Figures 6-9a and 6-9b, respectively. To understand the results obtained from the RC model, it is helpful to first consider a conventional RC model in which the resistance is a constant. The discharging current of the conventional model follows an exponential decay. For the partially discharged case in our model, the resistance increases at the beginning but it eventually becomes a finite constant value. As

a result, the overall discharge current still follows an exponential decay. For the completely discharged case, however, the final resistance approaches infinity when the carrier density in the channel approaches zero. So the carrier extraction becomes more and more difficult with time. The slower power lay decay is a result of the inverse proportional relationship between the resistance and carrier density.

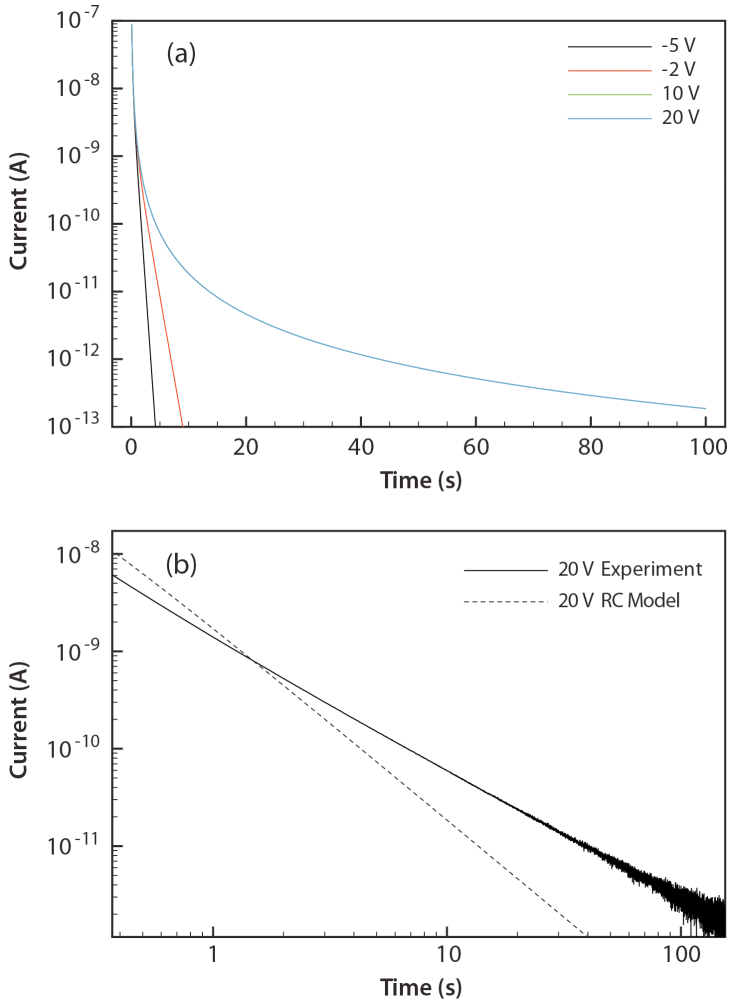

Figure 6-9 Semi-log plots of displacement current *vs.* time at different discharging voltages (V_4) obtained from the RC model (data courtesy of Hsiu-Chuang Chang). The displacement current curves for V_4 = 10 V and 20 V overlap each other. (b) Log-log plot of the displacement current *vs.* time at V_4 = 20 V. Dashed line: results from the RC model with an exponent of 2. Solid line: experimental data with a power law decay exponent of 1.3.

For the completely discharged case, the experimental data is also plotted in Figure 6-9b for comparison. The power law decay exponent obtained from the RC model is 2, while the exponent for the experimental data was 1.3. Preliminary results obtained from a more sophisticated RC model considering carrier traps suggest that the decrease of the exponent is due to the existence of carrier traps in the channel.[64] Qualitatively speaking, the existence of carrier traps further decreases the free carriers density in the channel, resulting in a higher the channel resistance compared to the situation with no carrier traps.

6.4.2 The completely discharged case: effect of temperature

To get more information on the transient carrier behaviors for the completely discharged case, variable temperature measurements were conducted on a pentacene LCC ($L = W = 3$ mm). Figure 6-10 shows the displacement current *vs.* time at different temperatures. For all the measurements, the charging voltage V_3 was –80 V, and the discharging voltage V_4 was +40 V.

Obviously, the displacement current still followed the power law decay at the different temperatures. In addition, the power law decay exponent (ranging from –1.25 to –1.28) was independent of the temperature. Currently, we are unable to explain these phenomena with the RC model. We hope the numerical model currently under development may provide more information regarding the transient carrier behaviors at different temperatures.

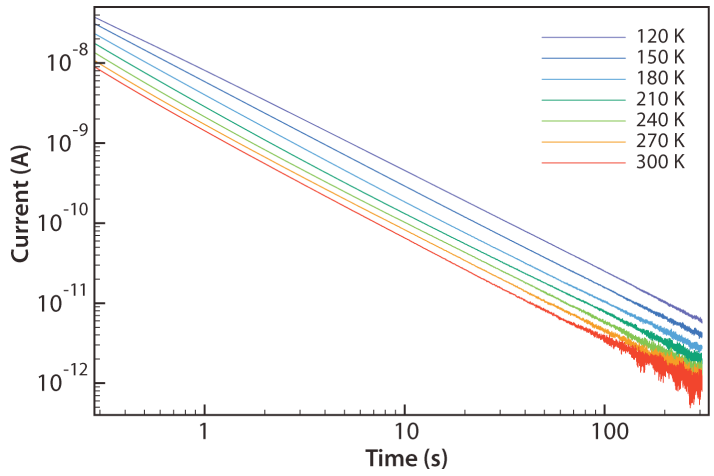

Figure 6-10 Discharging displacement current measured from a pentacene LCC at different temperatures. The charging voltage was –80V and the discharging gate voltage was +40V. The channel width and length were both 3 mm.

Another feature in Figure 6-10 is that the displacement current increased as the temperature decreased. Because the current followed power law decay, the discharging process took longer to complete at the lower temperature. This phenomenon can be explained with Equation 6-5. According to this equation, as temperature decreases, the carrier mobility also decreases, resulting in the increase of the displacement current. We can fit the experimental data in Figure 6-10 with a simple equation

$$I = \frac{a}{(t+b)^c} \qquad (6\text{-}6)$$

where a, b, and c are fitting parameters. Based on Equation 6-6, $1/a$ should be proportional to the carrier mobility, and hence it should be thermally activated. Figure 6-11 shows the Arrhenius plot of $1/a$. A good linear behavior is seen and the activation energy obtained from this plot is about 40 meV. The activation energy can also be obtained from the variable-temperature mobilities calculated from the slopes of displacement current peaks with Equation 4-12. With this method, the activation energy

obtained from Figure 6-5b is about 60 meV. The two activation energies show reasonable agreement.

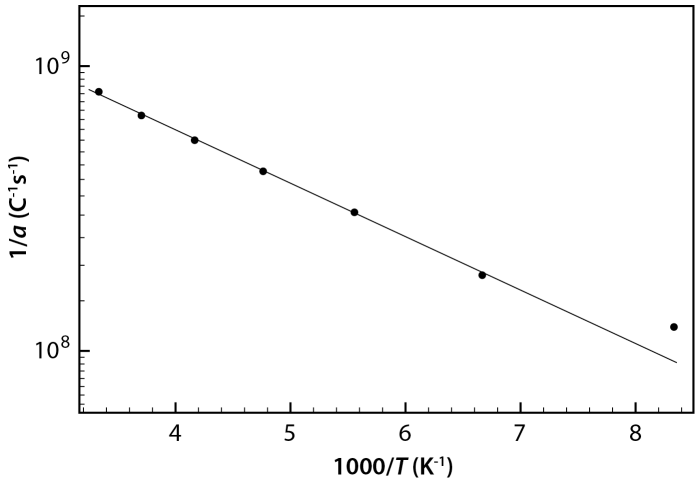

Figure 6-11 Arrhenius plot of 1/*a*. *a* is a fitting parameter in Equation 6-6.

6.5 Conclusion

We have conducted detailed experimental and theoretical studies on the transient carrier extraction during the conducting channel depletion in long channel capacitors (LCCs). Two different exaction situations are considered: the carrier extraction under linear gate voltage sweeps, and the carrier extraction under constant gate voltages.

For the carrier extraction under linear voltage sweeps, we are able to calculate with a numerical model the evolution of the carrier distribution in the channel during the conducting channel depletion. It is found that before the carrier density at the contact end of the channel becomes zero, the carriers are extracted at fast rates driven by the voltage sweep. After the carrier density at the contact end becomes zero, the voltage sweep has no more effect on the carrier extraction, so that the carriers are extracted at much slower rates. We have also conducted variable temperature displacement current measurement under linear voltage sweeps. As the temperature decreases, more carriers are trapped in the channel at the end of the sweep due to the decrease of the extraction rate.

For the carrier extraction at constant gate voltages, we have found that the transient extraction behavior is greatly dependent on the discharging voltage that controls the final steady state carrier density in the channel. If the steady state carrier density is not zero, which corresponds to the partially discharged case, the discharging displacement current follows an exponential decay. If the final carrier density is zero, which corresponds to the completely discharged case, the discharging displacement current follows a power law decay. A simple RC model has been proposed assuming that the channel resistance is inversely proportional to the carrier concentration in the channel. The discharging-voltage-dependent exponential and power law decays can be successfully explained with this simple model. In addition, we have conducted variable temperature measurements for the completely discharged case. It is found that the discharging displacement current increases as the temperature decreases. However, the displacement current still follows the power law decay with the exponent independent of the temperature. With regard to organic field-effect transistors (OFETs), we believe the power law decay of the transient discharging current should also occur in an OFET when switched from ON to OFF state.

7 Future work

7.1 Transient carrier behaviors

7.1.1 Variable temperature displacement current measurement

Figure 7-1a shows the typical results obtained from variable temperature displacement current measurement with cyclic gate voltage sweeps. The carrier mobilities at the different temperatures can be calculated from the slopes of the displacement current with Equation 4-12 (Section 4.4.1). Figure 7-1b shows the Arrhenius plot of the carrier mobility obtained from Figure 7-1a. The activation energy of the carrier mobility is about 60 meV. Because this activation energy is associated with the transient transport in the long channel, it might be different from the activation energy associated with the steady state transport. In future study, it is interesting to make systematic comparison between the activation energy determined by displacement current measurement of a pentacene LCC and the activation energy determined by DC measurements of a pentacene transistor on the same substrate made in the same run. Dunn and Dodabalapur have systematically conducted similar study with modified time of flight method.[43] They have found the activation energy associated with the transient transport is larger than the activation energy associated with the steady state transport. Their explanation for this difference is based on the difference of the carrier concentrations during the transient and steady state transports.

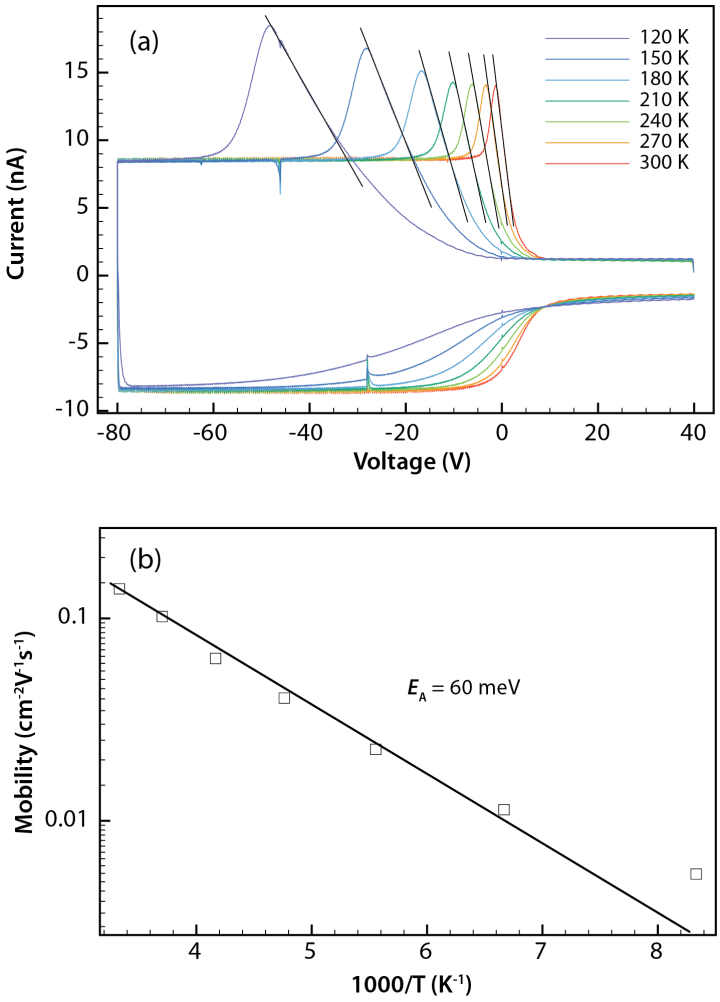

Figure 7-1 (a) Results obtained from variable temperature displacement current measurement with cyclic gate voltage sweeps. The device under test was a pentacene LCC with Cu contact and SiO_2 dielectric. The channel length and width were 3 mm and 4 mm, respectively. (b) Arrhenius plot of the carrier mobility calculated from the slope of the displacement current peak.

Another way of conducting variable temperature displacement current measurement is introduced in Chapter 5. At a given temperature, the channel is first charged at a constant gate voltage, and then the channel is discharged at a constant discharging gate voltage that allows all the carriers in the channel to get out eventually. The displacement current is measured during the discharging process. Figure 7-2 shows the results of this measurement at different temperatures on a log-log plot. The striking

feature is that the exponent of the power law decay (typically between 1.2 to 1.3) is independent of temperature. However, right now we are unable to explain this phenomenon. We believe solving this puzzle would help us to get a deeper understanding about the carrier traps.

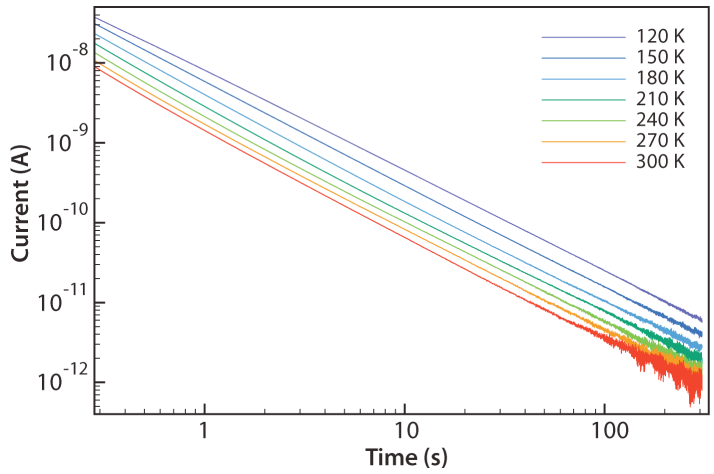

Figure 7-2 Discharging displacement current measured at different temperatures. The device under test was a pentacene LCC with Cu contact and SiO_2 dielectric. The channel length and width were both 3 mm. The charging voltage was –80 V, and the charging time was 15 s. The discharging voltage was +40 V.

A similar experiment can be done by using a new gate voltage profile with a linear voltage sweep added between the changing and discharging voltage steps, as shown in the inset of Figure 7-3a. The displacement current is measured during the voltage sweep and the discharging voltage step, as shown in Figure 7-3a. We find that the displacement current during the discharging voltage step still follows power law decay. The exponent of the power lay decay is typically between 1.2 to 1.3, and it is independent of temperature, as shown in Figure 7-3b. These behaviors are very similar to those seen in Figure 7-2. The reason for using the new voltage profile is that the displacement current under this situation can be simulated with a numerical model. The simulation studies will give us more information about the discharging process, which would help us

answer the questions what determines the value of the exponent and why the exponent is temperature independent.

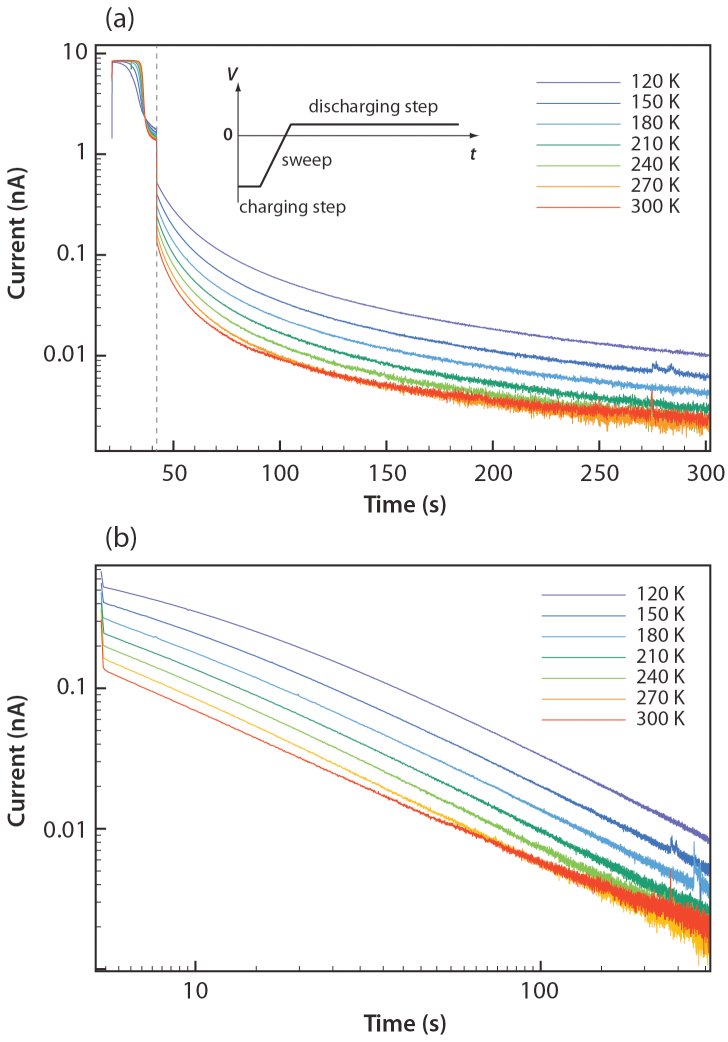

Figure 7-3 (a) Discharging displacement current measured with a new gate voltage profile (inset) at different temperatures. The current before the dashed line was measured during the sweep, and the current after the dashed line was measured during the discharging voltage step. (b) Log-log plot of the displacement current *vs.* time during the discharging step. The device under test was a pentacene LCC with Cu contact and SiO_2 dielectric. The channel length and width were 3 mm and 4 mm, respectively. The charging voltage was –80 V, the discharging voltage was +40 V, and the sweep rate of the voltage sweep between the two steps was 5.7 Vs^{-1}.

7.1.2 Effects of gate dielectrics

We believe the temperature-dependent displacement current behaviors are primarily due to the carrier traps at the pentacene-dielectric interface. It is would be helpful to change the dielectric material and study its effects on the displacement current behaviors. Some preliminary results from pentacene LCCs with a polystyrene (PS) dielectric (spin coated on the SiO_2 substrate) are given here.

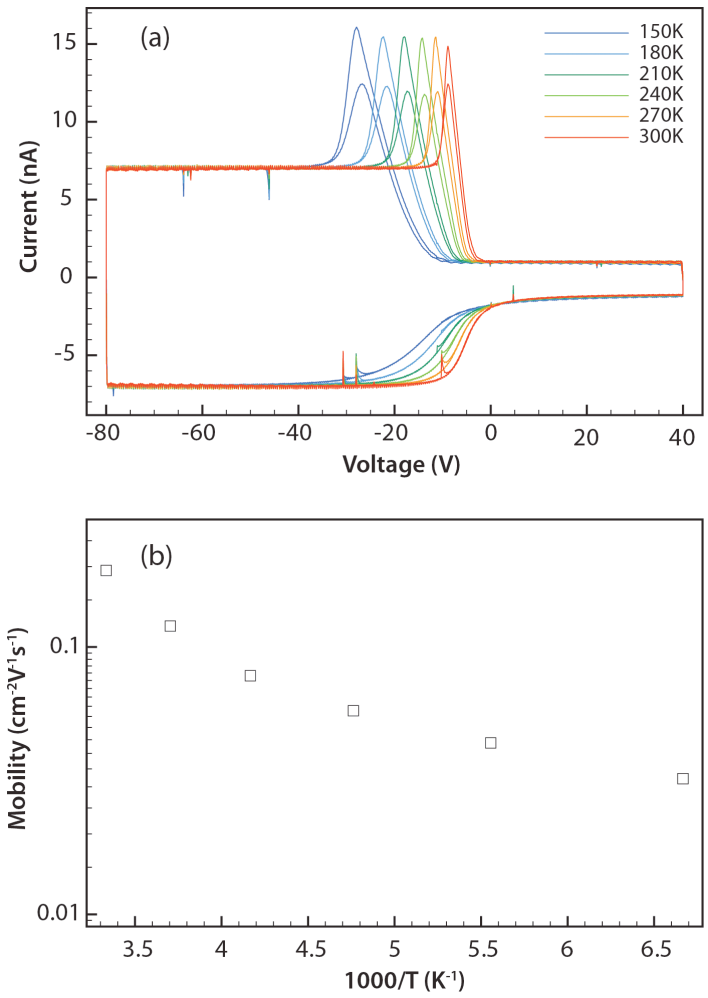

Figure 7-4 (a) Results obtained from variable temperature displacement current measurement with cyclic gate voltage sweeps. The device under test was a pentacene LCC with Cu contact and PS/SiO_2 dielectric. The channel length and width were 3 mm and 4 mm, respectively. (b) Arrhenius plot of carrier mobility calculated from the slope of the displacement current peak.

Figure 7-4a shows the results obtained from the variable temperature measurements with cyclic voltage sweeps. At 300 K, a clear shift is seen between the onsets of the displacement current peaks in consecutive cyclic sweeps. However, no shift was seen for the pentacene LCC with the SiO_2 dielectric and the same Cu contact. The shift is probably due to the thermal damage of the pentacene film near the contact during the Cu deposition. The damage is more severe on the PS dielectric because of its low thermal conductivity. Figure 7-4b shows the Arrhenius plot of the mobility calculated from the slope of the displacement current peak. No good linear behavior is seen, probably due to the contact effect mentioned above.

Figure 7-5a shows the discharging displacement current at different temperatures. Like the case in Figure 7-2, the slope shows very weak dependence on the temperature. The power law decay behavior of the device with the PS dielectric is very close to that of the device with the SiO_2 dielectric, as shown in Figure 7-5b. The power law decay exponent is 1.28 for SiO_2, and 1.20 for polystyrene. Based on these preliminary results, we think the hole traps in the both devices are not directly related to the dielectrics. They are more likely to be related to the defects in the polycrystalline pentacene films, such as grain boundaries, dislocations, and point defects.

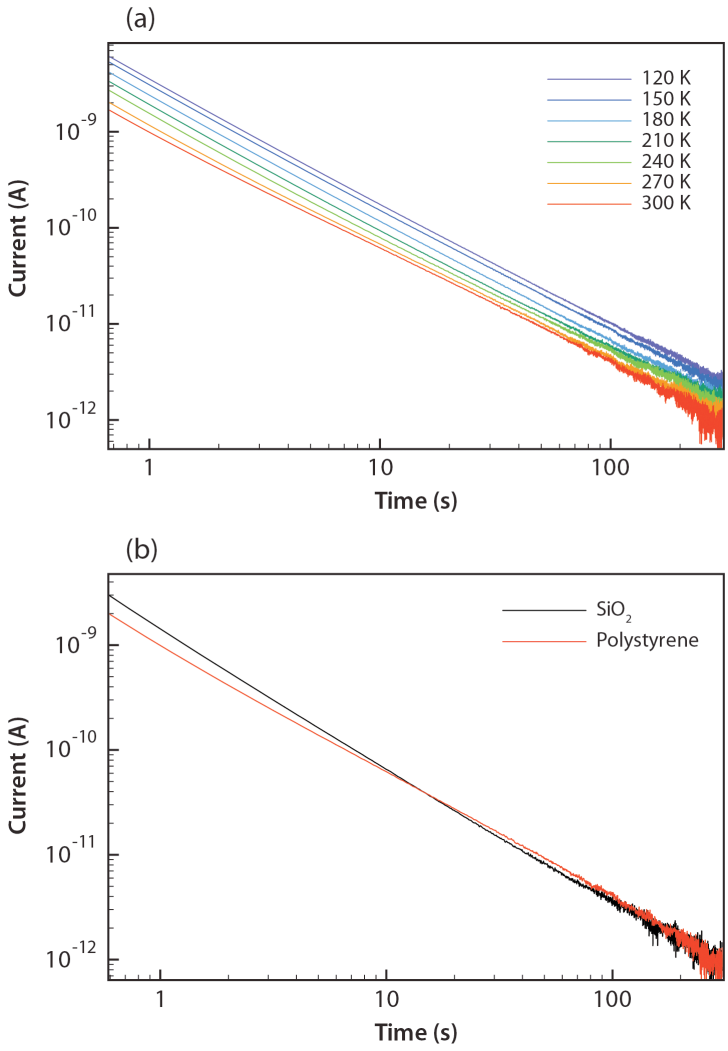

Figure 7-5 (a) Discharging displacement current measured at different temperatures. The device under test was a pentacene LCC with Cu contact and PS/SiO_2 dielectric. The channel length and width were both 3 mm. The charging voltage was –80 V, and the charging time was 15 s. The discharging voltage was +40 V. (b) Comparison of the room temperature results obtained from pentacene LCCs with SiO_2 and polystyrene dielectrics. The power law decay exponent is 1.28 for SiO_2, and 1.20 for polystyrene.

7.2 Contact effects

7.2.1 Hole injection in pentacene LCCs with Al contacts

Figure 7-6 shows the displacement current taken from two pentacene LCCs with Al contacts. The pentacene thickness was 30 nm in one device, and 100 nm in the other device. For the both devices, the channel length and width were 6 mm and 0.5 mm, respectively. For the Al device with 30 nm pentacene, very high displacement current peaks were observed, and the second peak shifted *positively* in contrast to the negative shift for the Au devices (Figure 6-2). Furthermore, the shape of the current peak changed dramatically if the positive end of the cyclic sweep was increased to +100 V, as shown by the red dashed line in Figure 7-6.

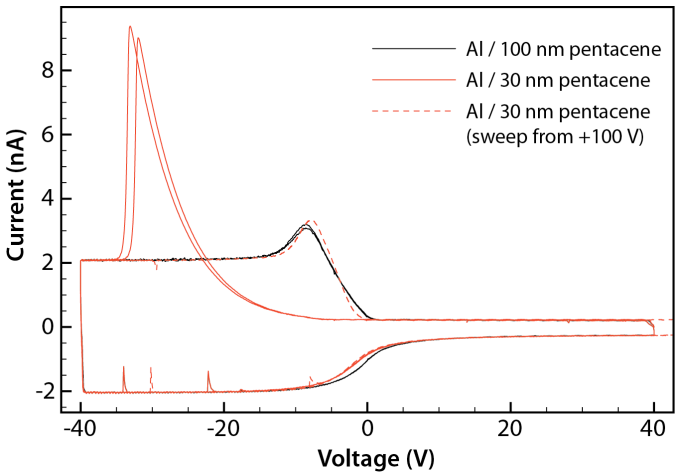

Figure 7-6 Displacement current measured from Al LCCs with 30 nm (black solid lines) and 100 nm (red solid lines) pentacene. Each measurement consisted of two consecutive cyclic sweeps. An additional measurement was performed on the device with 30 nm pentacene, in which the starting voltage of the cyclic sweep was +100 V (red dashed lines).

For the Al device with 100 nm pentacene, the displacement current in the forward sweep was very different from that of the Al device with 30 nm pentacene. However, it was similar to the displacement current in the forward sweep for the Al device with 30

nm pentacene when the sweep was started from +100 V. In the reverse sweep, both Al devices showed similar behavior.

Here we give one possible explanation for the different hole injection behaviors observed in Figure 7-6, which is based on deep Al penetration. According to the numerical simulation, a model based on carrier traps in a narrow region near the contact generated by Al penetration can also explain the high displacement current peaks in Figure 7-6. More work is needed to clarify which mechanism occurs in the real devices.

Al is generally considered an inferior contact material for hole injection in pentacene OFETs, because a large energy barrier (~1 eV) exists between the Al Fermi level (–4.1 eV) and pentacene HOMO level (–5.1 eV). This large energy barrier might result in the limited charge injection and hence the large displacement current peaks observed for the Al device with 30 nm pentacene. However, it seemed that the energy barrier had much less effect on the charge injection for the device with 100 nm pentacene.

It was reported that Al can penetrate deep into 3,4,9,10-perylenetetracarboxylic dianhydride (PTCDA) films even though aluminum oxide was formed during Al deposition.[65] The large heat released upon the formation of aluminum oxide (ΔH_f = -1670 kJ/mol for Al_2O_3) might facilitate the penetration. As a result, the different injection behaviors were possibly related to the depth of Al penetration relative to the pentacene film thickness. For the device with 100 nm pentacene, the penetration depth might be less than the pentacene film thickness. So the charge carriers were first *vertically* injected from Al to the pentacene molecules contacting it, then transported to pentacene molecules at the pentacene-dielectric interface, and finally horizontally transported into the channel, as shown in Figure 7-7a. For the device with 30 nm pentacene, the Al might penetrate the whole pentacene film. As a result, carriers were *horizontally* injected from Al contact to the pentacene molecules at the pentacene-dielectric interface, as shown in Figure 7-7b.

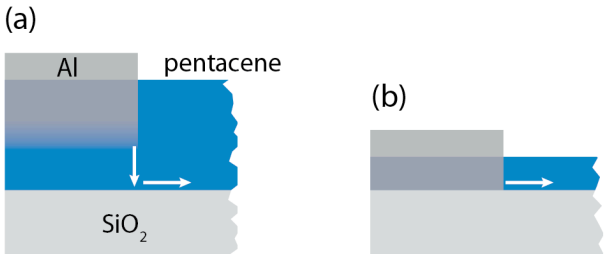

Figure 7-7 Proposed charge injection model in Al devices with (a) 100 nm pentacene and (b) 30 nm pentacene. The deep penetration of Al changed the injection behavior from vertical in the device with 100 nm pentacene to horizontal in the device with 30 nm pentacene.

It is not certain why the energy barrier had less effect on the injection process in the device with 100 nm pentacene. But it is highly possible that the *vertical* electric field at the Al/pentacene interface might enhance the tunneling injection and hence suppress the effect of the injection barrier. The vertical electric field, however, would not affect the injection process in the device with 30 nm pentacene because, as explained above, the injection direction might be *horizontal*. In this case, the energy barrier effectively limited the injection process, resulting in the large current peaks from 0 V to -30 V in Figure 7-6. Interestingly, the charge extraction characteristics in the reverse sweeps were very similar for the both Al devices, indicating the energy barrier did not affect the extraction process.[53]

By starting the cyclic sweep at +100 V, the injection behavior for the device with 30 nm pentacene changed dramatically, and became very similar to that for the device with 100 nm pentacene. This indicates that the energy barrier was somehow decreased. We propose that at high positive gate voltage, electrons were injected from Al to pentacene molecules. Because electron transport was not allowed on the pentacene-SiO_2 interface due to electron traps,[59] the injected electrons were accumulated at the pentacene-dielectric interface near the Al contact, forming an interfacial dipole that lower the energy barrier, as shown in Figures 7-8a and 7-8b. When the starting gate voltage of the cyclic sweep was +40 V, not enough electrons were injected to change the injection

behavior, but a small amount of them might caused the small positive peak shift in the second consecutive sweep, as observed in the red solid lines in Figure 7-6.

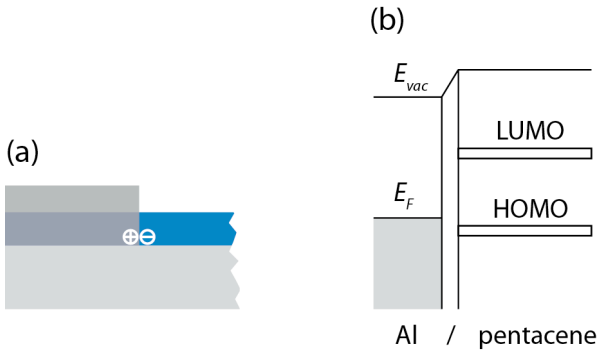

Figure 7-8 (a) Interfacial dipole is generated when electrons are injected and trapped on pentacene-SiO_2 interface near the contact. (b) Energy band diagram at the interface between Al and pentacene when the interfacial dipole is present.

7.2.2 Bottom contact devices

Till now, we have only discussed the carrier injection and extraction in LCCs with a top-contact (TC) configuration. Here we show some preliminary results on displacement current measured from LCCs with a bottom-contact (BC) configuration. Figure 7-9 shows the displacement current taken from TC and BC pentacene LCCs with Au contacts. Both devices were made on the same substrate with a channel length of 6 mm, and a channel width of 0.5 mm. The Au contact of the BC device was first deposited on SiO_2. Pentacene strips for the both devices were then deposited in a single run. Finally the Au contact of the TC device was deposited. Two consecutive cyclic sweeps were performed on both devices. A shift of the current peak is clearly seen in the displacement current of the TC device. The shift is due to the carrier trapping in the channel caused by the deep traps in the contact region generated by Au penetration, as discussed in Chapter 6. No shift is observed for the BC device, as shown in Figure 7-9. This is probably because the deep traps generated by Au penetration did not exist in the BC devices. The

positive onset of the displacement current peak for the BC device indicates some p-type doping occurred when pentacene was deposited on the Au contact.

In OFET studies, the contact resistance of the BC device is often much larger than that of the TC device. The effect of contact resistance on the displacement current behavior in LCCs with the BC configuration needs further study.

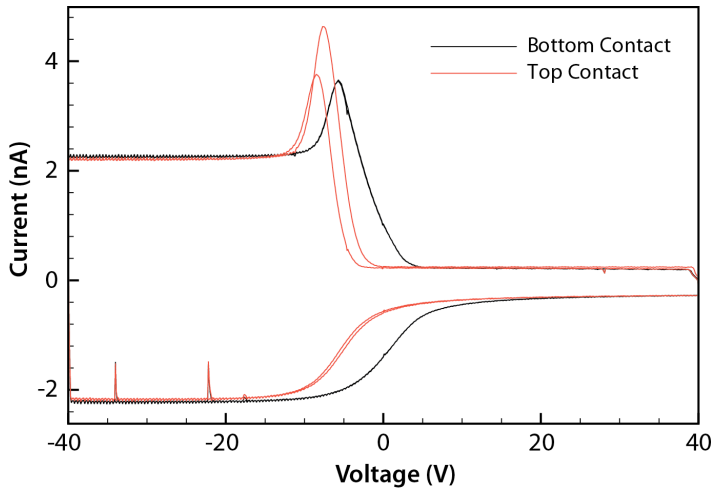

Figure 7-9 Displacement current curves of top-contact (red) and bottom-contact (black) pentacene LCCs with Au contacts.

7.3 Electrical characterizations of new organic semiconducting materials via DCM

DCM can be used as a standard technique to characterize new organic semiconductor materials. With DCM, it is easy to determine the carrier type of a new semiconductor (n- or p-type), estimate its carrier mobility, and check the purity of the material.

Figure 7-10 shows the chemical structure of *N,N'*-bis(4-methoxybenzyle)-perylene tetracarboxylic diimide (PTCDI-4MB). This material was synthesized by Jonathan Bohnsack from the Kent Mann group in the Chemistry Department at the University of Minnesota. To characterize its electrical properties, LCCs with Au contacts

were fabricated. The channel length was about 6 mm, and channel width was 0.5 mm. Figure 7-11 shows the displacement current curves measured in vacuum and in the air. Three consecutive cyclic sweeps were performed for each measurement.

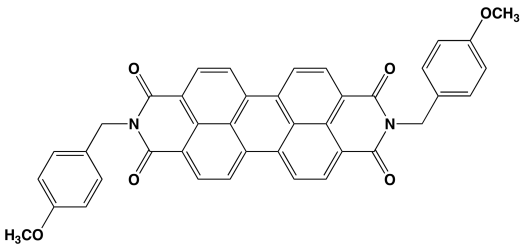

Figure 7-10 Chemical structure of PTCDI-4MB

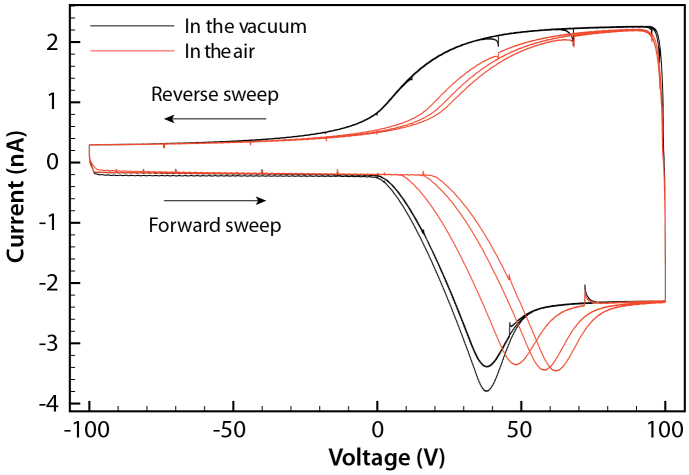

Figure 7-11 Displacement current curves of a PTCDI-4MB LCC measured in the vacuum and in the air. The forward sweep is from –100 V to +100 V.

Because the displacement current peaks occurred only in the positive gate bias, the carriers injected into the channel were electrons. In other words, PTCDI-4MB was an n-type semiconducting material. The slope of the displacement current peak measured in vacuum was about 0.125 nAV^{-1}, corresponding to an electron mobility of 8.3×10^{-3} $cm^2V^{-1}s^{-1}$ based on Equation 4-12.

When the displacement current was measured in the air, the displacement current peak in the first cyclic sweep was shifted positively. In addition, the shift between the displacement current peaks in the consecutive sweeps increased. These changes in displacement current were likely caused by the absorption of oxygen molecules that behaved as electron traps.

The above example illustrates the effectiveness of using DCM to characterize the electrical properties of small molecules whose films are usually deposited by thermal evaporation and can be easily patterned with shadow masks. For semiconducting polymers, the films are usually deposited by spin coating. Patterning these films is not easy, so that the long channel capacitors are not a good solution for characterizing the spin-coated polymer films.

A new device structure for using DCM to characterize the spin-coated polymer films is proposed here, as shown in Figure 7-12. The device fabrication includes two steps: first spin coat the polymer film of interest onto the SiO_2 substrate, then deposit a small metal contact in the center of the film.

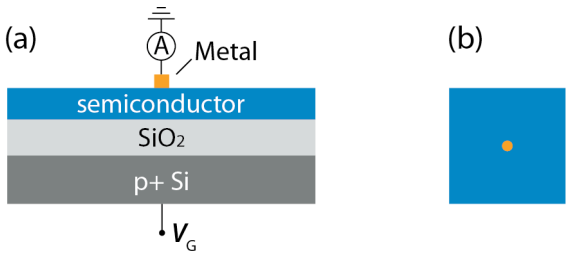

Figure 7-12 Proposed device for using DCM to characterize spin-coated polymer semiconducting films. (a) Cross-section view. (b) Top view.

Figure 7-13c shows the displacement current measured from a pentacene-based device with a slightly different structure. The pentacene film is patterned to a circular shape (Figures 7-13a and 7-13b), with a diameter of 3 mm. The diameter of the Au dot is 0.1 mm. We believe the displacement current curve taken from the proposed structure in Figure 7-12 should have a similar shape, especially at the beginning of the carrier

injection and transport when the carriers are away from the edges of the film. Although the displacement current shown in Figure 7-13c has many similarities as the typical displacement current measured from LCCs. The transient carrier transport in this new structure is 2D, instead of 1D in LCCs. New analytical or numerical model is needed to calculated mobility from the current peaks of the displacement current curve.

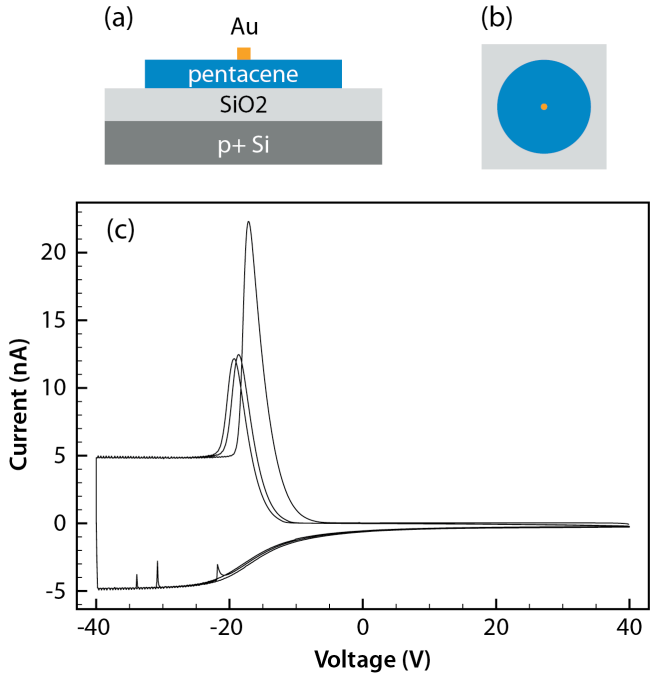

Figure 7-13 (a) and (b) Cross section and top views of a pentacene-based device. The pentacene film is circular, with a diameter of 3 mm. The diameter of the Au dot in the center is 0.1 mm. (c) Displacement current measured from this device (3 consecutive sweeps).

7.4 A device for determining charge carrier density in organic semiconductors induced by ionic liquids

Figure 7-14 shows a proposed device for determining the charge carrier density in organic semiconductors induced by ionic liquids via displacement current measurement. This device can be used to characterize spin coated polymer films and organic single crystals.

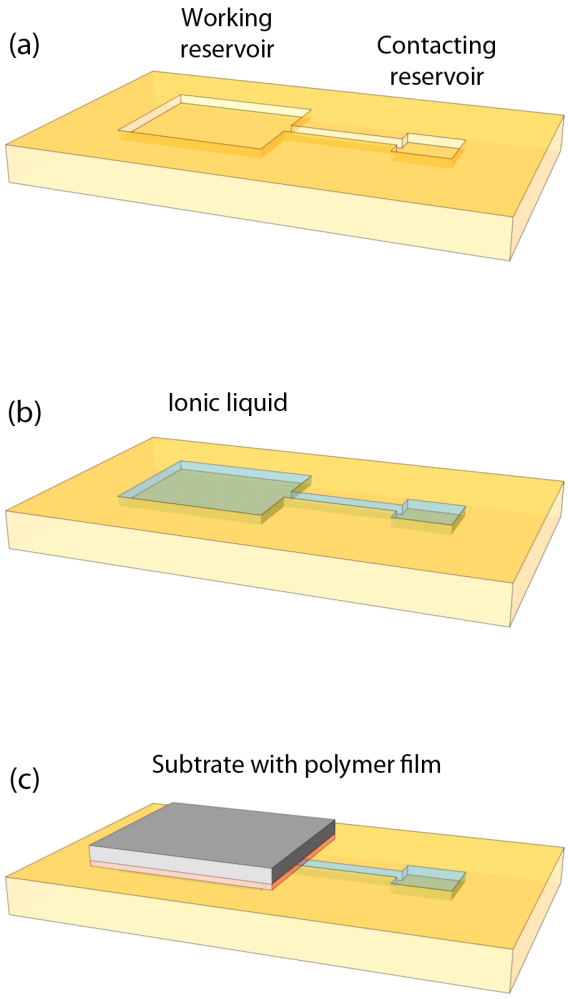

Figure 7-14 A proposed device for determining the charge carrier density in organic semiconductors induced by ionic liquids via displacement current measurement. (a) A PDMS stamp containing two reservoirs and a channel connecting them. The bottom surface of the reservoirs and the channel, and the top surface of the PDMS stamp are both covered with metal, but the two surfaces are not electrically connected. (b) The reservoirs and channel are filed with ionic liquid. (c) The working reservoir is covered with a substrate with the polymer film of interest on it. The polymer film is in contact with the top surface of the PDMS stamp. During measurements, the displacement current is measured from the grounded top surface of the PDMS stamp while voltage sweeps is applied on the bottom surface of the contacting reservoir.

The major part of the device is a PDMS stamp with two rectangular reservoirs and a channel connecting them (Figure 7-14a). The shape of the reservoirs can be changed if needed. We call the larger reservoir the *working reservoir*, and the smaller one the *contacting reservoir* (electrical contact is made on the bottom of this reservoir). The bottom surface of the reservoirs and the channel, and the top surface of the PDMS stamp are both covered with metal, but the two surfaces are not electrically connected. This can be realized by using the same method for fabricating the free-space gate dielectrics based on PDMS stamp.[66] We call the metal contact on the bottom surface of the reservoirs and channel the *bottom contact*, and the metal contact on the top surface of the PDMS stamp the *top contact*.

During measurements, the reservoirs and channel are first filled with enough ionic liquid (Figure 7-14b). *It is important to note that the channel connecting the two reservoirs can be blocked so that liquid is only in the working reservoir.* After covering the working reservoir with a polymer film (on a insulating substrate) or a single crystal (which should be larger than the working reservoir), as shown in Figure 7-14c, a small pressure can be applied on the substrate or the crystal to ensure good electrical connection between the organic and the top contact. The displacement current is measured from the grounded top contact while voltage sweeps are applied on the bottom contact of the contacting reservoir. To measure the background current, the previous substrate or crystal is removed, and the working reservoir is covered with a bare insulating substrate, and then the same displacement current measurement is performed again.

The major advantage of this device is the use of the working reservoir to define of the active area on the unpatterned polymer film or irregular shaped single crystals. This is very important for accurately determining the carrier density induced by the ionic liquid. The size of the working reservoir can be fine tuned either to increase the displacement current signal-to-noise ratio or to fit well with the size of the single crystal. In addition, the device allows easy and accurate detection of the background current. Last but not least, this device is reusable after cleaning the PDMS stamp.

References

[1] S. Egusa, N. Gemma, A. Miura, K. Mizushima and M. Azuma, *J Appl Phys* **71**, 2042 (1992).

[2] S. Egusa, A. Miura, N. Gemma and M. Azuma, *Jpn J Appl Phys 1* **33**, 2741 (1994).

[3] S. Ogawa, Y. Kimura, H. Ishii and M. Niwano, *Jpn J Appl Phys 2* **42**, L1275 (2003).

[4] S. Ogawa, T. Naijo, Y. Kimura, H. Ishii and M. Niwano, *Appl Phys Lett* **86**, 252104 (2005).

[5] S. Ogawa, T. Naijo, Y. Kimura, H. Ishii and M. Niwano, *Synthetic Met* **153**, 253 (2005).

[6] Y. Majima, D. Kawakami, S. Suzuki and Y. Yasutake, *Jpn J Appl Phys 1* **46**, 390 (2007).

[7] S. Ogawa, Y. Kimura, M. Niwano and H. Ishii, *Appl Phys Lett* **90**, 033504 (2007).

[8] Y. Xia, V. Kalihari, C. D. Frisbie, N. K. Oh and J. A. Rogers, *Appl Phys Lett* **90**, 162106 (2007).

[9] S. Suzuki, Y. Yasutake and Y. Majima, *Jpn J Appl Phys* **47**, 3167 (2008).

[10] E. Pavlica and G. Bratina, *J Phys D Appl Phys* **41**, 135109 (2008).

[11] S. Yoshita, R. Tamura, D. Taguchi, M. Weis, E. Lim, T. Manaka and M. Iwamoto, *J Appl Phys* **106**, 024505 (2009).

[12] S. Suzuki, Y. Yasutake and Y. Majima, *Org Electron* **11**, 594 (2010).

[13] N. Abiko, K. Sugi, T. Suenaga, Y. Kimura, H. Ishii and M. Niwano, *Jpn J Appl Phys 1* **45**, 442 (2006).

[14] Y. Noguchi, N. Sato, Y. Tanaka, Y. Nakayama and H. Ishii, *Appl Phys Lett* **92**, 203306 (2008).

[15] S. Lee, J. Hur and S. Lim, *J Soc Inf Display* **18**, 103 (2010).

[16] R. Liu, Y. L. Lei, P. Chen, Q. L. Song and Z. H. Xiong, *J Phys D Appl Phys* **42** (2009).

[17] G. Horowitz, *Adv Mater* **10**, 365 (1998).

[18] C. D. Dimitrakopoulos and P. R. L. Malenfant, *Adv Mater* **14**, 99 (2002).

[19] C. R. Newman, C. D. Frisbie, D. A. da Silva, J. L. Bredas, P. C. Ewbank and K. R. Mann, *Chem Mater* **16**, 4436 (2004).

[20] D. Braga and G. Horowitz, *Adv Mater* **21**, 1473 (2009).

[21] M. Bendikov, F. Wudl and D. F. Perepichka, *Chem Rev* **104**, 4891 (2004).

[22] A. R. Murphy and J. M. J. Frechet, *Chem Rev* **107**, 1066 (2007).

[23] A. Pron and P. Rannou, *Prog Polym Sci* **27**, 135 (2002).

[24] H. Sirringhaus, *Adv Mater* **17**, 2411 (2005).

[25] C. D. Dimitrakopoulos, A. R. Brown and A. Pomp, *J Appl Phys* **80**, 2501 (1996).

[26] Y. Y. Lin, D. J. Gundlach, S. F. Nelson and T. N. Jackson, *Ieee Electr Device L* **18**, 606 (1997).

[27] M. Shtein, J. Mapel, J. B. Benziger and S. R. Forrest, *Appl Phys Lett* **81**, 268 (2002).

[28] D. Knipp, R. A. Street, A. Volkel and J. Ho, *J Appl Phys* **93**, 347 (2003).

[29] A. Tsumura, H. Koezuka and T. Ando, *Appl Phys Lett* **49**, 1210 (1986).

[30] S. R. Forrest, *Nature* **428**, 911 (2004).

[31] J. A. Rogers, Z. Bao, K. Baldwin, A. Dodabalapur, B. Crone, V. R. Raju, V. Kuck, H. Katz, K. Amundson, J. Ewing and P. Drzaic, *P Natl Acad Sci USA* **98**, 4835 (2001).

[32] T. Someya, T. Sekitani, S. Iba, Y. Kato, H. Kawaguchi and T. Sakurai, *P Natl Acad Sci USA* **101**, 9966 (2004).

[33] J. H. Cho, J. Lee, Y. Xia, B. Kim, Y. Y. He, M. J. Renn, T. P. Lodge and C. D. Frisbie, *Nature Materials* **7**, 900 (2008).

[34] T. Sekitani, U. Zschieschang, H. Klauk and T. Someya, *Nature Materials* **9**, 1015 (2010).

[35] T. Manaka, E. Lim, R. Tamura and M. Iwamoto, *Nat Photonics* **1**, 581 (2007).

[36] T. Manaka, F. Liu, M. Weis and M. Iwamoto, *Phys Rev B* **78**, 121302 (2008).

[37] T. Manaka, F. Liu, M. Weis and M. Iwamoto, *J Phys Chem C* **113**, 10279 (2009).

[38] T. Manaka, F. Liu, M. Weis and M. Iwamoto, *J Appl Phys* **107**, 043712 (2010).

[39] L. Dunn, D. Basu, L. Wang and A. Dodabalapur, *Appl Phys Lett* **88**, 063507 (2006).

[40] R. Dost, A. Das and M. Grell, *J Appl Phys* **104**, 084519 (2008).

[41] M. Weis, J. Lin, D. Taguchi, T. Manaka and M. Iwamoto, *J Phys Chem C* **113**, 18459 (2009).

[42] D. Basu, L. Wang, L. Dunn, B. Yoo, S. Nadkarni, A. Dodabalapur, M. Heeney and I. McCulloch, *Appl Phys Lett* **89**, 242104 (2006).

[43] L. Dunn and A. Dodabalapur, *J Appl Phys* **107**, 113714 (2010).

[44] S. M. Sze, *Physics of Semiconductor Devices*. (Wiley, New York, 1981).

[45] Y. Liang, C. D. Frisbie, H. C. Chang and P. P. Ruden, *J Appl Phys* **105**, 024514 (2009).

[46] H. C. Chang, P. P. Ruden, Y. Liang and C. D. Frisbie, *J Appl Phys* **107**, 104502 (2010).

[47] N. J. Watkins, L. Yan and Y. L. Gao, *Appl Phys Lett* **80**, 4384 (2002).

[48] N. Koch, A. Kahn, J. Ghijsen, J. J. Pireaux, J. Schwartz, R. L. Johnson and A. Elschner, *Appl Phys Lett* **82**, 70 (2003).

[49] L. Diao, C. D. Frisbie, D. D. Schroepfer and P. P. Ruden, *J Appl Phys* **101**, 014510 (2007).

[50] A. C. Durr, F. Schreiber, M. Kelsch, H. D. Carstanjen and H. Dosch, *Adv Mater* **14**, 961 (2002).

[51] J. H. Cho, D. H. Kim, Y. Jang, W. H. Lee, K. Ihm, J. H. Han, S. Chung and K. Cho, *Appl Phys Lett* **89**, 132101 (2006).

[52] I. Kymissis, C. D. Dimitrakopoulos and S. Purushothaman, *Ieee T Electron Dev* **48**, 1060 (2001).

[53] D. J. Gundlach, L. Zhou, J. A. Nichols, T. N. Jackson, P. V. Necliudov and M. S. Shur, *J Appl Phys* **100**, 024509 (2006).

[54] K. Asadi, Y. Wu, F. Gholamrezaie, P. Rudolf and P. W. M. Blom, *Adv Mater* **21**, 4109 (2009).

[55] S. D. Wang, T. Minari, T. Miyadera, K. Tsukagoshi and Y. Aoyagi, *Appl Phys Lett* **91**, 203508 (2007).

[56] C. A. Di, G. Yu, Y. Q. Liu, Y. L. Guo, Y. Wang, W. P. Wu and D. B. Zhu, *Adv Mater* **20**, 1286 (2008).

[57] S. D. Wang, T. Minari, T. Miyadera, Y. Aoyagi and K. Tsukagoshi, *Appl Phys Lett* **92**, 063305 (2008).

[58] C. Y. Yang, Dhananjay, S. S. Cheng, C. W. Ou, Y. C. Chuang, M. C. Wu and C. W. Chu, *Appl Phys Lett* **92**, 253307 (2008).

[59] L. L. Chua, J. Zaumseil, J. F. Chang, E. C. W. Ou, P. K. H. Ho, H. Sirringhaus and R. H. Friend, *Nature* **434**, 194 (2005).

[60] K. Ihm, S. M. Chung, T. H. Kang and S. W. Cheong, *Appl Phys Lett* **93**, 141906 (2008).
[61] T. Sawabe, K. Okamura, T. Sueyoshi, T. Miyamoto, K. Kudo, N. Ueno and M. Nakamura, *Appl Phys a-Mater* **95**, 225 (2009).
[62] M. Nakamura, N. Goto, N. Ohashi, M. Sakai and K. Kudo, *Appl Phys Lett* **86**, 122112 (2005).
[63] X. H. Zhang, B. Domercq and B. Kippelen, *Synthetic Met* **159**, 2371 (2009).
[64] H. C. Chang, P. P. Ruden, Y. Liang and C. D. Frisbie, *Appl Phys Lett* **In preparation**.
[65] Y. Hirose, A. Kahn, V. Aristov, P. Soukiassian, V. Bulovic and S. R. Forrest, *Phys Rev B* **54**, 13748 (1996).
[66] E. Menard, V. Podzorov, S. H. Hur, A. Gaur, M. E. Gershenson and J. A. Rogers, *Adv Mater* **16**, 2097 (2004).

Appendix I – Detailed feature dimensions of the shadow masks in Figure 3-2

The size of all the masks is 25 mm × 25 mm.

PM1. The larger rectangles in the top and bottom rows are for LCCs with a size of 0.5 mm × 6 mm, the smaller rectangles in the middle two rows are for OFETs with a size of 0.5 mm × 1 mm.

PM2. The rectangles in the top row are for LCCs with a size of 0.5 mm × ***a*** mm. From left to right, ***a*** = 6, 6, 5, 5, 4, 4, 3, 3, 2, 2, 1, 1, 0.5, 0.125, 0.125. The rectangles in the middle two rows are for OFETs with a size of 0.5 mm × 1 mm. The rectangles in the bottom row are for LCCs with a size of 0.5 mm × ***b*** mm. From left to right, ***b*** = 0.125, 2.5, 2.5, 3, 3, 3.5, 3.5, 4, 4, 4.5, 4.5, 5, 5, 5.5, 5.5, 6, 6.

PM3. All the rectangles are for LCCs. The rectangles in the top row are of a size of ***c*** mm × 3 mm. From left to right, ***c*** = 1, 2, 3, 4, 5. The rectangles in the bottom row are of a size of ***d*** mm × 2 mm. From left to right, ***d*** = 1.5, 3, 4.5, 6.

CM1. The rectangles in the top and bottom rows are for LCCs with a size of 0.75mm × 0.5 mm. The rectangles in the middle two rows are source-drain pairs for OFETs. The transistor channel length defined by each pair is 100 μm.

CM2. The rectangles in the top and bottom rows are for LCCs with a size of 0.75mm × 0.5 mm. The rectangles in the middle two rows are source-drain pairs for OFETs. For the first middle row from left to right, the channel length defined by each source-drain pair is 300, 280, 260, 240, 220, 200, 180, 160, 140, 120, 100, 80, 60, 40, 20 μm. For the second middle row from left to right, the channel length is 25, 50, 50, 75, 75, 100, 100, 125, 125, 150, 150, 175, 175, 200, 200 μm.

CM3. All the rectangles are for LCCs. The rectangles in the top row are of a size of ***e*** mm × 0.5 mm. From left to right, ***e*** = 1.25, 2.25, 3.25, 4.25, 5.25. The rectangles in the bottom row are of a size of ***f*** mm × 2 mm. From left to right, ***f*** = 1.75, 3.25, 4.75, 6.25.

Appendix II – Keithley 2612 test scripts for displacement current measurement

Script 1: DCM with voltage sweeps

In this script, Channel B of Keithley 2612 sources gate voltage sweeps, and Channel A measures displacement current.

```
-- Create 3 arrays for storing voltage, current, and time readings.
voltage_array = {}
current_array = {}
time_array = {}

-- Set initial measurement parameters. "v_start" and "v_stop" are the
starting and ending voltages of the sweep, respectively. "v_step" is
the voltage step within the sweep. "loops" defines how many cyclic
sweeps will be performed.
v_start = 40
v_stop = -40
v_step = -0.1
loops = 2

-- Set the index number of upcoming "for loop" to 1.
index = 1

-- Reset both channels.
smua.reset()
smub.reset()

-- Set the voltage sourcing range of Channel B to 200 V.
smub.source.rangev = 200

-- Set the integration time of Channel A. NPLC (number of power line
cycles) controls the integration time. When NPLC = 1, the integration
time, or the time to take a current reading, is about 17 ms.
smua.measure.nplc = 1

-- Set the upper limit of current reading of Channel A to 10^-7 A. The
upper limit also determines the noise level. Try to set it as low as
possible.
smua.measure.rangei = 1e-7

-- Set Channel B to source DC voltage, and turn on voltage sourcing.
smub.source.func = smub.OUTPUT_DCVOLTS
smub.source.output = smub.OUTPUT_ON
```

```
-- Set the Channel B voltage to "v_start" for 5 seconds to eliminate
the large displacement current generated by sudden voltage change.
smub.source.levelv = v_start
delay(5)

-- Reset timer.
timer.reset()

-- The cyclic sweeps.
for m = 1, loops, 1 do

      -- The forward sweep.
      for v = v_start, v_stop, v_step do

            -- Channel B sources voltage.
            smub.source.levelv = v

            -- Channel A measures current and writes the current
            reading to "current_array".
            current_array[index] = smua.measure.i()

            -- Timer reads time and writes the time reading to
            "time_array".
            time_array[index] = timer.measure.t()

            -- Write the voltage to "voltage_array".
            voltage_array[index] = v

            -- Increase the index number by 1.
            index = index + 1

      end

      -- The reverse sweep
      for v = v_stop, v_start, -v_step do

            smub.source.levelv = v
            current_array[index] = smua.measure.i()
            time_array[index] = timer.measure.t()
            voltage_array[index] = v
            index = index+1

      end
end

-- Turn off voltage sourcing of Channel B.
smub.source.output = smub.OUTPUT_OFF

-- Print out the data stored in all arrays.
for n=1, index-1, 1 do

      print(voltage_array[n], current_array[n], time_array[n])

end
```

Script 2: DCM with voltage Steps

In this script, Channel B of Keithley 2612 sources charging and discharging gate voltage steps, and Channel A measures displacement current during the discharging voltage step.

```
-- Create 2 arrays for storing current and time readings.
current_array = {}
time_array = {}

-- Set initial measurement parameters. "v_charge" and "v_discharge" are
the charging and discharging voltages, respectively. "t_charge" is the
charging time in seconds. "n_datapoints" is the number of data points
taken during the discharging step.
v_charge = -80
v_discharge = 40
t_charge = 15
n_datapoints = 18000

-- Set the index number of upcoming "for loop" to 1.
index = 1

-- Reset both channels.
smua.reset()
smub.reset()

-- Set the voltage sourcing range of Channel B to 200 V.
smub.source.rangev = 200

-- Set the integration time of Channel A. NPLC (number of power line
cycles) controls the integration time. When NPLC = 1, the integration
time, or the time to take a current reading, is about 17 ms.
smua.measure.nplc = 1

-- Set the upper limit of current reading of Channel A to 10^-7 A. The
upper limit also determines the noise level. Try to set it as low as
possible.
smua.measure.rangei = 1e-7

-- Set Channel B to source DC voltage, and turn on voltage sourcing.
smub.source.func = smub.OUTPUT_DCVOLTS
smub.source.output = smub.OUTPUT_ON

-- The charging step. Channel B sources "v_charge" for "t_chrage"
seconds.
smub.source.levelv = v_charge
delay(t_charge)

-- The discharging step starts.
smub.source.levelv = v_discharge
```

```
-- Reset timer after the sourcing voltage of Channel B changes to
"v_discharge".
timer.reset()

-- Channel A measures displacement current during the discharging step.
The total time of the discharging step is determined by the time to
measure a single current data point and the total number of the data
points ("n_datapoints"). With NPLC = 1, 18000 date points give a total
discharging time of about 300 s.
for p = 1, n_datapoints, 1 do

      -- Channel A measures current and write the current reading to
      "current_array".
      current_array[index] = smua.measure.i()

      -- Timer reads time and writes the time reading to "time_array".
      time_array[index] = timer.measure.t()

      -- Increase the index number by 1.
      index = index+1

end

-- Turn off voltage sourcing of Channel B.
smub.source.output = smub.OUTPUT_OFF

-- Print out the data stored in "time_array" and "current_array".
for n=1, index-1, 1 do

      print(time_array[n], current_array[n])

end
```

Appendix III – Common mistakes in displacement current measurement

Mistake 1: Adding delay in measurement cycle

When Keithley 236/237 is used for displacement current measurement, it is important to use the *Measure Only* function instead of using the *Source-Delay-Measure (SDM)* function. The SDM function adds *default delay* before the actual current measurement takes place to *reduce* the displacement current, as shown in Figure A-1.

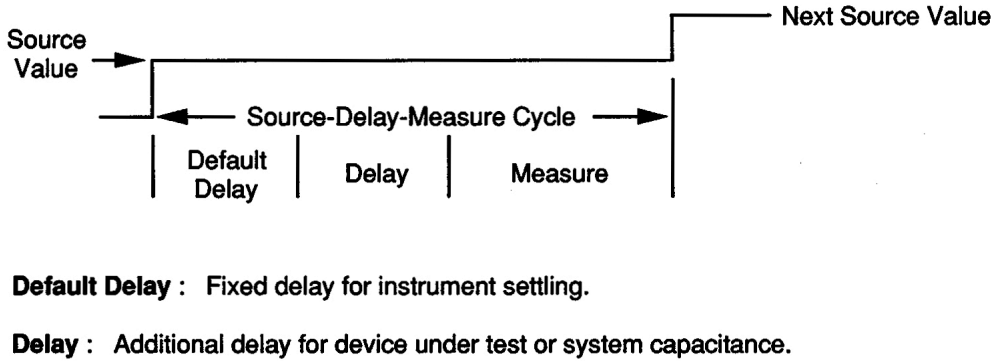

Figure A-1 Source-Delay-Measure cycle used by Keithley 236/237. This image is taken from *Keithley Model 236/237/238 Source Measure Units Operator's Manual Rev. E.*

Figure A-2 shows the displacement current measured from a pentacene LCC with Keithley 236. The constant background displacement current associated with the contact and the constant displacement current after pentacene becomes conductive are eliminated from the current reading due to the default delay. Only the displacement current associated with the transient transport remains, but the current value is reduced.

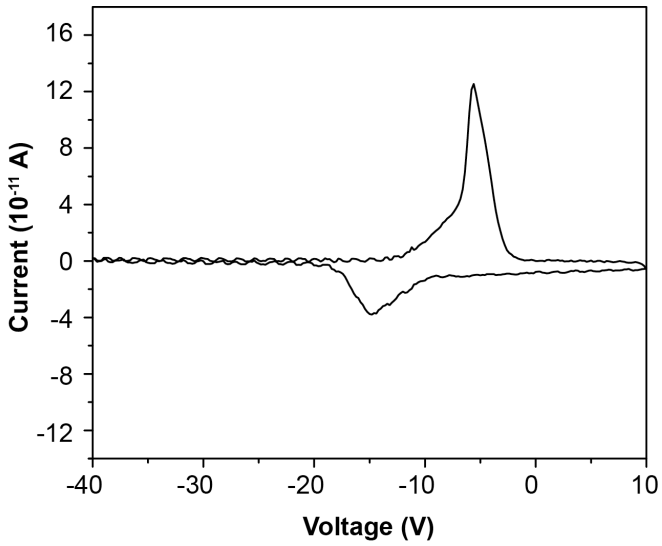

Figure A-2 Displacement current measured from a pentacene LCC with Keithley 236.

Similar results can be observed in the displacement current measured with Keithley 2612 if a delay is intentionally added before the current reading takes place, as shown in Figure A-3. In fact, any delay in the displacement current measurement cycle may result in underestimating the displacement current and should be avoided.

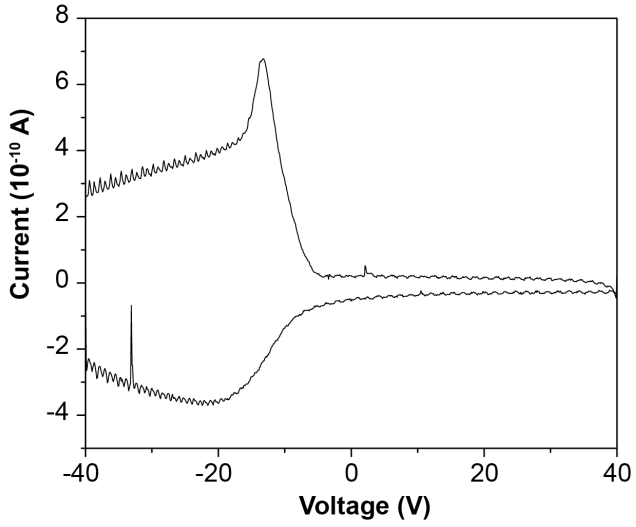

Figure A-3 Displacement current measured from a pentacene LCC with Keithley 2612. A delay was added before the current measurement, resulting in the reduction of displacement current.

Mistake 2: Applying voltage sweeps and measuring displacement current with the same channel of Keithley 2612

When displacement current is measured with the same channel that applies voltage sweeps, a background current associated with the internal capacitance of Keithley 2612 is measured, as shown by the red line in Figure A-4 (the channel is not connected to the device under test (DUT)). This background current can be eliminated by using two channels: one channel only applies voltage sweep, and the other channel only measures displacement current. For example, when Channel A measures current and Channel B applies voltage sweeps, a much smaller background current is measured, as shown by the black line in Figure A-4 (both channels are not connected to DUT).

Based on above discussion, when displacement current is measured from a gate electrode with the same channel that applies gate voltage sweeps, a background current will be measured. To measure displacement current from the gate but avoid the background current, it is better to use one channel to apply voltage sweep *on the channel contact*, and use the other channel to measure the displacement current from the gate electrode.

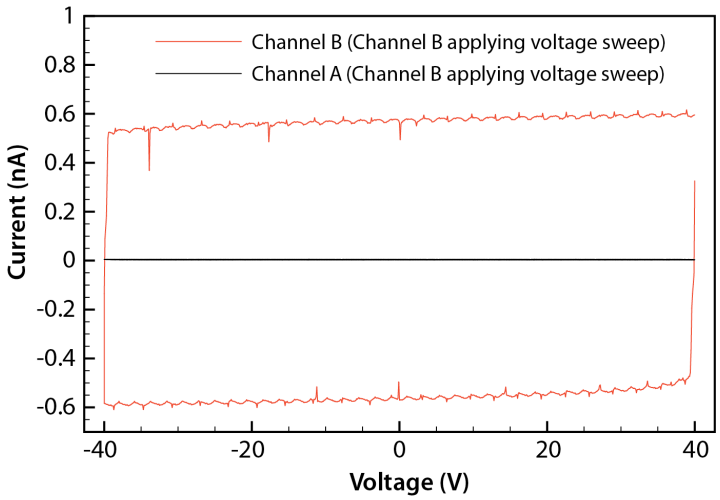

Figure A-4 Background current associated with Keithley 2612. Channel A and Channel B are *not* connected to DUT. The sweep rate is 5.7 Vs^{-1}. Red line, Channel B applies voltage sweeps and measures current. Black line, Channel B applies voltage sweeps and Channel A measures current.

Mistake 3: Measuring displacement current from an OFET in which the organic semiconductor film is not properly patterned

If an OFET is used for DCM, the displacement current of interests is associated with charging/discharging the conducting channel. As a result, it is important to pattern the organic semiconductor film so that it does not extend over the channel region between the source and drain electrodes, as shown in Figure A-5a. Otherwise (Figure A-5b), the displacement current will include both the component charging/discharging the channel and the component charging/discharging the organic film beyond the source and drain contacts. It is impossible the separate these two components.

Figure A-5 OFETs for displacement current measurement. (a) The organic semiconductor film is properly patterned. (b) The organic semiconductor film is not properly patterned.

Appendix IV – A proposed experiment to examine detrapping kinetics

The experiment procedures are as following.

(1) A long-channel capacitor is charged at a constant charging voltage V_{chg} (*e.g.* −40 V) for a short period of time (*e.g.* 30 s). The charging time should be long enough that the carrier distribution in the channel is stabilized and uniform. Then the voltage is swept to a discharging voltage V_{dischg} (*e.g.* 0 V) and held at V_{dischg}. The displacement current I_1 is recorded *vs.* time once the voltage reaches V_{dischg}. Figure A-6a summarizes this procedure.

(2) Increase the charging time (*e.g.* 480 s) and repeat Step (1). The displacement current I_2 is recorded *vs.* time once the voltage reaches V_{dischg}. Figure A-6b summarizes this procedure.

(3) Subtract I_2 with I_1. The resulting current is mainly related to the detrapped carriers. Figure A-6c shows the experimental results.

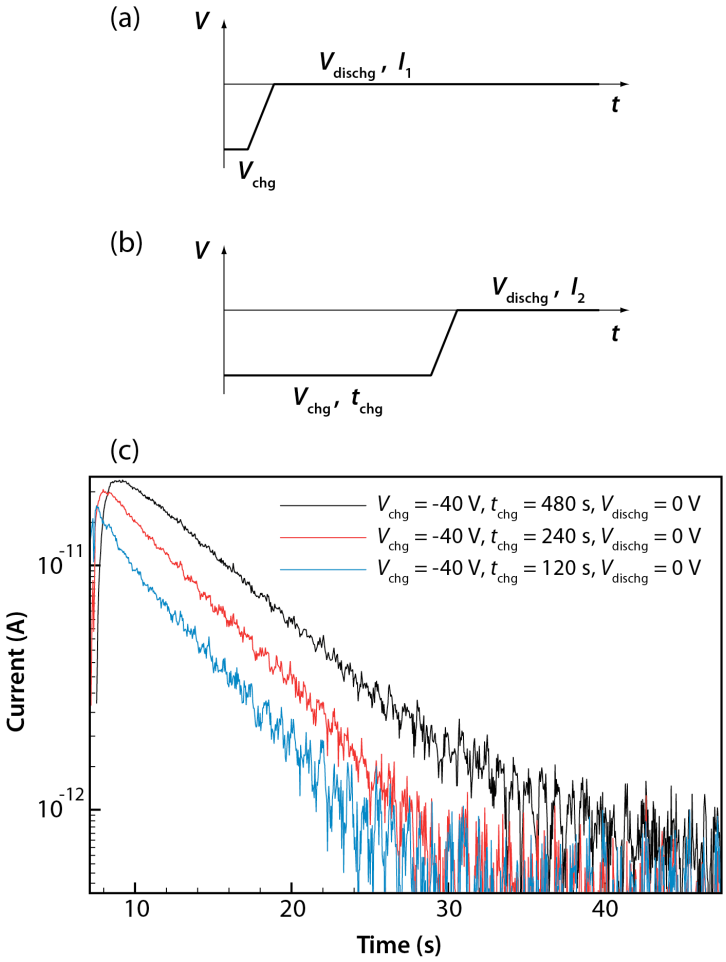

Figure A-6 Proposed experiment to examine detrapping kinetics. (a) and (b) two experimental procedures for measuring displacement current during contact discharging voltage. The difference between the two is the charging time. (c) Experimental results of $I_2 - I_1$.

The following model is proposed to explain the experimental data.

For the short charging time, I_1 results from the free carriers remaining in the channel, *i.e.*

$$I_1 = \frac{d\bar{p}_0}{dt} S \qquad \text{(A-1)}$$

where $\bar{p}_0$ is the average free carrier density in the channel, and S is the channel area.

For the long charging time, I_2 results from both the free carriers and the detrapped carriers in the channel, *i.e.*

$$I_2 = \left(\frac{d\bar{p}_0}{dt} - \frac{d\bar{p}_t}{dt} \right) S \qquad \text{(A-2)}$$

where $\bar{p}_t$ is the average density of the trapped carriers in the channel.

By subtracting I_2 with I_1 we get:

$$\Delta I = -\frac{d\bar{p}_t}{dt} S \qquad \text{(A-3)}$$

Since

$$-\frac{dp_t}{dt} = \tilde{e} p_t \qquad \text{(A-4)}$$

where $\tilde{e}$ is the emission coefficient, we get

$$p_t = A \exp(-\tilde{e} t) \qquad \text{(A-5)}$$

where A is a constant. Inset Equation A-5 into A-3, we get

$$\Delta I = \tilde{e} A S \exp(-\tilde{e} t) \qquad \text{(A-6)}$$

From Equation A-6, we know that ΔI follow an exponential decay, just as the data shown in Figure A-6c. In addition, the emission coefficient can be obtained from the slope of the linear fitting of the experimental data in a log-log plot. For the data shown in Figure A-6c, the emission coefficient is about 0.1 s^{-1}.